LATVIAN JOURNAL of PHYSICS and TECHNICAL SCIENCES

ISSN 0868 - 8257

5

(Vol. 61)

2024

CONTENTS

Y. Suchikova, S. Kovachov, I. Bohdanov, M. Konuhova, A. I. Popov
Synthesis of Periodic Porous Structures on the Surface of Indium Phosphide 3

R. Bakanas, A. Nikolskij, A. Bulanovs, D. Brotherton-Ratcliffe
Recent Works on Direct-Write Digital Holography 16

J. Kallunki, T. Kauppinen
A Method to Estimate Solar Panel Orientation Effectivity 28

L. Zemite, A. Backurs, K. Vonda, S. Batjuskovs, P. Cnubbern, L. Jansons
Comparative Study of Waste Management and Sampling Practices in Latvia and Estonia 36

J. Gutans, N. Mozga, A. Klokovs, N. Glizde, M. Kleinhofs
Main Stages and Results of the Development of Mobile Space Environment Simulation Facility "Metamorphosis" 58

A. G. E. M. I. Mowafy, I. Steiks
Advanced Maximum Power Point Tracking Technique for Photovoltaic Reverse Osmosis Systems 78

J. V. Sanchaniya, V. Rana, S. R. Vejanand
Optimisation of Electrospinning Parameters for High-Strength Oriented PAN Nanofibre Mats 90

A. Kapparova, S. Orynbassar, G. Dosymbetova, D. Almen, E. Yershov, A. Saymbetov, M. Nurgaliyev, N. Algazin, A. Sharipbay, D. Zhastalapova
Modelling Π-Shaped Concentrating Optics for LCPV Solar Cells using Fresnel Lens 101

LATVIAN JOURNAL of PHYSICS and TECHNICAL SCIENCES

LATVIJAS FIZIKAS un TEHNISKO ZINĀTŅU ŽURNĀLS

Published six times a year since February 1964
Iznāk sešas reizes gadā kopš 1964. gada februāra

5 (Vol. 61) • 2024

RĪGA

Language Editor: O. Ivanova
Computer Designer: I. Begicevs

INDEXED (PUBLISHED) IN

www.scopus.com
www.sciendo.com
EBSCO (Academic Search Complete, www.epnet.com), INSPEC (www.iee.org.com).
VINITI (www.viniti.ru), Begell House Inc/ (EDC, www.edata-center.com).

Issuers: Institute of Physical Energetics,
Institute of Solid State Physics, University of Latvia
Registration Certificate Number: 000700221

Editorial Contacts:
14 Dzerbenes Street, Riga, LV-1006
LATVIA
tel: +371 26245896
M: +371 29363105
leo@lza.lv

sciendo

LATVIAN JOURNAL OF PHYSICS
AND TECHNICAL SCIENCES
2024, N 5

DOI: 10.2478/lpts-2024-0032

SYNTHESIS OF PERIODIC POROUS STRUCTURES ON THE SURFACE OF INDIUM PHOSPHIDE

Y. Suchikova[1*], S. Kovachov[1], I. Bohdanov[1], M. Konuhova[2], A. I. Popov[2]

[1] Berdyansk State Pedagogical University,
4 Schmidt Str., Berdyansk, 71100, UKRAINE
[2] Institute of Solid State Physics,
University of Latvia,
8 Kengaraga Str., Riga, LV-1063, LATVIA
*e-mail: yanasuchikova@gmail.com

The paper demonstrates the possibility of forming specific nanostructures of the "parquet" type of nanowires on the InP surface. The resulting nanostructure is characterised by an ordered transverse and longitudinal relative shift of separate nanowires. A dislocation model is proposed that explains the mechanism of such structure formation. The numerical estimates of the geometric parameters of the nanostructure obtained during theoretical modelling are quite adequate for the experimental results.

Keywords: *Dislocations, electrochemical etching, indium phosphide, periodic nanostructures, porous oxide.*

1. INTRODUCTION

The interest in nanostructured semiconductors is due to the variety of morphological forms obtained [1], [2] and the broad prospects for applications [3]–[14]. Today, many different methods of surface nanostructuring are known, including the method of reactive magnetron sputtering [15], matrix synthesis [16], electrochemical deposition [17], [18], electrochemical etching [19], [20], lithography [21], etc. Electrochemical etching is increasingly popular due to the simplicity of technology and low cost [22]. This method has shown the highest efficiency for the nanostructuring of Si and A_3B_5 semiconductors, in particular, InP, GaP, GaAs [23]–[25]. When these semiconductors are etched in selective etchants, etching holes are often observed on the surface and in most of the crystal [26], [27]. A high concentration of etching pits determines the porous structure of the semiconductor plate, which causes a change in

properties and has been widely used. In particular, as a result of the high surface roughness, the range of light absorption expands, making it possible to use such structures as a material for PEP [28]. When the resistivity of porous structures is increased, an improvement in piezoelectric characteristics is observed, which is promising for the creation of sensors [29]. Porous semiconductors are known to be applied as a template for nanorods and nanotubes [30]. Porous layers are a 'soft' substrate for growing thin films, in particular, InN, GaN, etc. [31]. A promising direction is now directed controlled electrochemical etching, which leads to the formation of ordered periodic nanostructures [32].

As a rule, the formation of pores during electrochemical etching of a semiconductor begins at the sites of localisation of crystal lattice defects [33], [34]. This process can be accompanied by alternative reactions, for example, the formation of continuous insoluble films, surface texturing, overgrowing with oxides, etc. [35]–[38]. This is the reason for the low controllability of the process and the lack of a single mechanism for the pore formation process on the semiconductor surface.

In this study, the formation of periodic porous structures on the surface of n-InP (111) is reported, the mechanisms of their formation and their chemical composition are investigated.

2. EXPERIMENTAL DETAILS AND RESULTS

The structures were formed by electrochemical etching in a hydroalcoholic solution of hydrofluoric acid $HF:H_2O:C_2H_5OH=1:1:2$ at a constant current density $j=150$ mA/cm^2. A simple electrochemical cell with platinum on the cathode was used for etching. The experiment was carried out in the dark at room temperature. Before the experiment, the samples were cleaned with alcohol and vinegar. After electrochemical etching, the samples were kept in the same electrolyte for 10 minutes. The technology is described in detail in our work [19], [34]. The electrolyte was stirred during etching in order to remove bubbles from the semiconductor plate.

The morphological characteristics of the produced nanostructures were investigated using scanning electron microscopy. Chemical analysis of the surface layers was performed using the EDAX and INCA energy methods.

As a result of etching, structures were obtained in the form of massive porous nanowires packed according to the "parquet" type (Fig. 1a). The thickness of each wire is about 10 microns, the height is up to 10 microns, and the length is between 100 and 130 microns. The distance between the parquet layers is 20 to 50 microns. The wires have a porous, loose structure. They peel off easily from the crystal surface. Also, on closer inspection, one can notice that the parquet areas are easily combined with each other. In Fig. 1b, one can see a nanowire that broke at a cleavage of the crystalline material. This shows the fragility and looseness of the structure. In addition, an uneven crater structure of the surface of the InP sample is observed.

According to the results of the chemical analysis of the surface layers, the wires contain oxygen (Table 1), showing the formation of the oxide phase.

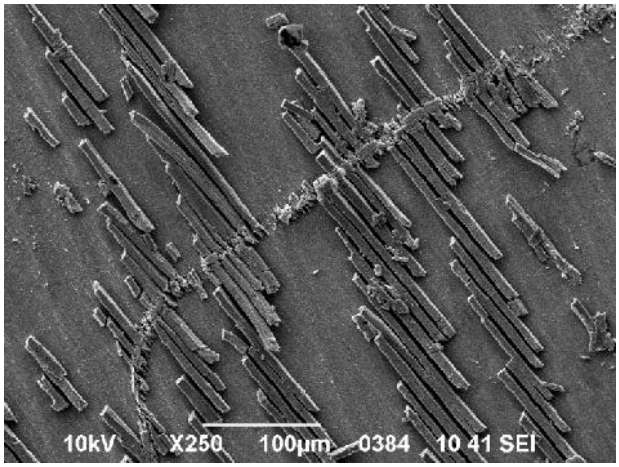

a)

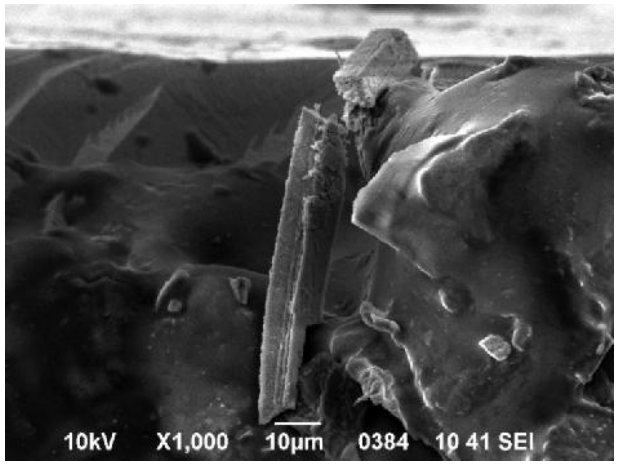

b)

Fig. 1. SEM image of the InP: a) surface after electrochemical etching in an hydroalcoholic solution of hydrofluoric acid; b) cleavage with a broken wire.

Table 1. Chemical Analysis of Surface Layers

Point of the surface	Element			Total
	O	P	In	
a	18.70	11.04	70.26	100.00
b	16.09	8.71	75.20	100.00
c	14.56	10.92	74.52	100.00
d	18.05	3.1	78.85	100.00
Average value	16.85	8.44	74.71	100.00

There are small concentrations of phosphorus (on average 8.44 %) and oxygen (on average 16.85 %), while indium is present in high concentrations (on average 74.71 %).

3. DISCUSSION

3.1. Electrochemical Processes on the Surface of Indium Phosphide in an Electrolyte Solution

In the interaction of A^3B^5 compounds with acid solutions, it is necessary to take into account the nature and chemical properties of the individual elements that are parts of the compound, as well as the physicochemical properties of the surfaces of the compounds. Since In and P elements are representatives of different groups, they are amenable to the action of oxidising agents. This is because of the nature of their redox properties. The component with the lower redox potential will oxidise first. At the same time, to maintain electroneutrality, the second component will pass into the solution simultaneously with it. Since the standard electrode potential of group III elements has a negative value and lower values of the potential of group V elements, In will be oxidised first. It should be noted that indium is characterised by moderate chemical activity and is resistant to water and air. During the electrolytic treatment of InP in a hydrofluoric acid solution, in the first stages of etching, a dense oxide film is formed, presumably of In_2O_3 oxide with $InPO_3$ inclusions. On the other hand, phosphorus reacts better with electrolyte anions, so its sublattice is etched faster. With an already formed In_2O_3 film, an interaction takes place between oxide and phosphorus diffusing from the bulk of the crystal, which can lead to the release of free indium, metallization of the growing layer on the crystal surface, and removal of phosphorus into the electrolyte solution. As a result, there is an excessive content of indium in the oxide layers.

It is obvious that the crystal lattices of indium phosphide and oxide have a significant mismatch. This leads to an appearance of excess stress. In addition, the film is loosely adhered to the substrate. As a result, we observe delamination and "spread" of the film upon further etching of the sample.

In_2O_3 is quite resistant to dilute acids; however, the current forms pores on its surface, it becomes soft and fragile (which is well demonstrated in Fig. 1b).

It is not the chaotic spreading of the oxide film that seems interesting, but the formation of even parallel steps equidistant from each other. In addition, there is a longitudinal uniform displacement of adjacent steps relative to each other. It is possible that such a periodicity of the structures is due to the concentration inhomogeneity of the impurity distribution in the bulk of indium phosphide. When a crystal uses the Czochralski method, a peculiarity of the distribution of the main (In, P) and minor (S) components is observed. In the direction from the centre to the periphery, the concentration of charge carriers increases, and their mobility decreases (a consequence of the temperature gradient). In addition, long-range elastic mechanical stresses prevent the formation of concentration and geometrically homogeneous single crystal. The sources of these mechanical stresses are dislocations (and their multiplication), which arise at internal growth defects. As a result, the crystal has a banded internal structure, in which areas with normal and high levels of dopant impurity concentration alternate.

When such a crystal is etched, areas with an increased concentration of impurities will be etched out faster. As a result, they will be very porous and have a low

phosphorus content. These areas are the initial sources of the formation of the oxide film. In these areas, the oxide layer has the greatest adhesion to the surface. This explains the sticking of oxide steps in the bands of segregation inhomogeneity.

3.2. The Mechanism of Formation of the Periodic Structure

Let us consider in detail a possible mechanism for the formation of a periodic structure of defects near or on the sample surface. As an initial hypothesis, we will accept the assumption that the geometric shape of such a structure is identical to the shape of the surface "parquet" structure.

The sample surface coincides with the crystal face (111). In this case, the faces of conservative slip of edge dislocations for the cubic crystal structure of sphalerite (InP) are located towards the sample surface, as shown schematically in Fig. 2.

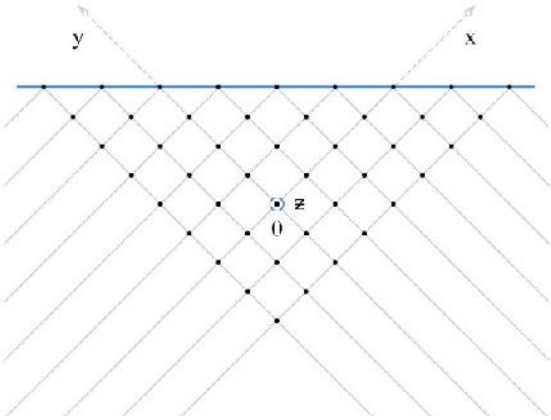

Fig. 2. Slip faces of edge dislocations in a cubic crystal structure.

Let us assume that at a sufficient distance from the surface (comparable to the sample thickness) there is a source of rectangular dislocation loops. The mechanism of operation of this source of dislocation loops is described in detail in [36]. The sliding system of these loops is a lateral surface of a prism composed of crystal planes (101), (110) (Fig. 3a).

As a result of repulsive interaction, the loops will spread along the sliding system from the source to the opposite surface of the sample. We will call the first loop (the most distant from the source) the "head" one, the next one – "upcoming". The movement of the loops will stop after one of the sides of the head loop comes out onto the surface of the sample (Fig. 3b). A step is formed on the sample surface, and the other three dislocations forming the loop will be fixed. As a result, the following (upcoming) dislocation loops will stop moving in the slip system and form a cluster.

Before the emergence of the head dislocation loop on the sample surface, the relative position of the head and the upcoming loops is symmetric toward the [010] and [001] directions (the OY and OZ axes). As a result, the superposition of the components of the Peach-Keller forces affecting the sections of the incident dislocation loop from the side of the stress field of the head dis-

location loop will be zero for all directions, except for [100] (the OX axis). This means that until the head dislocation loop emerges on the surface, the upcoming loop will not shift along the OY and OZ axes (Fig. 3a).

After the head dislocation loop emerges on the surface, the symmetry of the mutual arrangement of the upcoming and head dislocation loops will be broken. As a result, it will become possible to displace the upcoming dislocation loop along the OY axis (Fig. 3a).

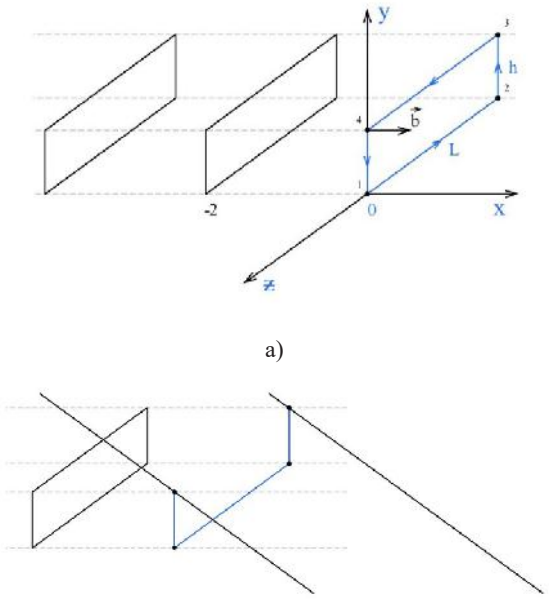

Fig. 3. Rectangular dislocation loops (a) and fixation of the head dislocation loop of a cluster on the sample surface (b).

Let us apply the expression for the components of the Peach-Keller force affecting per unit length of the dislocation line:

$$f_i = e_{ikl}\tau_k\sigma_{lm}b_m, \qquad (1)$$

where e_{ikl} is the Levi-Civita symbol (antisymmetric Kronecker symbol); τ_k are the components of the unit vector of the tangent to the dislocation line; σ_{lm} – components of the tensor of mechanical stresses external toward the dislocation; b_m – components of the dislocation Burgers vector. This expression applies Einstein's rule for summation using paired (occurring twice) indices. Indices can take on the values {x, y, z}.

As a result, the superposition of the components of the Peach-Keller force affecting the individual sections of the upcoming dislocation loop along the OY axis gives the expression:

$$F_y = -b^2 B \frac{h\left(3d^2+h^2\right)}{\left(d^2+h^2\right)^2} L, \qquad B = \frac{\mu}{2\pi\left(1-\sigma\right)}, \qquad (2)$$

where b is the modulus of the Burgers vector of the dislocation loop; μ is the shear modulus of the sample material; σ is the Poisson's ratio of the sample material; h is

the size of the dislocation loop along the OY axis; d is the distance between the head and the upcoming dislocation loops; L is the size of the dislocation loop along the OZ axis.

Thus, it becomes possible for the upcoming dislocation loop to shift in the negative direction of the OY axis. After the upcoming dislocation loop descends below the ZOX face, the component of the Peach-Keller force will affect section (1-2) of the dislocation loop in the negative direction of the OY axis.

$$F_y^{(1-2)} = -b^2 B \frac{(h+y_0)\left[3d^2 + (h+y_0)^2\right]}{\left[d^2 + (h+y_0)^2\right]^2} L, \quad (3)$$

where y_0 is the modulus of the distance from section (3-4) of the upcoming dislocation loop to the ZOX face.

The component of the Peach-Keller force will affect section (3-4) of the dislocation loop in the positive direction of the OY axis:

$$F_y^{(3-4)} = b^2 B \frac{y_0\left(3d^2 + y_0^2\right)}{\left(d^2 + y_0^2\right)^2} L. \quad (4)$$

If the condition is met

$$F_y^{(1-2)} + F_y^{(3-4)} = 0. \quad (5)$$

The upcoming dislocation loop will stop at a distance y_0 below the ZOX face. It will enter the slip system, without the obstacle in the form of the head loop of the cluster, and under the influence of the next upcoming dislocation loop, it will be able to continue sliding in it until it reaches the sample surface.

In the initial slip system, the place of the upcoming dislocation loop, which "dived" under the head dislocation loop, will be taken by the next dislocation loop of the cluster. It will repeat the described "diving" process twice and will also come to the surface of the sample.

A similar displacement will be performed by the next upcoming dislocation loop, and so on.

Under the condition of constant action of the source of dislocation loops [36], periodic areas of inhomogeneous deformation are formed on the sample surface, caused by the periodic elastic field of the system of dislocation loops, which partially emerged on the sample surface and fixed on it (Fig. 4a). Another option may be the formation of nanorelief in the form of periodic parallel steps (Fig. 4b).

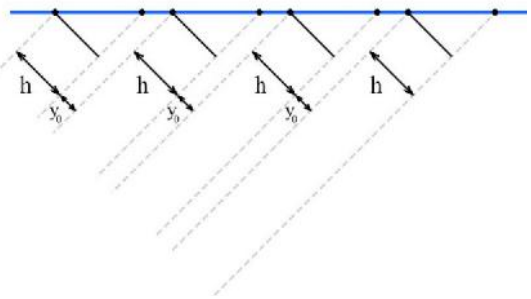

a)

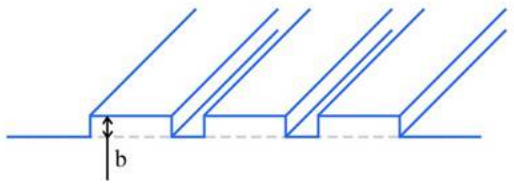

b)

Fig. 4. A system of dislocation loops fixed on the sample surface (a) and Periodic nano-steps on the sample surface (b).

The length of the nanosteps is equal to the length L of sections (1-2) and (3-4) of dislocation loops parallel to the OZ axis.

Let us find the value y_0 to estimate the distance between the nanosteps on the sample surface.

An attempt to directly solve Eq. (5) leads to an algebraic equation of the sixth degree. Its numerical coefficients depend on h and d – the values of the geometric parameters of the accumulation of dislocation loops. This makes it impossible to obtain a general analytical solution that demonstrates the relationship of these parameters in a general way. For each specific set of numerical values of the parameters, a numerical solution is possible.

There is another way to make an overall estimate of the value of y_0. To perform this estimate, we investigate the general expression for the Peach-Keller force acting on the sections of the dislocation loop parallel to the OZ axis:

$$F(y) = \pm b^2 B \frac{y\left(3d^2 + y^2\right)}{\left(d^2 + y^2\right)^2} L, \qquad (6)$$

where y is the ordinate of a section of the dislocation loop parallel to the OZ axis. The plus or minus sign is selected depending on the direction of the dislocation line.

The function $F(y)$ has two extreme points:

$$y_1 = \sqrt{\left(2\sqrt{3} - 3\right)} d \approx 0,681d ;$$

$$y_2 = -\sqrt{\left(2\sqrt{3} - 3\right)} d \approx -0,681d .$$

Taking into account the signs of expressions (3) and (4), we determine that at the points with ordinates y_2 the component $F^{(1-2)}$ has a maximum, and the component $F^{(3-4)}$ has a minimum. Thus, it can be estimated that, for all units

$$y_0 = 0,681d - \frac{h}{2}, \qquad (7)$$

the dislocation loop will be in a state of stable equilibrium relative to the displacement along the OY axis (Fig. 5).

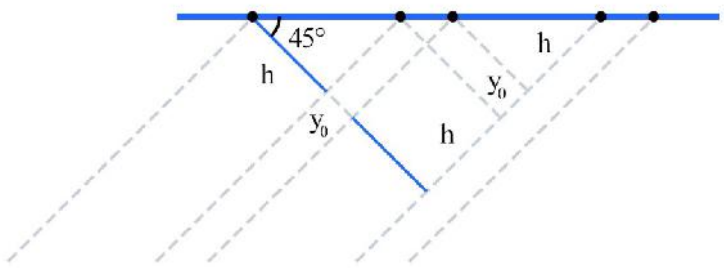

Fig. 5. Position of the upcoming dislocation loop after "diving" under the head loop, before reaching the sample surface.

Since the slip planes and the sample surface form an angle of 45°, the distance between adjacent parallel nanosteps can be estimated as:

$$l = \sqrt{2}y_0 = \sqrt{2}\left(0,681d - 0,5h\right). \qquad (8)$$

If there are no other defects in the crystal lattice of the sample, except for the accumulation of dislocation loops in their common slip system (Fig. 3a), then the superposition of the components of the Peach-Keller force displacing the loop along the OZ axis is zero.

In the presence of other defects in the bulk of the sample, or on its surface, the symmetry of the mutual arrangement of the head and upcoming dislocation loops will be violated. Such violation can lead to a nonzero superposition of the components of the Peach-Keller force displacing the loop along the OZ axis. In the simplest case, the initial relative displacement of the head and upcoming loops along the OZ axis is sufficient for this (Fig. 4a).

Thus, we can explain the longitudinal displacement of the nanowires observed on the sample surface after etching. The displacement of the upcoming dislocation loops in the ZOY face is carried out due to the shift and stops after the loop partially emerges onto the sample surface (Fig. 5). Accordingly, it is reasonable to assume that the value of the longitudinal displacement (along the OZ axis) for the incident dislocation loop *SS* will be close to the displacement along the OY axis and along the OX axis (Fig. 6):

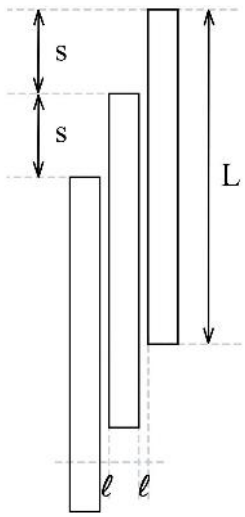

Fig. 6. Relative displacement of the head and upcoming dislocation loops along the OZ axis.

$$S = 2\left(h + y_0\right) = 2\left(0,5h + 0,681d\right). \quad (9)$$

Taking into account the fact that the cut-off radius of the elastic fields of the head dislocation loop, which partially emerged on the surface of the sample, is approximately equal to h, we take $d \approx h$ for a numerical estimate using Eqs. (8) and (9).

In this case, we get:

$$l \approx 0,256h \; ; \; S \approx 2,362h \; . \quad (10)$$

These estimates correspond closely to the experimental results shown in Fig. 1.

CONCLUSIONS

1. The paper demonstrates the possibility of forming specific nanostructures of the "parquet" type of nanowires on the InP surface. Their morphological and chemical parameters have been studied.
2. According to the results of scanning electron microscopy, it has been found that the thickness of each wire is about 10 microns, the height is up to 10 microns, and the length is between 100 and 130 microns. The distance between the parquet layers is 20 to 50 microns.
3. EDAX shows an excess of indium in the periodic oxide layers. The shift in stoichiometry toward excess indium is explained by the faster etching of the phosphorus sublattice.

The resulting nanostructure is characterised by an ordered transverse and longitudinal relative displacement of individual nanowires. A dislocation model is proposed to explain the mechanism of formation of such structure. The numerical estimates of the geometric parameters of the nanostructure obtained during theoretical modelling are adequate for the experimental results.

ACKNOWLEDGMENTS

The study has been supported by the Ministry of Education and Science of Ukraine via Project No. 0122U000129 "The Search for Optimal Conditions for Nanostructure Synthesis on the Surface of A3B5, A2B6 Semiconductors and Silicon for Photonics and Solar Energy". In addition, the research of A.I.P. and Y.S. has been partly supported by COST Action CA20129 "Multiscale Irradiation and Chemistry Driven Processes and Related Technologies" (MultiChem). Furthermore, A.I.P. also thanks HORIZON 2020 RISE-RADON Project "Irradiation Driven Nanofabrication: Computational Modelling Versus Experiment" for partial support.

REFERENCES

1. Monaico, E., Tiginyanu, I., & Ursaki, V. (2020). Porous Semiconductor Compounds. *Semiconductor Science and Technology*, 35 (10), 103001. doi: 10.1088/1361-6641/ab9477
2. Deng, T., Li, M., Wang, Y., & Liu, Z. (2015). Development of Solid-State Nanopore Fabrication Technologies. *Science Bulletin*, 60 (3), 304–319. doi: 10.1007/s11434-014-0705-8

3. Dolgyi, A., Bandarenka, H., Prischepa, S., Yanushkevich, K., Nenzi, P., Balucani, M., & Bondarenko, V. (2012). Electrochemical Deposition of Ni into Mesoporous Silicon. *ECS Transactions*, *41* (35), 111.
4. Shimanovich, D. L., Vorobjova, A. I., Tishkevich, D. I., Trukhanov, A. V., Zdorovets, M. V., & Kozlovskiy, A. L. (2018). Preparation and Morphology-Dependent Wettability of Porous Alumina Membranes. *Beilstein Journal of Nanotechnology*, *9* (1), 1423–1436.
5. He, Y., Tsutsui, M., Zhou, Y., & Miao, X. S. (2021). Solid-State Nanopore Systems: From Materials to Applications. *NPG Asia Materials*, *13* (1), 1–26. DOI: 10.1038/s41427-021-00313-z
6. Plesa, C., Verschueren, D., Pud, S., Van Der Torre, J., Ruitenberg, J. W., Witteveen, M. J., ... & Dekker, C. (2016). Direct Observation of DNA Knots Using a Solid-State Nanopore. *Nature Nanotechnology*, *11* (12), 1093–1097. DOI: 10.1038/nnano.2016.153
7. Zavatski, S., Popov, A. I., Chemenev, A., Dauletbekova, A., & Bandarenka, H. (2022). Wet Chemical Synthesis and Characterization of Au Coatings on Meso- and Macroporous Si for Molecular Analysis by SERS Spectroscopy. *Crystals*, *12* (11), 1656.
8. Ochs, D., Brause, M., Krischok, S., Stracke, P., Maus-Friedrichs, W., Puchin, V., ... & Kempter, V. (1998). Characterization of LiF and CaF2 Surfaces Using MIES and UPS (HeI). *Journal of Electron Spectroscopy and Related Phenomena*, *88*, 725–732.
9. Kozlovskiy, A., Kenzhina, I., Kaikanov, M., Stepanov, A., Shamanin, V., Zdorovets, M., & Tikhonov, A. (2018). Effect of Electronic Modification on Nanostructures Stability to Degradation. *Materials Research Express*, *5* (7), 075010.
10. Suchikova, Y., Kovachov, S., Bohdanov, I., Karipbaev, Z. T., Pankratov, V., & Popov, A. I. (2023). Study of the Structural and Morphological Characteristics of the CdxTeyOz Nanocomposite Obtained on the Surface of the CdS/ZnO Heterostructure by the SILAR Method. *Applied Physics A*, *129* (7), 499.
11. Suchikova, Y., Kovachov, S., Bohdanov, I., Popova, E., Moskina, A., & Popov, A. (2023). Characterization of CdxTeyOz/CdS/ZnO Heterostructures Synthesized by the SILAR Method. *Coatings*, *13* (3), 639.
12. Usseinov, A.B.; Akilbekov, A.T.; Kotomin, E.A.; Karipbayev, Z.T. (2019). The First Principles Calculations of CO_2 Adsorption on (1010) ZnO Surface. *AIP Conf. Proc.*, *2174*, 020181.
13. Klym, H., Ingram, A., Hadzaman, I., Karbovnyk, I., Vasylchyshyn, I., & Popov, A. I. (2019). Nanoporous Characterization of Modified Humidity-Sensitive MgO-Al2O3 Ceramics by Positron Annihilation Lifetime Spectroscopy Method. *IOP Conference Series: Materials Science and Engineering*, *503* (1), 012019.
14. Žalga, A., Abakevičienė, B., Žarkov, A., Beganskienė, A., Kareiva, A., & Tamulevičius, S. (2011). On the Properties of Yttria-Stabilized Zirconia Thin Films Prepared by Sol-Gel Method. *Medziagotyra*, *17* (2), 191–196.
15. Villarroel, R., Espinoza-Gonzalez, R., Lisoni, J., & Gonzalez-Moraga, G. (2018). Influence of the Oxygen Consumption on the Crystalline Structure of Titanium Oxides Thin Films Prepared by DC Reactive Magnetron Sputtering. *Vacuum, 154*, 52–57. doi: https://doi.org/10.1016/j.vacuum.2018.04.049
16. Suzuki, K., Sato, S., & Fujita, M. (2010). Template Synthesis of Precisely Monodisperse Silica Nanoparticles within Self-Assembled Organometallic Spheres. *Nature Chemistry*, *2* (1), 25–29. doi: 10.1038/nchem.446
17. Wei, C., Wu, G., Yang, S., & Liu, Q. (2016). Electrochemical Deposition of Layered Copper Thin Films Based on the Diffusion Limited Aggregation. *Scientific Reports*, *6* (1), 1–7. doi: 10.1038/srep34779
18. Ivanou, D. K., Streltsov, E. A., Fedotov, A. K., Mazanik, A. V., Fink, D., & Petrov, A. (2005). Electrochemical Deposition of PbSe and CdTe Nanoparticles onto p-Si (100) Wafers and into Nanopores in SiO_2/Si (100) Structure. *Thin Solid Films*, *490* (2), 154–160. doi: 10.1016/j.tsf.2005.04.046

19. Suchikova, Y.A., Kidalov, V.V., & Sukach, G.A. (2010). Influence of the Carrier Concentration of Indium Phosphide on the Porous Layer Formation. *Journal of Nano- and Electronic Physics*, *2* (4), 75–81.
20. Sato, T., Zhang, X., Ito, K., Matsumoto, S., & Kumazaki, Y. (2016). Electrochemical Formation of N-Type GaN and N-Type InP Porous Structures for Chemical Sensor Applications. *2016 IEEE Sensors,* (1–3). IEEE. doi: 10.1109/ICSENS.2016.7808443
21. Lee, E., Menumerov, E., Hughes, R. A., Neretina, S., & Luo, T. (2018). Low-Cost Nanostructures from Nanoparticle-Assisted Large-Scale Lithography Significantly Enhance Thermal Energy Transport across Solid Interfaces. *ACS Applied Materials & Interfaces*, *10* (40), 34690–34698. doi: 10.1021/acsami.8b08180
22. Monaico, E., Monaico, E. I., Ursaki, V. V., Tiginyanu, I. M., & Nielsch, K. (2019). Electrochemical Deposition by Design of Metal Nanostructures. *Surface Engineering and Applied Electrochemistry*, *55* (4), 367–372. doi: 10.3103/S1068375519040070
23. Suchikova, Y., Vambol, S., Vambol, V., & Mozaffari, N. (2019). Justification of the Most Rational Method for the Nanostructures Synthesis on the Semiconductors Surface. *Journal of Achievements in Materials and Manufacturing Engineering*, *92* (1–2), 19–28. doi: 10.5604/01.3001.0013.3184
24. Šimkiene, I., Kindurys, A., Treideris, M., & Sabataityte, J. (2008). Formation of Porous n-A_3B_5 Compounds. *Acta. Phys. Pol. A*, *3* (113), 1085–1090.
25. Delimitis, A., Komninou, P., Kehagias, T., Pavlidou, E., Karakostas, T., Gladkov, P., & Nohavica, D. (2008). Controlled Growth of Porous Networks in Phosphide Semiconductors. *Journal of Porous Materials*, *15* (1), 75–81. doi: 10.1007/s10934-006-9054-6
26. Ben Amara, E., Lebib, A., & Beji, L. (2020). Structural and Electrical Investigation of Porous GaAs Layers on Different Crystallographically Oriented GaAs Substrates. *Journal of Electronic Materials*, *49* (9), 5281–5292. doi: 10.1007/s11664-020-08294-5
27. Weng, Z., Chai, X., Liu, L., Li, L., Xu, H., Song, Z., & Liang, K. (2017). Effects of Temperature and Current Density on the Porous Structure of InP. *Journal of Solid State Electrochemistry*, *21*, 545–553. doi: 10.1007/s10008-016-3387-0
28. Praveenkumar, S., Lingaraja, D., Mathi, P. M., & Ram, G. D. (2019). An Experimental Study of Optoelectronic Properties of Porous Silicon for Solar Cell Application. *Optik*, *178*, 216–223. doi: 10.1016/j.ijleo.2018.09.176
29. Gerngross, M. D., Carstensen, J., & Föll, H. (2012). Electrochemical and Galvanic Fabrication of a Magnetoelectric Composite Sensor Based on InP. *Nanoscale Research Letters*, *7* (1), 1–5. doi: 10.1186/1556-276X-7-379
30. Korotcenkov, G., & Cho, B. K. (2010). Porous Semiconductors: Advanced Material for Gas Sensor Applications. *Critical Reviews in Solid State and Materials Sciences*, *35* (1), 1–37. doi: 10.1080/10408430903245369
31. Suchikova, J.A. (2015). Synthesis of Indium Nitride Epitaxial Layers on a Substrate of Porous Indium Phosphide. *Journal of Nano- and Electronic Physics*, *7* (3), 03017.
32. Cheng, H., Xiao, R., Bian, H., Li, Z., Zhan, Y., Tsang, C. K., ... & Li, Y. Y. (2014). Periodic Porous Silicon Thin Films with Interconnected Channels as Durable Anode Materials for Lithium Ion Batteries. *Materials Chemistry and Physics*, *144* (1–2), 25–30. doi: 10.1016/j.matchemphys.2013.12.003
33. Schmuki, P., Erickson, L. E., & Lockwood, D. J. (1998). Light Emitting Micropatterns of Porous Si Created at Surface Defects. *Physical Review Letters*, *80* (18), 4060. doi: 10.1103/PhysRevLett.80.4060
34. Suchikova, J.A., Kidalov, V.V., & Sukach, G.A. (2009). Blue Shift of Photoluminescence Spectrum of Porous InP. *ECS Transactions*, *25* (24), 59–64. doi: 10.1149/1.3316113

35. Vambol, S., Bogdanov, I., Vambol, V., Suchikova, Y., Kondratenko, O., Hurenko, O., & Onishchenko, S. (2017). Research into Regularities of Pore Formation on the Surface of Semiconductors. *Eastern-European Journal of Enterprise Technologies*, *3* (5–87), 37–44. doi: 10.1134/S1063782611010192
36. Yana, S. (2016). Porous Indium Phosphide: Preparation and Properties. *Handbook of Nanoelectrochemistry: Electrochemical Synthesis Methods, Properties, and Characterization Techniques*, 283–306. doi: 10.1007/978-3-319-15266-0_9
37. Lazarenko, A.S., Mikhailovskij, I.M., Rabukhin, V.B., & Velikodnaya, O.A. (1995). Nanotopography and Grain-Boundary Migration in the Vicinity of Triple Junctions. *Acta Metallurgica Et Materialia, 43* (2), 639–643. doi: 10.1016/0956-7151(94)00228-A
38. Suchikova, Y.A., Kidalov, V.V., & Sukach, G.A. (2011). Influence of Dislocations on the Process of Pore Formation in n-InP (111) Single Crystals. *Semiconductors*, *45* (1), 121–124. doi: 10.1134/S1063782611010192

sciendo

LATVIAN JOURNAL OF PHYSICS
AND TECHNICAL SCIENCES
2024, N 5

DOI: 10.2478/lpts-2024-0033

RECENT WORKS ON DIRECT-WRITE DIGITAL HOLOGRAPHY

R. Bakanas[1], A. Nikolskij[1], A. Bulanovs[2*],
D. Brotherton-Ratcliffe[1]

[1] Geola Digital Ltd.,
41 Naugarduko Str., Vilnius, LT03227, LITHUANIA
[2] Daugavpils University,
Institute of Life Sciences and Technology,
1a Parades Str., Daugavpils, LV5401, LATVIA
*e-mail: andrejs.bulanovs@du.lv

Direct-write digital holographic (DWDH) printing is a highly flexible technique for the generation of photoresist masters, which are required to produce the metallic shims used for the mass production of holograms in the security and packaging industries. Here we describe a new type of holographic feature, which can be combined with any other feature printable using DWDH: full-parallax, full-colour transmission masters containing limited animation. We will also describe a technique to print the fringe pattern of each hogel without using a reference beam. By programming the required fringe calculation algorithm on a graphics card using CUDA, we obtain acceptable calculation times. The advantage of using such direct fringe writing is that once again DWDH allows extra features to be written onto a master and combined with other features to produce a stronger security solution. Finally, we present results concerning the use of hogel image dithering to improve the grey-scale performance of DWDH printers.

Keywords: *Digital hologram, direct-write holography, DWDH, image-matrix lithography, holographic printer, photoresist, security holography.*

1. INTRODUCTION

The technique of writing digital reflection holograms as a matrix of small adjacent elemental holograms (now known as 'hogels') was first demonstrated by Yamaguchi et al. [1] (JP) in 1990. These early experiments, although monochromatic, slow, and employing contact apertures, led the way to the development of what is today known as DWDH or Direct-Write Digital Holography [2], [3]. In the late 1990s, Klug et al. (USA) working at Zebra Imaging Inc and Brotherton-Ratcliffe et al. [4] (LT) working at Geola UAB improved Yamagushi's technique to allow the production of large-format high-quality full-colour reflection holograms having relatively large hogels (0.8 mm–1.6 mm). DWDH was subsequently developed at Geola Digital UAB (LT) by Stanislovas Zacharovas et al. [5]–[9] to produce high-resolution digital master holograms for security applications. Here the hogel size was reduced to 100 microns, and photoresist was used as the recording medium. This work has led directly to the recent availability of commercial security mastering machines known as DIWO (Direct Write Originator), which complement the well-known techniques of E-beam [10], Dot-Matrix [11]–[13] and Image-Matrix or Kinemax [14] technology, currently in use by much of the holographic security industry. The combination of DIWO technology with Image-Matrix Lithography and a fast blue pulsed laser allows the rapid writing of all security features from Level 1 to Level 4 in a security master including achromatic and deep 3D HPO colour images with covert optical security features.

2. EXPERIMENTAL

Current DWDH security origination is commercially available through Geola's DIWO-6 originator (Fig. 1). This machine typically uses a DPSS SLM 440 nm blue pulsed laser operating at 30–120 Hz for fast origination of security masters, employs a sequential inscription of holograms, each comprising an ensemble of elemental parts called hogels or holopixels (Fig. 2).

As in all DWDH systems, the hogel constitutes a fundamental holographic optical unit akin to a pixel in a digital image but differs by offering varying visual representations from different viewing angles, paralleling the behaviour of conventional analogue holographic elements. Given the limitations of the human eye in discerning small detail, the selected size of the holographic unit (hogel) for master-original printing in DIWO-6 is chosen to be 100 x 100 microns. This dimension allows for the projection of extremely high quality distinct visual perspectives depending on the viewing angle. The underlying mechanism of the recording scheme is depicted in Fig. 3.

The high numerical aperture Fourier-Transform objective lens used by DIWO-6 projects a focal point beyond its physical extent. Around this focal spot, light beams emitted from each pixel on a Spatial Light Modulator (SLM) maintain a near identical size and directional consistency. Introducing a reference beam to this focal point allows for the inscription of a hogel as a holographic optical element that, when illuminated, directs light beams along the paths established during recording.

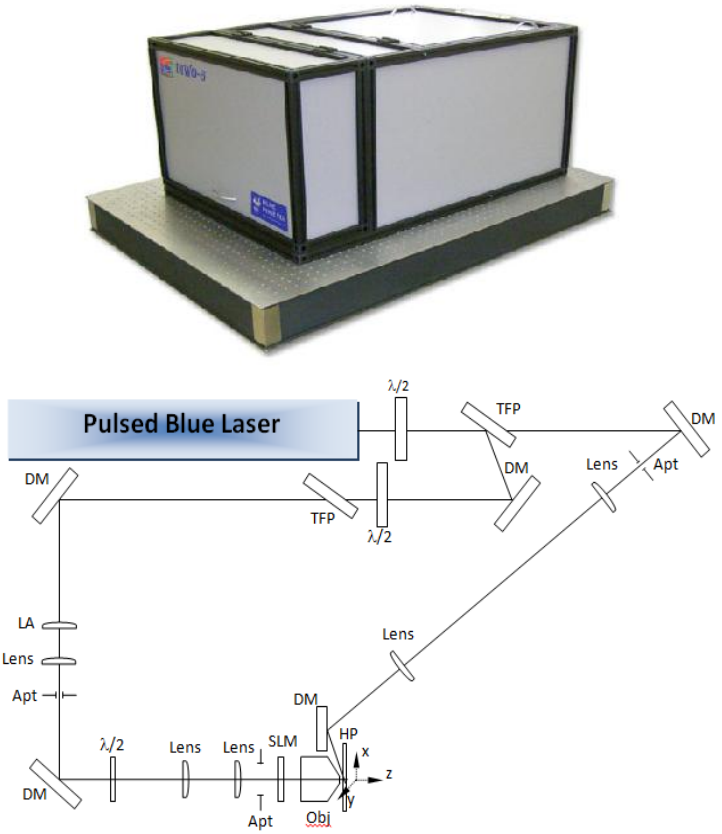

Fig. 1. DIWO-6 DWDH Originator (above) and simplified optical scheme (below). DM = dielectric mirrors, TFP = thin film polarizer, λ/2 = half wave plate, SLM = spatial light modulator, Obj = Fourier transform objective, Lens = lenses, Apt = aperture, LA = lens array, HP = holographic plate.

For the generation of the SLM image required for the inscription of each specific hogel, Geola employs a collection of parallax-related 2D images of the 3D scene, captured from various viewing angles along a horizontal line (either using a moving digital camera for real world scenes or a virtual camera in CAD software). Corresponding pixels are extracted from each 2D parallax-related image and merged into a new "pixel-swapped" image displayed on the SLM. When illuminated, each hogel then replays these 2D pixel images at their corresponding angles. The viewer's binocular vision interprets these parallax-related 2D images as a 3D scene (HPO – horizontal parallax only).

An HPO hologram of a 3D object produced using this method usually contains 200 to 800 parallax-related views, thus eliminating any unwanted image transition effects, unless intentionally introduced. This streamlined holographic recording process can swiftly yield effects unachievable with other origination techniques. These include high-resolution 3D images that are:

- bright and highly diffractive;
- capable of motion replay;
- deep;
- colour-rich;
- grayscale;
- mixed grayscale and colour;
- front and back illuminated grayscale and colour (for transparent films).

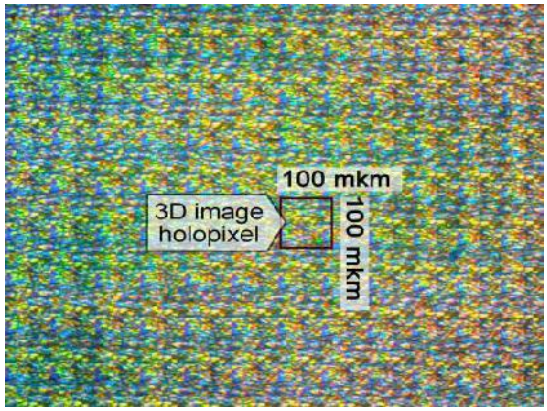

Fig. 2. Microphotographs of an embossed 3D image hologram originated with Geola's DIWO-6 – Direct Write Originator. Note that the hologram is made up of a raster of 100 micron x 100 micron hogels.

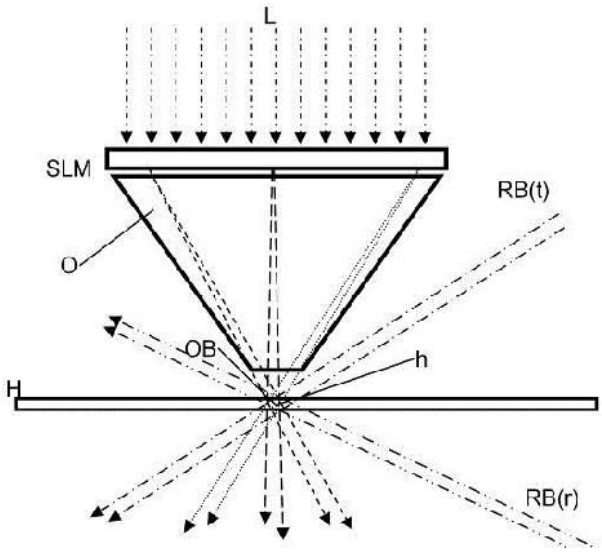

Fig. 3. Writing a hogel for a DWDH hologram. L – the laser beam, OB the object beam, RB(t) and RB(r) – reference beams for transmission and reflection holograms, respectively; h – a hogel, H – the white-light reflection or transmission hologram.

3. RESULTS AND DISCUSSION

3.1. Full-Parallax Optically-Variable Achromatic 3D Images now Available in DWDH Originators

Traditional dogma dictates that reflection holograms are able to support the display of full-parallax images, but transmission holograms must sacrifice the vertical parallax in order to avoid image blurring (as dispersion is much higher in the vertical dimension). Whilst this dogma is certainly true in principle, dispersion of a full

parallax DWDH hologram of vanishingly small depth is zero. In fact, the dispersion in the vertical dimension of a hologram with a moderate reference angle (e.g., wall-mounted) only blurs the holographic image unacceptably after a small but finite image depth. In the context of small security and packaging holograms, it turns out that the critical depth available is enough to support optically-variable full-parallax achromatic images with acceptable blurring. Practically this technique can be implemented on existing DIWO-6 machines with only a software upgrade. The technique consists of using a standard full-parallax animated dataset for the required achromatic scene (as used in standard DWDH full-colour full-parallax printers) and using the calculated SLM images as data for the DIWO-6's unique SLM. Figures 4 and 5 show an animated watch hologram produced with the new software created for the DIWO-6. By moving the hologram around in your hands, the image appears clearly full-parallax and in addition the watch hands rotate around the clock face. This feature is a distinct improvement over the HPO images available previously as moving the hologram simulates a real watch. Previous HPO holograms available on photoresist masters showed no motion or parallax change with a vertical tilting of the hologram and as such did not correctly simulate objects such as a watch with moving watch hands.

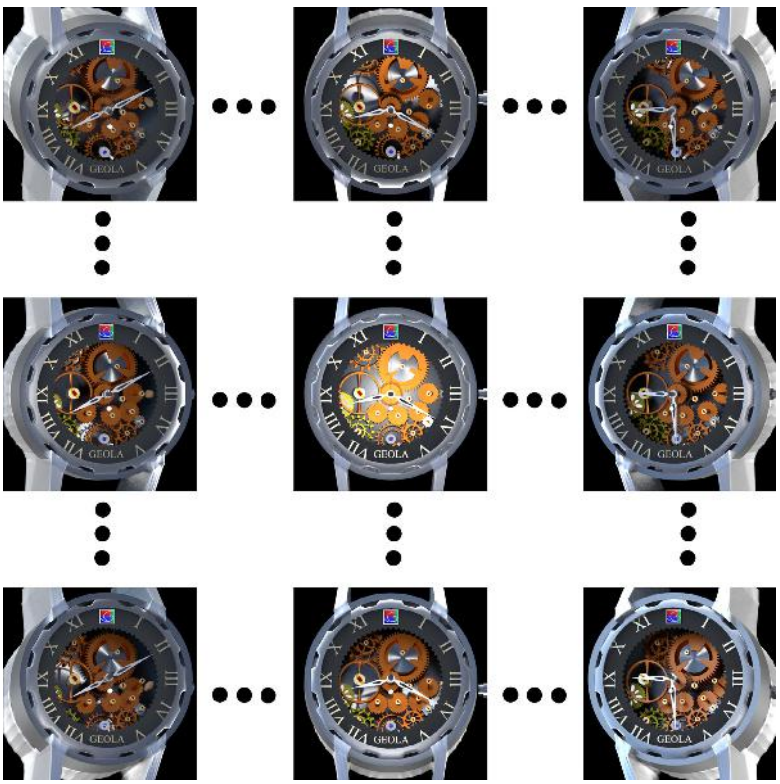

Fig. 4. Full-Parallax Perspective View Renders of the hologram of Fig. 5. Note that the position of the watch hands are arranged so that as the viewer tilts the hologram up and down and left to right, the hands rotate around the watch face.

Fig. 5. Full-Parallax Optically-Variable Hologram Labels (Left) and Master (Right). Digital DWDH Master made using DIWO-6 originator on photoresist.

3.2. Improving the Greyscale

One of the issues up to now of writing DWDH holograms onto photo-resist at the extremely small hogel sizes used in the DIWO-6 has been a less than optimal greyscale. Geola has now released a new software version for the DIWO-6, which significantly improves image greyscale. This has been done using a post-processing of the SLM images using Burke's algorithm for dithering. Since the DIWO-6 employs 100 micron hogels, its high-resolution SLM cannot be resolved on replaying the hologram due to digital diffractive blurring [2]. As such dithering the SLM images at the full resolution of the panel produces no angular degradation of the images. However, as with standard 2D dithering, significant improvements to greyscale are observed.

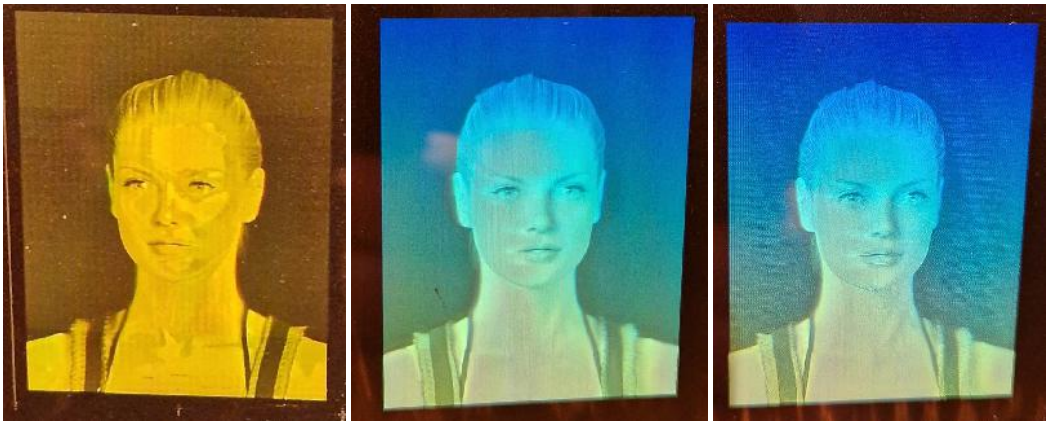

Fig. 6. Hologram recorded without Dithering (Left). With Dithering on Perspective View Images (Right). With Dithering on SLM Images (Centre).

Typical results are shown in Fig. 6 where on the left a hologram recorded without dithering can be seen. The poor greyscale is clearly visible as patches on the girl's face and chest. The centre photograph shows the result of dithering the SLM images using Burke's algorithm. Not only is the greyscale substantially improved, but

importantly there is absolutely no spatial image deterioration. As a comparison, the effect of dithering the raw perspective view images is shown on the right-hand image. Here we can see a clear improvement of the greyscale but at a cost to the spatial resolution.

3.3. Image-Matrix versus DWDH

Geola offers two types of security origination systems: the DIWO-6, which has been described above, and the IMP-6, which is an image matrix machine. The two machines are designed to be complimentary, and master holograms can be written and over-written on both machines. Together these machines allow all security features covering level 1 to 4 to be produced on the same master (see Figs. 7 and 8). The IMP-6 has two modes of operation – holographic and lithographic. These modes are switchable in real time, and so different parts of the shim can use different methods of operation. The highest resolution obtainable is 210,000 dpi. Complex optical security features with holographic images of shallow depth can be printed with the IMP-6 at moderate speed. The DIWO-6 adds deep holographic imagery at faster speeds.

Visibility	Verified by	Diffractive effects and elements	Level
Public (Overt)	Customer	True colour, 2D/3D, Bass-relief, E-beam motion, Guilloches, Lenses, Compass,	Level 1
Simple Aided verification (Obvious)	Specialists	Microtext, Smart glint, Letter lens, Laser readable image, ets	Level 2
Not obviously visible (Covert)	Inspectors	Nanotext, ets.	Level 3
Invisible without very special equipment	Forensic labs	Forensic features (holoframe size, shape, spacing, internal structures of the holoframe, grating period and angle, noise	Level 4

Fig. 7. The various levels of security features used in modern security holograms.

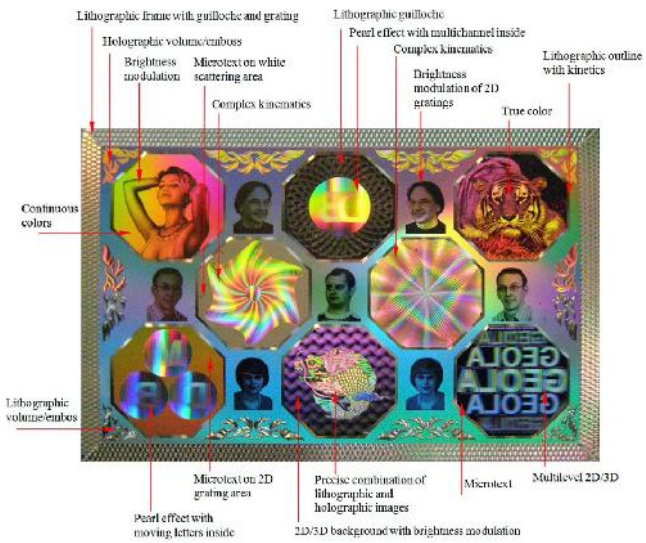

Fig. 8. Diffractive features producible by IMP-6.

3.4. Writing DWDH Holograms Using the Image Matrix IMP-6

Currently, in order to print deep holographic images on a security master, including the optically variable full-parallax holograms described above, a DWDH printer such as the DIWO-6 is required. We report here of our first attempts to print DWDH holograms on the image matrix machine IMP-6 using software data processing to calculate the interferometric fringe pattern of individual hogels. These fringe patterns are then imaged directly onto the photoresist using a 405nm laser. In the DIWO-6, the fringe pattern of the hogel is produced by the interaction of a reference and object beam.

The fringe pattern calculation is based on the fact that each DWDH hogel on replay essentially projects a 2D image of the recording SLM mask. The distance of the focal plane of this projection from the hogel is usually arranged to be in the range of the optimum viewing distance to infinity. A Fourier or Fresnel transform (as the case may be) of the SLM hogel data, therefore, defines the fringe pattern of the hogel.

Early attempts to calculate the hogel fringe pattern using Matlab and Fortran required a prohibitively long time. Due to the complexity and size of the fringe calculation, we, therefore, coded the calculation using CUDA, which then brought the calculation time down to a reasonable range on a small PC. As an example, Fig. 9 shows full-parallax perspective view data, which has then been converted to hogel fringe data as illustrated in Figs. 10 and 11.

The final hologram is shown in Fig. 12. It must be emphasised that this is the first test only and as such the quality of the hologram is not optimal. We are, however, optimistic that the quality can be significantly improved; as such DWDH holography features may plausibly be integrated into the IMP-6 in future generations.

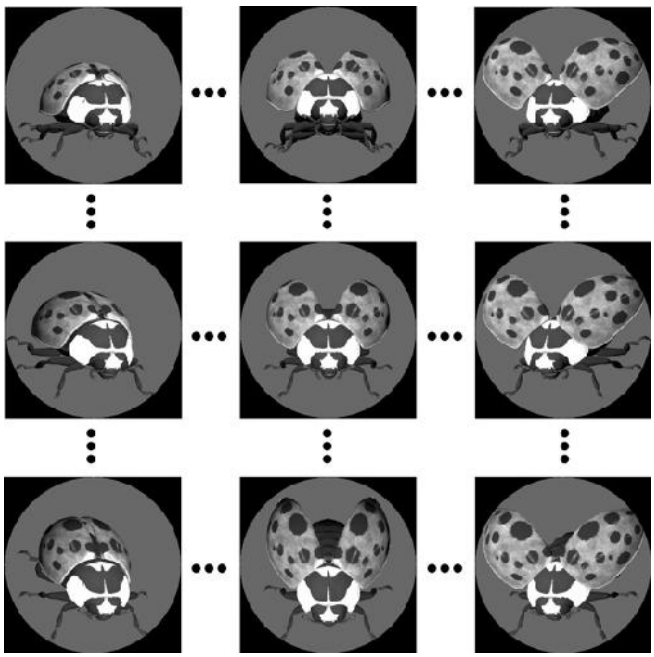

Fig. 9. Full Parallax Perspective View Data used to calculate DWDH hogel fringe patterns for subsequent lithographic inscription using the image matrix machine, IMP-6.

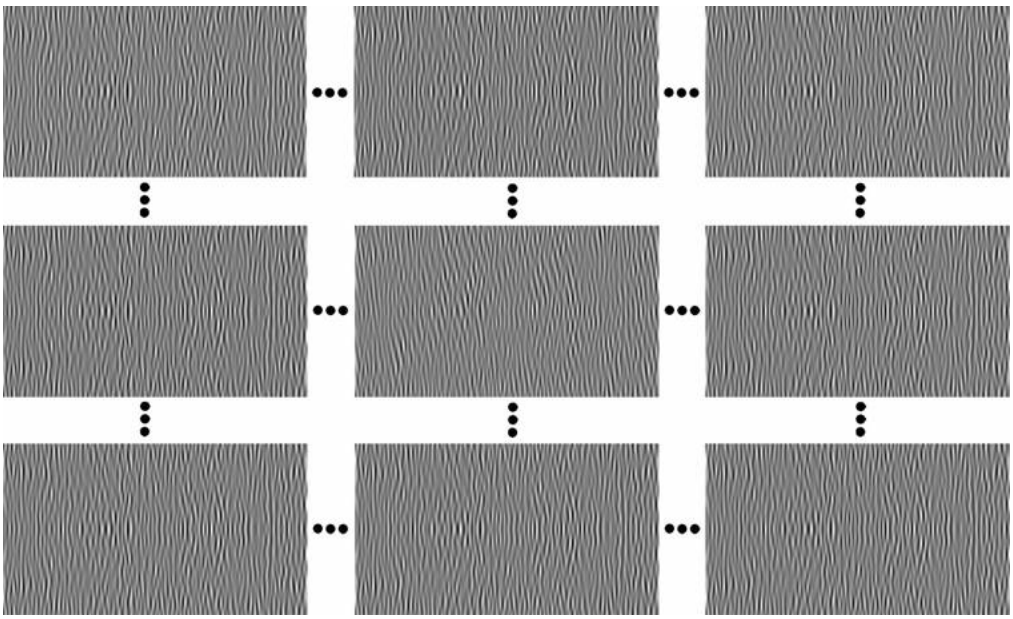

Fig. 10. 300 x 300 hogel fringe images calculated by a CUDA algorithm using the data of Fig. 9. This fringe data is then used by the IMP-6 to produce a 3cm x 3cm full-parallax achromatic transmission hologram master composed of 300 x 300 hogels, each of 100 micron diameter.

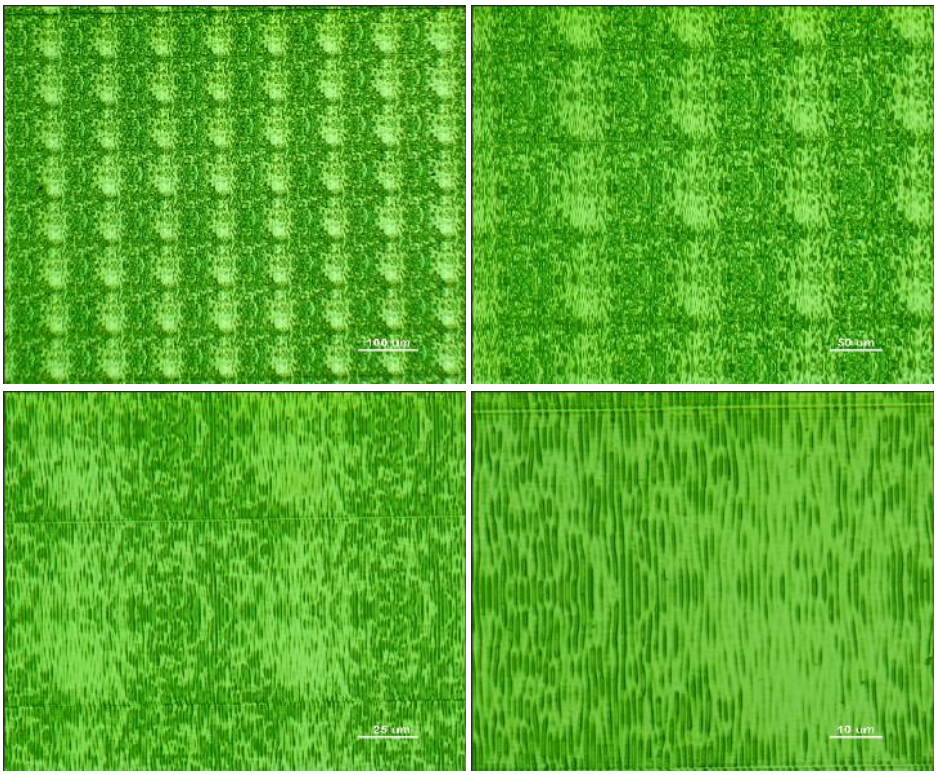

Fig. 11. The structure of a hologram consisting of DOE pixels at different magnifications. Images obtained using a metallurgical microscope under narrow band of green illumination.

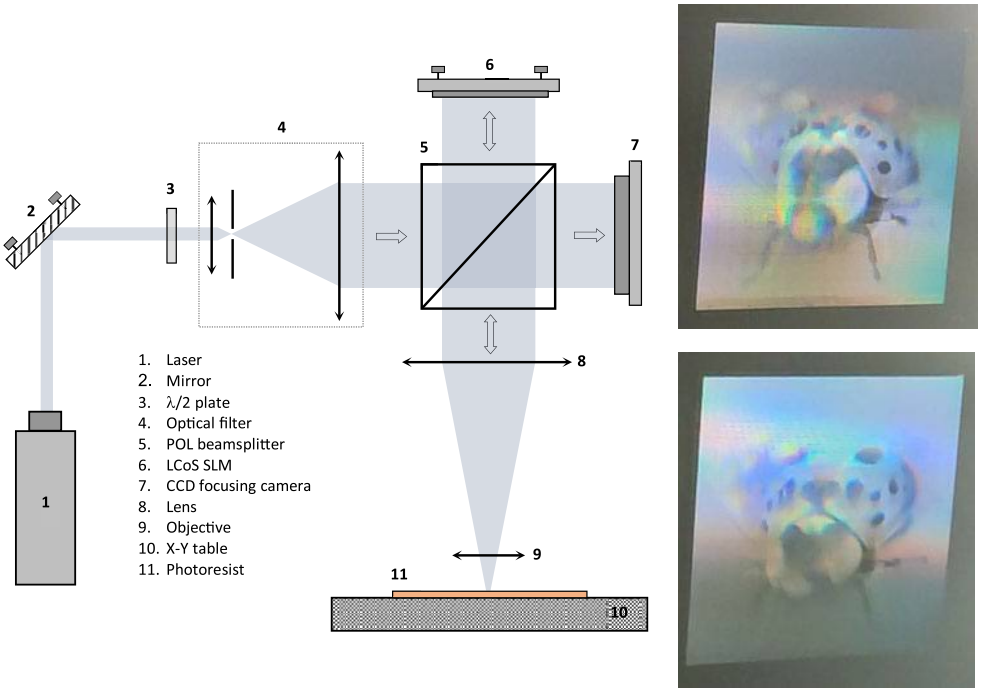

Fig. 12. (Left) A simplified scheme and photo of optical lithographic system used in recording the DWDH fringe patterns above by the IMP-6. (Right) Two views of final recorded hologram.

Fig. 13. For comparison this is a hologram of the data of Fig. 9, produced on a DIWO-6 machine.

4. CONCLUSIONS

We have presented two new features that are now available as standard in Geola's DWDH commercial security originator DIWO-6. These are:

- the inclusion of full-parallax achromatic optically-variable stereograms on a security photoresist master and
- the improvement of greyscale on all holograms created by the DIWO-6 machine using dithering of the SLM images by Burke's algorithm.

We have also presented initial work concerning the creation of true DWDH security hologram features using the image matrix IMP-6 machine employing only lithography. Here the DWDH fringe pattern of each hogel is calculated via computer rather than formed by interference. Initial results are promising; further work will be required to see whether the image quality can be increased to a satisfactory level.

REFERENCES

1. Yamagushi, M., Koyama, T., Endoh Ohyama, H., Takahashi, S., & Iwata, F. (1995). Development of Full-Parallax Holoprinter. *Practical Holography IX,* Proc. SPIE 2406, 50–56.
2. Bjelkhagen, H., & Brotherton-Ratcliffe, D. (2013). *Ultra-Realistic Imaging: Advanced Techniques in Analogue and Digital Colour Holography.* USA: CRC Press, ISBN:10 0367576430.
3. Klug, M., Holzbach, M., & Ferdman, A. (1998). *Method and Apparatus for Recording 1-step Full-Color Full-Parallax Holographic Stereograms.* US Patent No US6330088B1.
4. Brotherton-Ratcliffe, D., Vergnes, F. M., Rodin, A., & Grichine, M. (1999). *Method and Apparatus to Print Holograms.* Lithuanian Patent No LT4842; and "Holographic Printer" (1999); U.S. Patent No. US7800803B2.
5. Zacharovas, S., Nikolskij, A., Bakanas, R., & Brotherton-Ratcliffe, D. (2013). One-step 3D Full-Colour and Achromatic Transmission Holograms Digitally Printed Using a 440 nm Pulsed Laser for Embossed Applications. *Proc. SPIE 8644, Practical Holography XXVII: Materials and Applications*, 864407. doi: 10.1117/12.2008469
6. Bakanas, R. (2017). *Holographic Structures Formation in Light Sensitive Photopolymeric Materials Using Pulsed Laser and Digital Holography Method.* Summary of PhD Thesis. Kaunas: Kaunas University of Technology.
7. Zacharovas, S., Bakanas, R., Bulanovs, A., & Varadarajan, V. (2017). Effective Public Security Features for Embossed Holograms. *Proc. SPIE 10127, Practical Holography XXXI: Materials and Applications*, 1012702. doi:10.1117/12.2248904
8. Zacharovas, S., Adliene, D., Bakanas, R., Šeperys, R., & Narmontas, P. (2014). Master-Holograms Recorded with Pulsed Laser on Photoresist. *Proc. SPIE 9006, Practical Holography XXVIII: Materials and Applications*, 900605. doi: 10.1117/12.2044365
9. Bakanas, R., Jankauskaite, V., Bulanovs, A., Zacharovas, S., & Vilkauskas, A. (2017). Comparison of Diffraction Patterns Exposed by Pulsed and CW Lasers on Positive-Tone Photoresist. *Applied Optics, 56* (8), 2241–2249. doi 10.1364/AO.56.002241
10. Goncharsky, A. V., & Goncharsky, A. A. (2004). *Computer Optics and Computer Holography*. Moscow: Moscow University Press.

11. van Renesse, R. L. (2004). Security Aspects of Commercially Available Dot Matrix and Image Matrix Origination Systems. *SPIE International Conference on Optical Holography and its Applications*. Kiev, Ukraine.
12. Davis, F. S. (1988). *Holographic Image Conversion Method for Making a Controlled Holographic Grating.* US patent US5262879.
13. Rob Munday et al. (1997). *Method and Apparatus for Creating Holographic Patterns.* Patent WO 9829767.
14. Stepien, P., & Gaida, R. (1997). *Optically Variable Device (OVD) and a Method of Recording OVD and an OVD Recorder.* Patent WO1997016772.

sciendo

LATVIAN JOURNAL OF PHYSICS
AND TECHNICAL SCIENCES
2024, N 5

DOI: 10.2478/lpts-2024-0034

A METHOD TO ESTIMATE SOLAR PANEL ORIENTATION EFFECTIVITY

J. Kallunki[1*], T. Kauppinen[2]

[1] Metropolia University of Applied Sciences,
Myllypurontie 1, Helsinki, FI-00079, FINLAND
[2] Mutsal, Tunturikoivuntie 6, 90630 Oulu, FINLAND
*email: juha.kallunki@metropolia.fi

In the past years, new photovoltage (solar panel) systems have been installed rapidly, for instance, in regular households. Investment decisions have often been made without knowing all technical facts and information, which are affecting total energy production of photovoltage systems. In this work, we have made a simple model, which shows solar panels energy production with the different orientation angles of solar panel. Our results show that if panels are installed more than 30 degrees from the optimal orientation, the energy production drops drastically. This result applies to both azimuth and tilt angles. The developed model is very adaptive, and it can use any locations and all orientation angles. We confirm our calculation result by making a measurement with a small (30 W) test solar panel. The model and measurement results have a good relationship (correlation coefficient, $R^2 = 0.7$). The obtained result is satisfactory by taking into account the fact that measurements were made during the variable weather conditions and over long period of time (six months).

Keywords: *Energy production, photovoltage system, renewable energy, solar panel.*

1. INTRODUCTION

Renewable energy sources such as solar power have become very popular in the past years without reason. The usage of fossil fuels plays a major role in the climate change. Thus, it is important that renewable energy sources are put into use in a larger scale. Solar power is one alternative energy source for fossil fuels. Besides, the prices and installation costs of small-scale solar power systems have dropped drastically in the past few years. Solar panel (or photovoltage, PV) alignment is a major factor when studying carefully their energy production. Both tilt and azimuth angles have their own effect on the energy production. Regular households have been actively

installing small-scale photovoltage systems when the electricity price has been increasing at the same time. The development is positive. However, investment plans in regular households are made partly without knowing true facts. The PV system vendor might give too positive information about PV system payback times and PV energy production, for instance. Especially, the azimuth alignment is critical for the total, annual energy production. For instance, if the photovoltage system is installed on the top of the roof of a small residential building, which has an east-west alignment, the energy production is far from the optimal situation.

The tilt angle is the angle of the photovoltaic modules from the horizontal plane for a fixed mounting. In some contexts, the term "elevation angle" is also used, as each latitude has an own optimal tilt angle. Some general rules have been given when choosing the optimal tilt angle. The basic rule has been that the tilt angle should be equal to the latitude angle of the site. Usually, PV panels are directed to the south, which gives the optimal energy production. Optimal energy production could be achieved when panels are tracking the Sun over the whole day. However, this is not usually very economical. Besides, such a PV system is more complicated, and they need more regular maintenance.

In this work, we have created a simple mathematical model to estimate the annual solar panel system production. Besides, we have tested our model in practice. A single 30 W solar panel has worked as a test environment, and we have compared its output with the created model output. Thus, we have managed to validate our model. The test setup is in northern Europe (Finland). The model itself is generic, and it can be used in other location as well. Some estimations about optimal tilt angles in different locations have been done earlier, e.g., [1]–[5]. For instance, the research [4] uses National Solar Radiation Database. Therefore, this model is less mathematical, and it uses real solar radiation data. Purely mathematic models have also some disadvantages. Prevailing weather conditions, including the cloud coverage, are not included in the analysis. The information about the altitude above sea level could be useful information when defining accurate PV energy production. This also has a minor effect on energy production.

We are not taking a stand how much energy a regular house could produce, for instance, it depends on the size of the installation. However, our model gives relative information about energy production with different orientation angles. Our results could be used in all kind of installations from small-scale production to the large solar power plant.

Section 2 presents formulas and the theoretical background for the solar position estimation. In addition, the photovoltage energy production estimation principle is explained. The results and observations are presented in Section 3. Finally, the conclusions are made in Section 4, including further investigation topics and improvement ideas.

2. SOLAR POSITION

The first step when starting to estimate the energy production of the photovoltage system, it is important to define the solar position in the location under investigation. The hour angle (*HA*) is the first parameter when calculating solar elevation and azimuth angles. Twelve noon in a local solar time (*LST*) is a time when the Sun is the highest in the sky. Local time (*LT*) usually varies from *LST* because of the eccen-

tricity of the Earth's orbit, and because of human adjustments such as time zones and daylight saving. In this calculation, we did not include an effect of the eccentricity of the Earth's orbit. The total effect is small. A local solar time can be calculated as follows:

$$LST = LT + \frac{TC}{60}, \tag{1}$$

where LT is local time in hours and TC is a time correction factor. A time correction factor can be calculated as follows:

$$TC = 4 \times (lon - 15° \times \Delta T_{UTC}), \tag{2}$$

where *lon* is a longitude coordinate of specific location and ΔT_{UTC} is the difference of the Local Time (LT) from Universal Coordinated Time (UTC) in hours. After the local solar time has been defined, the hour angle can be calculated as follows:

$$HRA = 15° \times (LST - 12). \tag{3}$$

Before the solar position (azimuth and elevation) can be defined, the declination angle must be defined. The declination angle varies seasonally due to the tilt of the Earth on its axis of rotation and the rotation of the Earth around the Sun. There are a few formulas which can be used for the calculation of declination angle (δ). In this study, we used the following formula:

$$\delta = 23.45 \times \sin\left(\frac{360}{365} \times (d - 81)\right), \tag{4}$$

where d is a day number of the year. The difference between different formulas is relatively small (< 0.3°). To have more accurate estimation, we took into account the fact that d is changing over the day. Finally, elevation (α) and azimuth (β) angles of the Sun can be calculated. The elevation and azimuth angles are defined as follows:

$$\sin\alpha = \sin\delta \sin\varphi + \cos\delta \cos\varphi \cos(HRA); \tag{5}$$

$$\cos\beta = \frac{\sin\delta \cos\varphi - \cos\delta \sin\varphi \cos(HRA)}{\cos\alpha}. \tag{6}$$

2.1. Solar Radiation

After Sun's position has been defined, we can calculate the solar radiation at every point in time. The solar radiation (F) on arbitrary orientated and tilted surface can be calculated as follows:

$$F = \cos\alpha \sin\alpha_{tilt} \cos(\beta_{orien} - \beta) + \sin\alpha \cos\alpha_{tilt}, \tag{7}$$

where α_{tilt} is the photovoltage panel tilt angle and β_{orien} is the azimuth angle where the panel is pointed to.

We have estimated annual energy production so that we have calculated solar radiation in every 15 minutes in panel azimuth angles from 90° to 270° (with 2- or 5-degree steps) and panel tilt angles from 0° to 90° (with 2-degree steps). In each 15-minute step, hour, declination, and solar azimuth and elevation angles have been calculated separately. Finally, a daily average energy production with various angles (both azimuth and tilt) has been calculated for each azimuth and tilt angles on the basis of a 15-minute step. With this method, we have found optimal orientation angles from

the energy production point of view. We have used this value (factor, *F*), presented here, in comparison with real solar panel energy production. The factor *F* varies between 0 and 1. The value 1 (one) means that the solar panel energy production is optimal (maximum) in the location under investigation. It is important to remember that simulation takes only into account direct solar radiation, which is facing to the panel. The isotropic radiation cannot be included in the simulation; thus, it depends on local conditions, such as shading and atmospheric stability.

3. RESULT

We have created a coloured contour map, which shows the photovoltage system energy production (colour scale) with different panel's tilt (y-axis) and azimuth orientation (x-axis) angles. In the current location (southern Finland), panel should be directed to the south (± 10°). In our study, the most energy effective angle is 186° ± 1°. The south is in the direction of 180. This can also be noticed in Fig. 1. The best tilt angle (elevation) should be 44° ± 1° (optimal position). Previous studies gave somewhat smaller optimal tilt angle: 39° [1, 4]. The value 1 (one) for a factor *F* achieved in angles 186° ± 1° (azimuth) and 44° ± 1° (tilt). With these orientation angles, solar panel annual energy production is the most effective. However, the energy production does not drop drastically (less than 10 %) if the tilt angle is changing only ± 20°. The energy production drops around 38 % if panels are oriented to the west. This is a major difference and reduction to the energy production. We can conclude that panels should be oriented to the south with an accuracy ± 40°, if it is required that the energy production is still 90 % of the maximum. The result shows that energy production is still rather good even if orientation angles (azimuth and tilt) are some tens of degrees away from the optimal position. In the tilt angle, the allowed change is smaller. With a bigger change, the energy production drops drastically. In Fig. 2, the photovoltage system energy production close to the optimal orientation is shown. Figure 2 shows that the energy production is very effective when angle differences are ± 30° from the optimal angles. The result emphasises the matter that solar panels do not have to be orientated exactly to the south. Some difference is allowed, but not too large (> 60°).

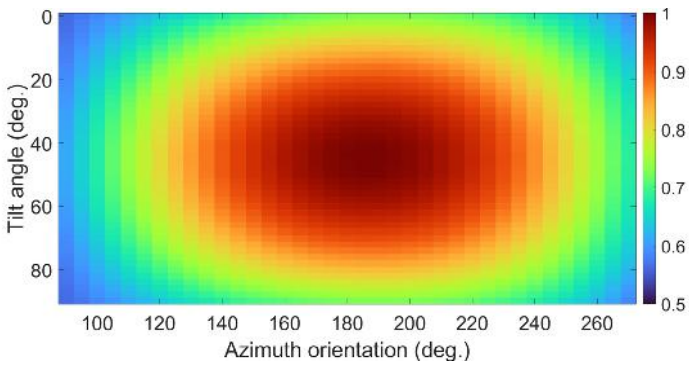

Fig. 1. Photovoltage (PV) system energy production with different tilt (0–90) and azimuth orientation angles (90–270). The south is in the direction of 180. Red colour (values close to 1) indicates that the energy production is optimal or close to optimal. A blue colour indicates efficiencies below 60 %.

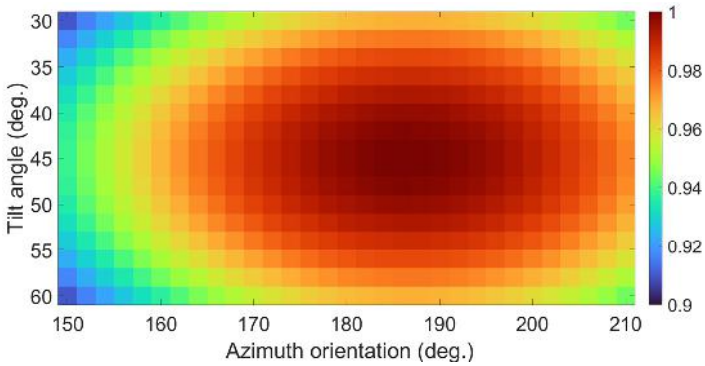

Fig. 2. Photovoltage (PV) system energy production with different tilt (30–60) and azimuth orientation angles (150–210). The south is in the direction of 180. Red colour (values close to 1) indicates that the energy production is optimal or close to optimal. The plot is made closer to optimal position. A blue colour indicates efficiencies below 94 %.

We have tested our model with a real solar panel. The panel nominal power is 30 W, so it is rather small. In Fig. 3, a test solar panel installation is shown. The solar panel is oriented close to the south 183° (±1°) with a tilt angle of 90° (±2°). We have measured the solar panel's open-circuit voltages during the fall, winter and spring seasons (from October 2023 to March 2024). Measured values have been recorded on days, when cloudiness level is moderate. This selection has been made using visual inspection. Besides, the ambient temperature has varied between -20 °C and +10 °C over the period of measurements. Since the temperatures have been rather moderate, we can assume that the efficiency of the panel is stable. The solar panel has the temperature correlation; high panel temperature means lower efficiency [6]. Totally 262 individual measurements have been collected. It has been shown that the open-circuit voltage increases with increasing irradiation with a linear dependency [7].

Fig. 3. The solar panel (30 W) under test, which has been used to confirm our calculation model. The panel is oriented close to the south 183° (± 1°) with a tilt angle of 90° (± 2°). On the right side of the panel there is a voltage meter (marked with a red circle), which shows the solar panel open-circuit voltage in real time. The picture has been taken on a cloudy winter day, and on that time energy production has been negligibly small and the voltage output has been zero.

Figure 4 shows the relationship between calculated panel efficiency and measurement. We have made a linear fit (a first-degree polynomial function) to obtain the measurement results. The correlation coefficient (R^2) between measurements and a fit model is 0.7. We have added an extra term to solar radiation (F) factor to present indirect radiation. It has been shown that the indirect radiation has a strong dependency with a solar elevation [8]. We chose a simple term for the indirect radiation: $a \times \sin \alpha$. Thus, the corrected solar radiation factor (F_{corr}) can be defined as follows:

$$F_{corr} = F + a \times \sin \alpha \,, \tag{8}$$

where a is an individual factor (a = 1.02), which only matches to this specific location and measurements.

This value is rather good by taking into account variable weather conditions over the long measurement period. The weather conditions are very critical for the energy production. This can be seen especially clear on times of low solar elevations, from the fall to the spring season. In addition, the solar panel under investigation is located in urban environment with some obstacles in front of it. This means that in some solar angles, there might be some losses or reflections, which affect debilitating to the open-circuit voltage. However, we can conclude that the measurement result also confirms that our calculation model is usable.

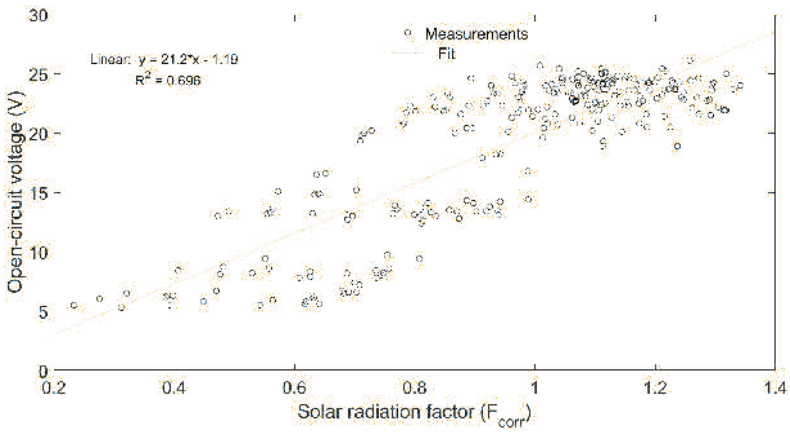

Fig. 4. The relationship between solar panel's open-circuit voltage and solar radiation factor (F_{corr}). The blue dots indicate individual measurements. The yellow line is a fit line (linear fit, a first-degree polynomial function), which is done on the basis of measurements. The correlation coefficient (R^2) between measurements and a fit model is 0.7.

4. CONCLUSIONS

We can conclude that the generated model works rather reliably and accurately. However, we could not test our model comprehensively since we could only use a single solar panel for verifying our results. The measurement should also be verified using other solar panels, which are installed with different orientation angles, and in other locations. In addition, the measurement should be repeated using different size solar panels, and also different manufacturer panels. The devolved model is simple and it can

be used in any geographical locations. We did our measurement in the season from fall to spring; thus, the ambient temperature was moderate, and we could assume that the efficiency of the solar panel was stable. If the measurements are repeated in the summer season during hot summer days, the effect of the ambient temperature must be included in the analysis. In addition, we can conclude that local conditions (e.g., shading, panel temperature and atmosphere stability) have a major effect on the final energy production. The estimation of indirect radiation is challenging and the local conditions also contribute to this.

Results showed that energy production of solar panel decreased significantly if the tilt angle was more than 20 degrees from the optimal orientation, and in the azimuth direction, the angle could not be more than 40 degrees from the optimal orientation. This means that if the panels are installed in the east-west alignment, the energy production is far from the optimal. In this case, the energy production drops by 38 %, which is a major decrease for the production. If the solar panel, for instance, is installed on the east-west alignment, the investment decision should be made using careful consideration.

Our calculation and measurement also show that in the winter season, it is also possible to get some energy production from the solar panels if the panel orientation is made correctly. In Finland (north Europe), this means that tilt angle must be really high (between 70 and 80, and, on the opposite, in the summer season angle must be closer to 40. This means that there must be a possibility to adjust the tilt angle in different seasons. It can be technically rather challenging, at least in regular household installations. This is also increasing system total costs, and further the payback time. Usually, solar panel system's tilt angle is some sort of trade-off, which means that energy production is not very effective in the winter season. A common approach or aim is that the annual energy production will be maximised with a static azimuth and tilt angles. In addition, we have shown that the estimation of indirect radiation is rather challenging.

Calculations were made with a 15-minute step, so the efficiency factor, F, was calculated every 15 minutes. The time interval could be dense, but it required more calculation capacity. The calculation algorithm was made with Matlab. With a current simulation setup (15-minute step) and a standard laptop, it takes more than 12 hours to complete the whole simulation.

REFERENCES

1. Barbón, A., Bayón-Cueli, C., Bayón, L., & Rodríguez-Suanzes, C. (2022). Analysis of the Tilt and Azimuth Angles of Photovoltaic Systems in Non-ideal Positions for Urban Applications. *Applied Energy, 305,* 117802. https://doi.org/10.1016/j.apenergy.2021.117802
2. Han, Z., Zhou, W., Sha, A., Hu, L., & Wei, R. (2023). Assessing the Photovoltaic Power Generation Potential of Highway Slopes. *Sustainability, 15* (16), 12159. https://doi.org/10.3390/su151612159
3. Božiková, M., Bilčík, M., Madola, V., Szabóová, T., Kubík, Ľ., Lendelová, J., & Cviklovič, V. (2021). The Effect of Azimuth and Tilt Angle Changes on the Energy Balance of Photovoltaic System Installed in the Southern Slovakia Region. *Applied Sciences, 11* (19), 8998. https://doi.org/10.3390/app11198998

4. Jacobson, M. Z., & Jadhav, V. (2018). World Estimates of PV Optimal Tilt Angles and Ratios of Sunlight Incident upon Tilted and Tracked PV Panels Relative to Horizontal Panels. *Solar Energy, 169*, 55–66. https://doi.org/10.1016/j.solener.2018.04.030
5. Prunier, Y., Chuet, D., Nicolay, S., Hamon, G., & Darnon, M. (2023). Optimization of Photovoltaic Panel Tilt Angle for Short Periods of Time or Multiple Reorientations. *Energy Conversion and Management: X, 20*, 100417. https://doi.org/10.1016/j.ecmx.2023.100417
6. Maghami, M. R., Hizam, H., Gomes, C., Radzi, M. A., Rezadad, M. I., & Hajighorbani, S. (2016). Power Loss due to Soiling on Solar Panel: A Review. *Renewable and Sustainable Energy Reviews, 59*, 1307–1316. https://doi.org/10.1016/j.rser.2016.01.044
7. Chegaar, M., Hamzaoui, A., Namoda, A., Petit, P., Aillerie, M., & Herguth, A. (2013). Effect of Illumination Intensity on Solar Cells Parameters. *Energy Procedia, 36*, 722–729. https://doi.org/10.1016/j.egypro.2013.07.084
8. Sansa, I., & Mrabet Bellaaj, N. (2022). Forecasting and Modelling of Solar Radiation for Photovoltaic (PV) Systems [Internet]. *Solar Radiation - Measurement, Modeling and Forecasting Techniques for Photovoltaic Solar Energy Applications. IntechOpen*. http://dx.doi.org/10.5772/intechopen.99499

sciendo

LATVIAN JOURNAL OF PHYSICS
AND TECHNICAL SCIENCES
2024, N 5

DOI: 10.2478/lpts-2024-0035

COMPARATIVE STUDY OF WASTE MANAGEMENT AND SAMPLING PRACTICES IN LATVIA AND ESTONIA

L. Zemite[1,2]*, A. Backurs[1,3], K. Vonda[4], S. Batjuskovs[5],
P. Cnubbern[6], L. Jansons[1,7]

[1]Latvian Hydrogen Association,
1 Akademijas Square, Riga, LV-1050, LATVIA
[2]Riga Technical University,
Faculty of Computer Science, Information Technology and Energy,
12-1 Azenes Str., Riga, LV-1048, LATVIA
[3]Latvia University of Life Sciences and Technologies,
Faculty of Engineering,
5 J. Cakstes Blvd., Jelgava, LV-3001, LATVIA
[4]Ltd. Getliņi EKO,
57 Kaudzisu Str., Rumbula, Ropaži parish, LV-2121, LATVIA
[5] Ernst & Young Baltic,
1A Muitas Str., Riga, LV-1010, LATVIA
[6]Hydrogen Architects,
9728 RJ Groningen, THE NETHERLANDS
[7]Riga Technical University,
Faculty of Engineering Economics and Management,
6 Kalnciema Str. 210, Riga, LV-1048, LATVIA
*e-mail: prof.zemite@gmail.com

The study focuses on waste management and sampling practices carried out in two large Baltic cities: Riga (Latvia) and Tartu (Estonia). Even though waste collection schemes are not at the same centralisation level in the two municipalities, certain similarities can be observed in waste collection, management and sampling processes. Governed by provisions of Council Directive 1999/31/EC of 26 April 1999 on the landfill of waste, general national waste treatment legislation, and the national waste management plans, waste management practices in Latvia and Estonia are moving towards minimalisation of waste landfilling and maximalisation of waste inclusion into various recycling practices (use in waste biodegradation cells, bioreactors, different waste recycling facilities, in developing modern waste management supporting infrastructure, etc.). Therefore, waste management in two countries can be partly

characterised as a vital element of emerging circular economy activities aimed at minimising landfill deposition of waste, hence, a more effective and permanent approach to sustainable waste management problems, on the one hand, and maximising the diversified use of waste in different branches of economy, hence, larger economic and social benefits.

Keywords: *Getlini, Tartu, waste management, waste processing, waste sampling.*

1. INTRODUCTION

The management of waste is a growing concern globally, regionally and nationally. In 2020, the total waste generated in the EU amounted to 2 135 million tons or 4 815 kg per capita. Only 39.2 % of waste was recycled and 32.2 % landfilled [1].

However, the traditional method of disposing of waste in landfills is no longer deemed sustainable due to the impact it has on the environment. Waste management facilities need to move towards a more sustainable and circular approach to reduce the amount of waste that is landfilled and to minimise the environmental impact of waste management [2], [3]. There is a need for innovative solutions that utilise new technologies and business models to create a more sustainable waste management system [4], [5].

This goes in line with the target set by Council Directive 1999/31/EC of 26 April 1999 on the landfill of waste (Directive 1999/31/EC) to take the necessary measures to ensure that by 2035 the amount of municipal waste landfilled is reduced to 10 % or less of the total amount of municipal waste generated (by weight) [6].

In line with provisions of Directive 1999/31/EC, Latvia adopted the National Waste Management Plan for 2021–2028 [7], so the effectiveness of waste prevention measures can be evaluated based on the following quantitative indicators, which by substance are comparable to aims for 2028 (see Table 1).

Table 1. Quantitative Indicators for Evaluation of Effectiveness of Waste Prevention Program in Latvia

No.	Quantitative indicators	Measurement	2018	2028
1	Total volume of household waste produced by households	kg per capita	409	<400
2	Total volume of household waste	t/year	785 074	<600 000
3	Total volume of produced hazardous waste	t/year	118 142	<50 000
4	Total volume of recycled household waste	% of total volume	43	55
5	Total volume of recycled hazardous waste	% of total volume	31	75
6	Total volume of recycled production waste	% of total volume	83.3	85
7	Total volume of household waste that is landfilled	% of total volume	58.9	< 40
8	Total volume of production waste that is landfilled	% of total volume	5	< 25 %
9	Total volume of hazardous waste that is landfilled	% of total volume	4.5	< 25 %

Source: [7]

The plan focuses on the increase of recycling level of each waste type, especially household and hazardous waste. However, at the European Union level, the Latvians still sort too little. For example, in 2021, Latvia had to pay EUR 15 million in sanctions for its small amount of recycled plastic. This would account for a similar amount in 2022. Every resident of Latvia will pay approximately EUR 8 per year for this. State audit warns that Latvia could also be faced with an additional EUR 11 million penalty for the insufficient collection of biodegradable waste (BDW) [8].

Also, in Estonia goals are determined in line with Directive 1999/31/EC, but the Estonian National Waste Plan for 2023–2028 emphasises increasing safe material recycling and promotion of waste prevention and reuse (see Table 2). By 2028, Estonia aims to increase household waste recycling rate by 29 %.

Table 2. Quantitative Indicators for Evaluation of Effectiveness of Waste Prevention Program in Estonia

No.	Quantitative indicators	Measurement	2020	2028
1	Waste generation per person	kg per capita	4 151	4 000
2	Rate of circulating material	% of total volume	17	25
3	Share of reusable packaging from packaging placed in market	% of total volume	0	10
4	Household waste recycling	% of total volume	29	58
5	Packaging waste recycling	% of total volume	66	70
6	Recycling of construction and demolition waste	% of total volume	32	40
7	Recycling of hazardous waste	% of total volume	48	55
8	Electrical and electronic waste collection rate	% of total volume	62	65
9	Battery and battery waste collection rate	% of total volume	39	63

Source: [9]

Estonia has an obligation to recycle at least 55 % of household waste (recycling means waste is used as material, incineration does not qualify for recycling). The goal must be achieved by 2025. Currently, approximately 30 % of household waste is recycled [10].

Current research reviews the types of waste processed in waste treatment facility serving Riga and its vicinity, Latvia, and several waste treating facilities serving Tartu, Estonia, and establishes a methodology for waste sampling and testing that can help identify types and amounts of waste that can be recycled or processed in addition to already established recycling processes.

2. AN OVERVIEW OF WASTE MANAGEMENT PROCESSES

2.1. Getlini, Latvia

Getlini is a company formed jointly by the municipalities of Riga and Ropazi municipality, which manages the largest solid household waste landfill in the Baltic States. The main objective of the company is to ensure modern, safe and efficient management and disposal of solid household waste as well as production of electricity.

The goal is to ensure continuous improvement of the quality of the services provided and reduction of the environmental impact [11].

The landfill is one of the most modern in Europe, currently developed as a secure waste recycling centre. With the total area of 89.8369 ha, Getlini is formed by the old, reclaimed waste dump site, waste disposal cells, bioreactor, waste recycling infrastructure, as well as infrastructure supporting waste management – facilities, administration buildings, etc. It accepts waste from natural and legal persons, and currently has 1360 contracts in force with legal entities for the acceptance and disposal of household, industrial and construction waste. Waste from natural person is accepted without contract with immediate settlement after delivering the waste to the landfill.

According to information shared by Getlini, total amount of waste received in 2021–2023 is gradually decreasing, i.e., by 24 % comparing 2023 to 2021. The main change is acknowledged in construction waste (-56 % comparing 2023 to 2021). Getlini reviewed tariff for reception of construction waste in 2022 that led to an increase of fees. As a result, the amount of received construction waste dropped due to availability of lower tariffs in the market.

The average composition of total waste is illustrated in Fig. 1. A major part of waste received by Getlini is formed by unsorted household waste (on average 5 9% of total waste amount). The second position takes construction waste (17 %) and waste from the waste management industry (15 %).

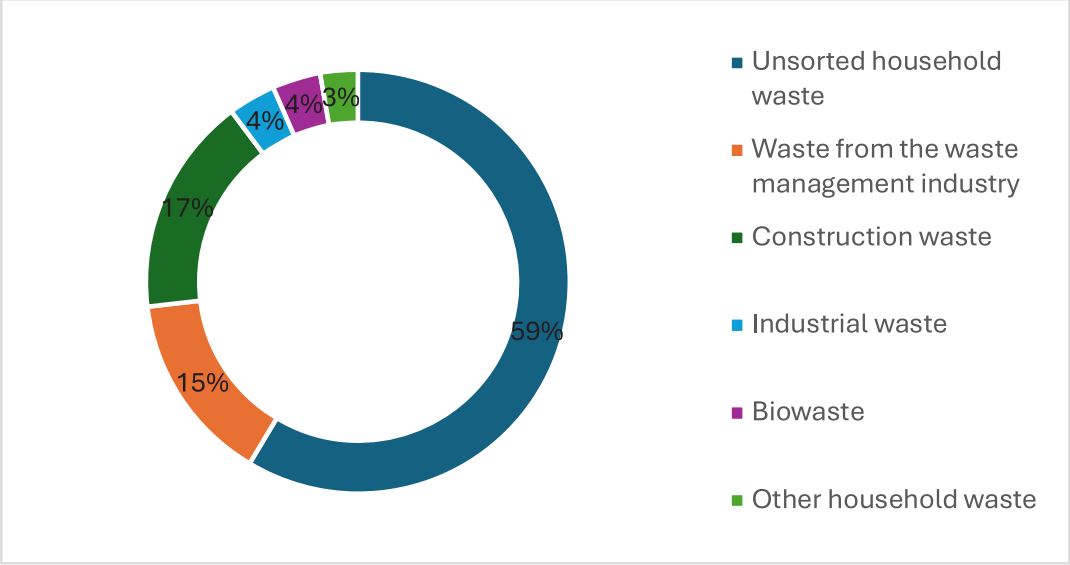

Fig. 1. Average composition of waste received by Getlini in 2021–2023.

Source: [12]

According to information on total produced waste in Latvia in 2021 (see Table 3), Getlini managed 22 % of total produced waste in Latvia. However, Getlini received more than half (55 %) of unsorted household waste and 73 % of biowaste generated in Latvia in 2021.

Table 3. Waste Received by Getlini of Total Produced in Latvia in 2021, t

Waste category	Received by Getlini [17]	Total produced in Latvia [21]	Received by Getlini of total produced in Latvia
Unsorted household waste	268 844	493 046	55 %
Waste from the waste management industry	59 542	443 040	13 %
Construction waste	112 224	394 573	28 %
Industrial waste	21 416	517 473	4 %
Biowaste	27 740	37 803	73 %
Other household waste	23 994	483 313	5 %
Total	513 761	2 369 248	22 %

Source: [13]

Getlini manages four main waste streams: household waste, BDW, industrial waste and construction and demolition waste, although it does not have its own waste sorting station. Waste sorting is ensured by the sorting station located in the landfill site, which was built in 2015 and is managed by "Vides resursu centrs" Ltd. that was selected within a public procurement procedure as a service provider. Getlini does not accept any kind of hazardous waste.

2.1.1. Unsorted Household Waste Sorting Plant and BDW Recycling Complex

In the landfill of Getlini, an unsorted household waste sorting plant was opened in 2015. It is currently managed by Vides resursu centrs Ltd. In the plant, BDW, PET bottles, tin cans, waste containing ferrous and non-ferrous metals, light plastic, textiles, and paper (to produce fuel derived from waste) are mechanically separated and directed to recycling (secondary raw materials). The capacity of the unsorted household waste sorting plant is 300,000 t/year.

The nominal hourly capacity of the sorting plant is 80 tons, which means that a maximum of 960 tons of waste can be sorted per day, on average around 822 tons of waste. The road transport with loads of waste is registered and weighed in Getlini pass house. The quantity of waste accepted is determined by weight – on arrival the total weight of the waste is weighed with the load and on departure the weight of the empty transport is weighed.

Vides resursu centrs Ltd. in its selected technological equipment can separate the following types of waste (by volume):

1. BDW or separated biomass (biomix): 230,000 t/year. This waste is delivered to the landfill site (105,000 t/year for disposal and 125,000 t/year at the BDW recycling facility);
2. non-recyclable or inert waste (residuals) – 40,000 t/year. The waste is transferred to Getlini for landfilling;
3. secondary raw materials suitable for further recycling (~10 % of incoming waste flow) [14].

In BDW recycling complex treats the following waste streams: BDW from gardens and parks, BDW from households, restaurants, catering establishments, retail premises and other similar food cooking merchants where BDW is generated, BDW from mechanical waste processing suitable

for composting or anaerobic digestion and plant tissue waste from Getlini greenhouses.

The BDW treatment process is divided into two phases: anaerobic and aerobic fermentation, with the aim to process the biodegradable part of the waste in controlled conditions and generate biogas, which is collected and used for energy production.

Approximately 450 t of BDW are placed in the tunnels and are sealed from the surrounding environment with hermetic doors, ensuring an anaerobic environment. In this stage, BDW is sprayed with an infiltrate solution (percolate), which contains a large amount of organic and inorganic substances that catalyse waste decomposition in the hydrolysis process. The percolate is circulated between the tunnels and methanogenic reactors. A percolate collection/aeration system is installed in the tunnel floors from which all the liquid is diverted to the pump station to be pumped into buffer tanks. After the buffer tank, the percolate is filtered and fed into one of the two 4,200 m^3 methane reactors, where bacteria convert lighter hydrocarbons into methane. Hydrolysis lasts for four weeks; the time is constant and entered in the automation system. Generated biogas is used as fuel to produce heat and electricity at the Getlini power plant. The produced heat and electricity are used in Getlini technological processes, thus promoting the rational and circular use of resources [15].

After hydrolysis, fresh air supply begins for the whole material in one tunnel for a 4-week aeration process, which ensures complete biological processing to stabilise it. Fresh air is delivered through the percolate collection/aeration system installed in the tunnel floor and is pumped from the tunnel through a ventilation pipe installed in the top part of the tunnel. This is achieved with air pumps that create low vacuum in the tunnel. The air pumped from the tunnels is passed through biofilters to reduce emissions and odours that leak into the surrounding environment. During the aeration process, the temperature in the tunnels, according to a natural biological process, is in the range of 45–65 ^{0}C. Consequently, the biomass is made stable in this way. At the end of the composting process, the moisture in the biomass is reduced by 50 %, and the volume decreases by 20 %–30 %.

During the entire processing process, system operators monitor and control technical parameters – tunnel temperature, methane quantity and concentration, percolate flows, etc., using a monitoring, control and data acquisition management system [16].

After the composting process, the stabilised material in the closed tunnel is unloaded with mobile equipment and loaded into a sorting (screening) line hopper. The first separation stage is a drum sieve (drum sieve No 1) with two fractions 0–75 mm and 75–200 mm. The finer fraction is screened by a drum sieve No 2, resulting in 0–30 mm (technical compost) and 30–75 mm fractions. The initial 75–200 mm fraction is sent to a wind sieve, where the finer fraction falls out as potential RDF, while the heavier fraction, along with the 30–75 fraction obtained from drum sieve No 2, is further screened with a star sieve, from which 0–60 (mulch) and 60–200 (landfilled) mm fractions are obtained.

Mulch is used daily as a covering material in the quantity specified in the category A pollution permit while the rest is landfilled. The production capacity is 40,000 t/year. The potential refuse-derived fuel (RDF) material is collected in the screening area and, without storage, is landfilled in the disposal cell. The production capacity is 12,500 t/year. The fraction to be landfilled is collected in the screening area and is buried in the disposal cell without storage [14].

2.1.2. Bioreactor

In the first quarter of 2016, the operation of a bioreactor started in the territory of landfill where BDW is placed with the aim of obtaining biogas. When waste is placed in a bioreactor, leachate recirculation and gas collection systems are also installed in layers, and biogas is obtained. After filling the bioreactor with BDW, it is covered with a temporary reclamation layer. The operation time of the bioreactor is 15 years. At the end of the operation period, the material is sieved, and the following fractions are obtained: technical compost, part to be landfilled (inert materials, potentially they would be admixtures of biological waste that the factory could not separate – of glass or rock origin, small metal, textile, etc.) and energy resource.

Within a year, according to category A pollution permit, it was allowed to place: 230,000 tons of BDW obtained from Vides resursu centrs Ltd., up to 50,000 tons of BDW received from waste management companies, residents, and other merchants, up to 45,000 tons of BDW from construction and demolition and bulky waste sorting line and up to 1000 tons of green mass (leaves and stems) generated in greenhouses at the landfill site [14].

Figure 2 shows the amount of biogas produced by Getlini in 2022 and its methane content. On average, Getlini produces 190,000 m^3 of biogas per month with methane content exceeding 50 %. The volume of produced biogas is gradually decreasing (-26 % comparing December 2023 to January 2023).

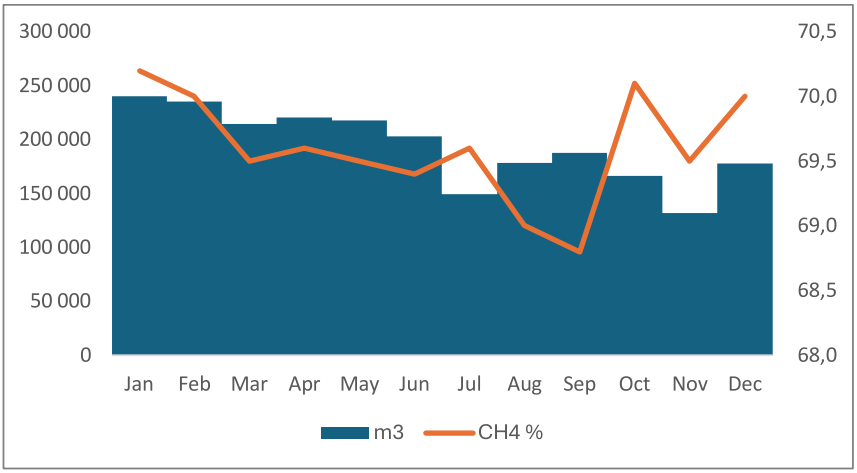

Fig. 2. Biogas produced by Getlini in 2023 and its methane content.

Source: [12]

Landfill gas, mainly consisting of methane (50–55% by volume) and carbon dioxide (45–50% by volume), is formed during the waste decomposition process [17]. Releasing methane into the atmosphere is environmentally unfavourable because it creates a greenhouse effect, contributing to global climate change. To reduce the release of greenhouse gases (GHG), Getlini collects and burns the gas from the waste in the cogeneration plant, producing thermal energy and electricity. Electricity is sold on the free market while thermal energy is used in the greenhouses of Getlini [14].

However, in future the possibility of biomethane production and injection into the gas distribution network can be reviewed [18]–[22].

2.1.3. Landfill Cell

Waste landfilling cells are located adjacent to the old, remediated waste dump site, and they are equipped with an appropriate base – peat was excavated throughout the area, the base was filled with gravel or sand, covered with a geotextile and a layer of clay as well as a water-impermeable film lining protected by a geomembrane. Above this isolating layer a drainage system for infiltrate collection was installed.

In the landfill, a 50-ton compactor operates, which compacts the delivered waste. When placing waste and after its compaction, a regular covering is applied using a hardening substance. The regular covering is performed by the service provider who delivers the material intended for the covering to the site. This covering also uses mulch from BDW processing.

When placing waste in disposal cells, gas collection pipes (perforated, flexible pipes) are installed in it every approximately 6 meters upon reaching the thickness of the waste layer.

The following waste types are placed in the cell:

1. waste separated in the unsorted household waste sorting plant and not suitable for further recycling (sorting residuals);
2. mechanically sorted biowaste that cannot be recycled at BDW recycling complex due to its capacity;
3. unsorted household waste in emergency situations as well as during periods when maintenance work is carried out in the unsorted household waste sorting plant;
4. waste brought to the landfill site and not suitable for further treatment/recycling (industrial and household waste that meets the permitted types of waste for disposal at the household waste landfill according to the Cabinet Regulations No 1032 “Regulations Regarding Landfill Sites” [23]);
5. waste generated during waste recycling processes at Getlini, for example, waste separated at the construction and demolition sorting line, waste generated during sieving process at BDW recycling complex and not suitable for further recycling [14].

2.1.4. Sorting and Recycling of Construction Waste without Significant Impurities

Separate waste streams are accepted for crushing (recycling) construction waste which already have a low level of impurities in their composition. These are mainly demolition materials (concrete, asphalt and bricks). This material is crushed to form multiple fractions, while separated metal is stacked separately for later sale. Waste with a low mixture of plastics, rubber, and other types of waste ends up on the crushing line.

Wood-origin waste is collected and stacked in a separate pile which is shredded twice a year and currently sold to other waste management companies [14].

2.2. Tartu Municipality, Estonia

According to the Environmental Register, there are a total of 45 working waste treatment facilities in the city of Tartu. The most important waste treatment sites are the Aardlapalu transfer station, the biogas plant of the Tartu wastewater treatment plant, the

Ilmatsalu biogas and cogeneration plant, the South Estonian Hazardous Waste Management Centre, and the health care waste management site of Tartu University Clinic [10].

2.2.1. Collection and Transportation of Waste

One of the most important tasks of the municipality is to organise the collection and transport of household waste. The city is holding a public tender to find a waste hauler. Only the waste handler who has won the competition organised by the city may transport household waste in the area. Residents sign a contract with this company and pay the company directly. The municipality does not have garbage trucks, all work is done by the private sector based on public procurement.

The organised waste transport includes the following types of waste:

1. mixed household waste, which is taken to the Aardlapalu transfer station;
2. wastepaper, which is handed over to a company with a corresponding environmental permit;
3. biowaste, which is taken to Aardalpalu transfer station and composted there.

Residents and companies must hand over mixed household waste, biowaste and wastepaper to the company that won the organised waste transport tender. Four areas of Tartu municipality currently have one waste carrier – Eesti Keskonnateenused AS, who won tenders in all consequent areas.

In addition to organised waste transportation, the city of Tartu also organises waste collection by their type. At least the following types of waste must be collected separately in Tartu: paper and cardboard, packages, hazardous waste, biowaste, hazardous waste (refrigerators, TVs, computers, tires, etc.), bulky waste (furniture), metals, and textiles.

There are four ways to collect waste by type:

1. in a separate container next to the house for the collection of the corresponding type of waste (wastepaper and biowaste are collected this way). A separate container for wastepaper must be in apartment buildings with at least 5 apartments. The city also has public containers for private homes. There must be a separate container for biowaste in all properties;
2. in collection points on the territory of the city for the collection of different types of waste (packages, textiles, hazardous waste and wastepaper are collected in this way). The city has a public collection network for collecting packaging and textiles. About 100 containers have been installed in the city for packaging, 15 containers for textiles;
3. waste collected separately can be taken to a waste station;
4. waste is accepted by waste handlers (e.g., metal, construction waste).

Packaging manufacturers organise packaging collection. Producers are obliged to place collection points in the city in such a way that there is one collection point within a radius of approximately 500 meters from each household.

Collection points have been set up in the city for the collection of hazardous waste, expired/unused medicine can be handed over at pharmacies. Basically, hazardous waste is taken to waste plants.

Residents can hand over all types of waste at waste stations. There are two waste stations in Tartu that accept:

1. hazardous waste (batteries, paint and medicine waste, daylight lamps, etc.);

2. bulky waste (including old furniture);
3. electronic waste (refrigerators, TVs, etc.);
4. recyclable waste (wastepaper and metal, plastic and glass containers);
5. packaging waste;
6. wood, construction waste and similar.

Recycling centres operate in Tartu, where residents can discard furniture, dishes, books, clothes, toys etc. Items are organised in centres and sold for a small amount of money. Recycling centres are managed by non-profit organisations, and the city supports the activities financially.

According to Tartu waste management regulations, the following must be collected separately on the construction site: hazardous waste by type (it is not allowed to pour liquid hazardous waste such as paints, varnishes, solvents, glues, etc. into the hazardous construction waste collection container), wood, packaging, metals, permanent waste (stones, plaster, concrete, plaster, etc.), plastics and other mixed waste [24].

2.2.2. Aardlapalu Transfer Station

The mixed household waste collected from the city of Tartu is taken to the Aardlapalu transfer station. From there mixed household waste is directed to the following treatment sites: Iru mass incineration plant, Tallinn Waste Recycling Centre, the mechanical-biological processing plant located on Suur-Sõjamägi in Tallinn, the Uikala landfill (to produce waste fuel) and the Paikre, Torma and Väätsa landfills. To which waste treatment facility, the waste is currently sent depends on the operator of the Aardlapalu transfer station. However, based on the agreement between the city of Tartu and the operator, the principles of the waste hierarchy must be observed when choosing the final disposal site, and the largest possible share of mixed household waste must be directed to recycling (waste incineration, waste fuel production). Transferring waste to a landfill is permitted only as an exception. As part of the waste transport procurement, the city of Tartu has so far considered mechanical-biological processing as equivalent to mass incineration of mixed household waste.

At the end of 2013, a composting station was built in Aardlapalu where it is possible to compost food waste in an environmentally safe way, a waste sorting building and a reloading station with a garbage compactor [10].

2.2.3. Sorting Station

There is a sorting station operated by Ragn Sells AS in the city of Tartu where waste is accepted only from business customers according to the price list. Ragn Sells AS accepts construction and demolition waste, household waste, bulky waste, wood, excavated surface, glass, old tires, wastepaper, concrete, brick, tile or ceramic mixture. The sorting station also has the function of a transhipment centre for mixed household waste [10].

2.2.4. Biogas Plant

The biogas generated at the plant (up to 3,000 m^3 per day, methane content 65 %) is used as fuel in the on-site combined heat and power plant with an installed capacity of 300 kW. In a biogas plant, sewage sludge can be handled anaerobically together with other organic waste, which can be up to 10 % of the total volume as dry matter [10].

2.2.5. South Estonian Hazardous Waste Management Centre

In the administrative territory of the city of Tartu, the Southern Estonia hazardous waste management centre operates, which is managed by the hazardous waste management company Epler&Lorenz that operates on the same property. The management of the hazardous waste collection system is the responsibility of the state (i.e., the city of Tartu has no obligations in managing the centre). In addition to the collection of hazardous waste, waste is burned in a waste incineration plant, and polluted soil is cleaned using bag composting technology [26].

2.2.6. Statistic Data on Waste and Biogas Amount

Statistical information on waste collected in Tartu in 2019 and 2021 is shown in Table 4 below.

Table 4. Waste Collected in Tartu in 2019 and 2021, t

Waste category	**2019**	**2021**
Construction and demolition debris, including soil removed from contaminated land areas	214 515	215 594
Waste from waste management companies, non-company wastewater treatment plants, and drinking and industrial water management	83 595	130 805
Waste generated in agriculture, horticulture, aquaculture, forestry, hunting and fishing and food preparation and processing	64 625	58 734
Municipal waste (household waste and similar commercial, industrial and official waste), including separately collected waste	42 946	41 459
Packaging waste, absorbents not listed elsewhere, cleaning rags, filter materials and protective clothing	17 865	16 666
List of waste not specified elsewhere	8 371	7 956
Waste from mechanical shaping of metals and plastics and physical and mechanical surface treatment	4 175	3 887
Waste generated in organic chemical processes	1 249	1 550
Oil and liquid fuel waste (except edible oils)	594	768
Waste generated during human or animal health care or related research (except kitchen and canteen waste that is not directly related to health care)	513	601
Waste generated in thermal processes	159	550
Waste from the manufacture, mixing, distribution and use of surface coatings (paints, varnishes and vitreous enamels), adhesives, sealants and printing inks	517	539
Photographic waste	23	24
Waste generated during the surface treatment and coating of metals and other materials and hydrometallurgical processes of non-ferrous metals	8	20
Wastes of organic solvents, refrigerants and propellants	14	17
Waste from wood processing, tiles and furniture and pulp, paper and cardboard production	47	12
Total	439 216	479 182

Source: [25]

Total value of collected waste increased by 9 % in 2022 compared to 2019. The main part of waste collected by Tartu city is formed by construction waste (47 % of total average waste amount collected in 2019 and 2022). The second position takes waste

from waste management companies, non-company wastewater treatment plants, and drinking and industrial water management (23 %; see Fig. 3 below).

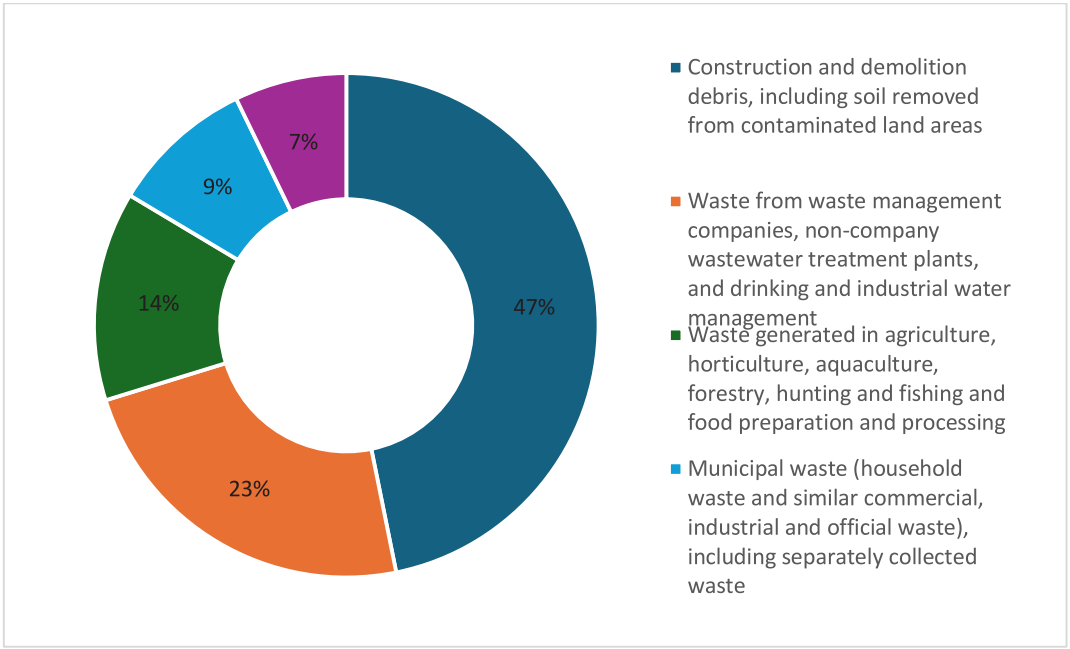

Fig. 3. Average composition of waste collected by Tarty city in 2019 and 2021.

Source: [25]

According to Table 5, at least 61 % of waste generated and imported to Tartu city is recycled. There is a high recycling level of construction and agricultural waste – 75 % and 100 %.

Table 5. Waste Recycled in Tartu in 2019, t

Waste category	**Collected**	**Imported**	**Total managed**	**Recycled**	**Recycling rate**
Construction and demolition debris, including soil removed from contaminated land areas	214 515	20 616	235 131	176 524	75 %
Waste from waste management companies, non-company wastewater treatment plants, and drinking and industrial water management	83 595	1 566	85 161	8 810	10 %
Waste generated in agriculture, horticulture, aquaculture, forestry, hunting and fishing and food preparation and processing	64 625	31 284	95 909	95 560	100 %
Municipal waste (household waste and similar commercial, industrial and official waste), including separately collected waste	42 946	2 227	45 173	5 698	13 %
Other waste	33 535	5 646	39 181	20 530	52 %
Total	439 216	61 339	500 555	307 122	61 %

Source: [25]

Figure 4 illustrates the amount of waste incinerated in Tartu in 2020–2023. The volume of incineration will gradually increase since 2020 by reaching 24 757 tons in 2023.

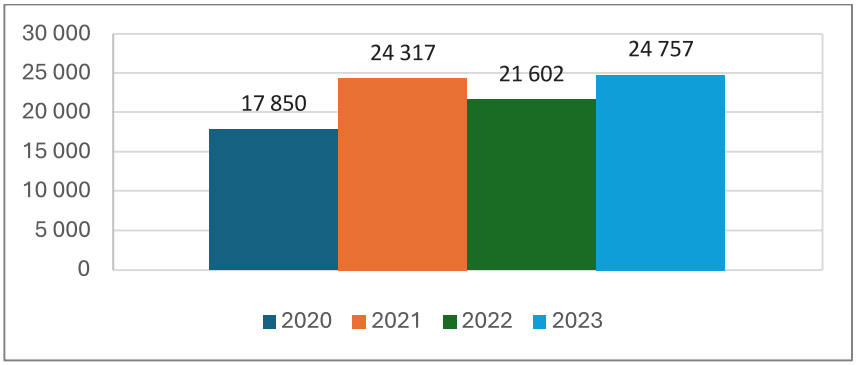

Fig. 4. Mixed household waste incinerated in Tartu in 2020–2023, t.

Source: [25]

Figure 5 illustrates the volume of biogas produced in Tartu in 2021–2023 and its methane content (through the gas collection system of the closed landfill in Aardlapalu).

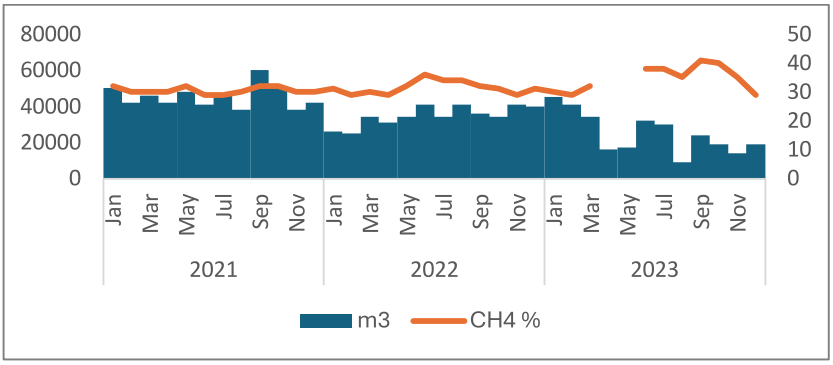

Fig. 5. Statics on biogas produced in Tartu in 2021–2023 and its methane content.

Source: [25]

Volume of produced biogas reduced by 62 % comparing December 2023 to January 2021. The average content of methane equals 32 %.

3. SIMILARITIES AND DIFFERENCES

The common and different features of Getlini and Tartu waste management processes are reflected in Table 6.

Table 6. The Common and Different Features of Getlini and Tartu Waste Management Processes

Similarities	
Getlini and Tartu city have similar waste processing opportunities – sorting station, biogas plant and landfill. In 2021, Getlini and Tartu managed comparable volume of waste. Getlini – 513,761 tons; Tartu – 479,182 tons.	
Differences	
Getlini, Latvia	Tartu Municipality, Estonia
Getlini is a company formed jointly by the municipalities of Riga and Ropazi. Getlini does not operate as a recycling station, the main function of Getlini is management of waste, which is directed to landfill cell – the last stage of waste management process. Total amount of waste received in 2021–2023 by Getlini is gradually decreasing, i.e., by 24 % comparing 2023 to 2021. The main change is acknowledged in construction waste (-56 % comparing 2023 to 2021) due to an increase in tariffs. 59 % of waste received by Getlini is formed by unsorted household waste. Getlini managed 22 % of total produced waste in Latvia in 2021. However, Getlini received more than half (55 %) of unsorted household waste and 73 % of biowaste generated in Latvia in 2021. In 2023, Getlini landfilled 53 % of the received waste. The value of landfilled waste significantly increased in 2022 due to reaching of maximum capacity of bioreactor in May 2022 where notable amount of household waste suitable for composting or anaerobic digestion was placed. Industrial waste received by Getlini has the highest landfilled proportion that reached 100 % of total received industrial waste in 2023,	Tartu is a municipality, which organises the collection and transport of household waste; it does not take the function directly. Waste management processes are taken by merchants through public tender. Tartu municipality takes the role of control. Total value of collected waste in Tartu increased by 9 % in 2022 compared to 2019. Waste mainly is formed by construction waste (47 %). Tartu uses an opportunity to incinerate mixed household waste. Tartu has a high recycling level of construction and agricultural waste – 75 % and 100 %.

Volume of waste, its composition and management processes do not correlate between Getlini and Tartu. It triggers a requirement for development of aligned waste sampling and testing procedures.

4. WASTE SAMPLING AND ANALYSIS

4.1. Getlini, Latvia

According to Cabinet Regulation No 1032 and Category A Polluting Activity Permit, Getlini is testing the following types of waste: residuals from sorting of unsorted household waste (household waste after sorting that is landfilled) and mechanically separated BDW, which is transferred to BDW recycling complex (from unsorted household waste).

Getlini conducts composition measurements of sorting residuals once a quarter by inviting an accredited laboratory, which determines the specific weight of each fraction in the residuals. Determining the com-

position of household waste for disposal, the waste is sorted into the following fractions:

1. paper and waste containing paper (e.g., packaging, paperboard, tetra packages, mixed wastepaper and paperboard);
2. plastic and plastic-containing waste (for example, packaging, film, mixed plastic waste);
3. glass and glass-containing waste;
4. wastes containing metals;
5. BDW and biowaste;
6. construction and demolition waste;
7. waste electrical and electronic equipment;
8. waste batteries and accumulators;
9. textile waste;
10. large waste (at least one external dimension exceeding 50 cm);
11. fine fraction (dimensions of household waste less than 10 mm);
12. other household waste that does not fit into the fractions mentioned in this point.

Sample preparation is carried out by laboratory specialists in accordance with the methodology established by Cabinet Regulation No 1032, namely, samples of household waste are taken from all waste loads within a specified period of time (the incoming loads are directed to the unsorted household waste sorting plant, the sample is taken from a waste pile that contains post-sorting waste and is prepared for transportation to the disposal site).

Household waste from which a sample will be taken shall be discharged into a conical stack and divided vertically into four equal parts in two imaginary lines. Two opposite quarters of the conical pile are mixed into one sample in a conical pile, which is then again divided vertically into four equal parts in two imaginary lines, but the remaining two quarters are not included in further operations. These actions are repeated until the household waste sample size is reached.

Laboratory specialists manually sort the household waste sample according to the household waste fractions. After sorting, the waste from each household waste fraction is weighed and their weight is recorded. The sample size varies on average from 100 to 250 kg.

Getlini, in addition to the mandatory testing conducted once a quarter, also analyses the composition of unsorted household waste (received household waste before sorting) using the same approach and determining the same fractions as for the residual of sorted household waste [14].

The sampling and testing procedure is prescribed by Cabinet Regulation No 1032.

To verify the efficiency of unsorted household waste sorting process and determine whether the BDW contains a sufficient proportion of biological waste for further processing (the content of impurities may not exceed 30 %), Getlini shall, by inviting an accredited laboratory, perform testing of BDW sorted from household waste once a week, determining the following parameters:

1. percentage by mass of moisture (standard LVS CEN/TS 15414-1:2020);
2. non-biomass percentage (standard LVS EN ISO21644:2021);
3. percentage by mass of inert waste (standard LVS EN ISO21644:2021);
4. mass percentage of biomass content in a dry sample (standard LVS EN ISO 21644:2021);
5. percentage by mass of the number of impurities in the wet sample – calculation.

Moreover, in addition to waste composition, Getlini started testing of chemical parameters of:

1. residuals of sorted household waste, which is currently being landfilled;
2. mixed construction waste, which is currently being landfilled;
3. waste resulting from sieving of the fermented mass from BDW recycling complex, which is currently being landfilled;
4. wood-containing waste accepted at the construction and demolition waste and bulky waste sorting line, primarily consisting of wood from construction waste, furniture, packaging, garden, and park waste, etc., and which, after accumulating a certain volume, is handed over to other waste management operators (woodchips).

Table 7 reflects parameters that are determined within chemical analysis.

Table 7. Chemical Parameters that are Determined in Waste by Testing Laboratory Invited by Getlini

Parameter	**Measure**
Moisture content	%
Ash content	%
Gross calorific value at constant volume	MJ/kg, kcal/kg MWh/t
Net calorific value at constant pressure	MJ/kg, kcal/kg MWh/t
Sulphur	%
Nitrogen	%
Total carbon content	%
Hydrogen	%
Fines <10mm	%
Biomass content (selective dissolution method)	%
Biomass content (selective dissolution method) express as percentage carbon of total carbon	%
Shrinkage starting temperature	°C
Deformation temperature	°C
Hemisphere temperature	°C
Flow temperature	°C
Chemical elements: Na, Mg, Al, Si, P, K, Ca, Ti, Cr, Mn, Fe, Ni, Cu, Zn, As, Cd, Hg, Pb,	mg/kg
Chemical elements: S, Cl	%

Source: [26]

4.2. Tartu Municipality, Estonia

In the city of Tartu, there is no regular testing in place, and there is no regulated procedure for such testing. The Ministry of Environment orders sorting studies at the interval of 2–3 years. These studies gather data from 3–4 municipalities, and the data is generalised for the whole country. Usually, studying does not cover Tartu municipality. Therefore, the data does not represent the situation in Tartu. Tartu has conducted its own surveys described below.

Sorting studies have been carried out in 2011 when the study of biogas raw materials of Tartu city and Tartu County was carried out by the Institute of Sustainable Estonia. In October 2019, Tartu carried out waste sorting survey MAVES Tallinn, and in December 2023 the municipal waste sorting

study was carried out by Tartu City Government. Within this framework, the average composition of Tartu's mixed municipal waste was assessed. These were carried out by Tartu city to assess how much recyclable material went to waste as mixed household waste.

Sampling of the analysed waste was carried out based on the international and methodological framework used in the previous household waste studies conducted in Estonia (including Tartu):

1. Standard EVS-EN14899:2006 – Characterization of waste. Sampling of waste materials. A framework for preparing and implementing a sampling plan;
2. Methodological guidance material NT ENVIR 001: Solid Waste, Municipal: Sampling and Characterization prepared by Nordtest;
3. American standard ASTM D5231-92(2016): Standard Test Method for Determination of the Composition of Unprocessed Municipal Solid Waste [10].

The waste samples were taken from the waste loads previously agreed with the waste handlers, which were collected from the respective study areas. A total of five samples were taken from each load. Data on the analysed waste loads, the number of containers making up the waste load for 2023 and sample weights are given in Table 8.

Table 8. Data on the Analysed Waste Load, the Number of Containers Making Up the Waste Load and the Average Weight of the Samples Taken for Analysis, 2023

Data of the study period		Annelinn	Former Tähtvere municipality	Variku	City Centre	Mean
Study period I	Number of containers	51	91	322	114	145
	Load weight, t	6,8	5,0	8,6	3,2	5,9
	Average sample weight, kg	93.2	93.0	93.5	100.7	95.08
Study period II	Number of containers	51	90	171	172	121
	Load weight, t	7,2	2,4	4,3	7,4	5,3
	Average sample weight, kg	99.6	95.8	95.8	96.2	96.84
Study period III	Number of containers	51	90	171	172	121
	Load weight, t	7,2	2,3	4,3	7,4	5,3
	Average sample weight, kg	97.5	109.9	91.5	98.1	99.25
Study period IV	Number of containers	61	220	192	124	149
	Load weight, t	6,1	6,2	5,0	5,9	5,8
	Average sample weight, kg	94.9	95.7	96.8	98.2	96.4

Source: [25]

The waste from Variku, Annelinna, Kesklinna districts and former Tähtvere municipality was analysed at the Aardlapalu transfer station (Kambja parish, Uhti village, Aardlapalu). The waste load was mixed and spread out in an even layer. The scattered waste was divided into four groups, and after grouping the waste and reducing the amount of material, a waste sample weighing about 100 kg was taken into a 600–770 litre container.

The waste sample was manually sorted on a sorting table (including screening out particles smaller than 20 mm) according to the agreed waste types, and then the separated waste types were weighed.

Based on the aggregated results of the sorting study, it can be stated that the largest proportion of the analysed mixed household waste is biowaste (29.9 %) and other combustible material (diapers and sanitary napkins, rubber, cotton wool, contents of vacuum cleaner bags, roll material for floor covering), followed by paper and cardboard (16.45 %) and plastic (15.45 %).

In addition to the mixed household waste sorting survey, Tartu city also carried out observations of mixed household waste at the client's premises – the so-called garbage bingo project.

At the customer's place, the mixed household waste container was emptied into the garbage truck, and it was assessed by external observation whether there was inappropriate waste in the container. On the spot, the data was entered into the information system and the contents of the container poured into the car were photographed. In case of non-compliant waste, the customer was contacted. In 2023, it was organised three times, and approximately 1000 containers were analysed [10].

A comparison of the aggregate results of this sorting study with the results of similar studies previously conducted in Tartu (2011 and 2019 studies) is provided in Table 9.

Table 9. A Comparison of the Aggregate Results of Sorting Studies Conducted in Tartu in 2011, 2019 and 2023

Waste type (material based)	2011 average	2019 average	2023 average
Glass	3.2	4.4	6
Plastic	15.2	16.6	15.4
Paper and cardboard	17.1	20.2	16.5
Metal	2.2	2.3	1.5
Wood	0.5	0.9	0.6
Bio waste including:	38.4	31.8	29.1
garden waste	9.4	7.5	4.7
kitchen waste	27.6	24.3	23.4
other biowaste	1.4	0.1	1
Textiles and clothes	0.9	5.9	3.6
Hazardous waste	0.3	0.6	0.1
Electronic waste	0.4	0.6	0.9
Other non-combustible (inert) material	6.1	5.4	3.6
Other combustible material	15.7	11.3	22.7
Total	100	100	100

Source: [10]

When comparing the results of this study with previous studies, the biggest change in the direction of increase has occurred in the content of other combustible materials. At the same time, it must be taken into account that the share of this type of waste is relatively large, and as the share of other types of waste (especially biowaste) changes, it increases. Therefore, it is more important to pay attention to the decrease in the proportion of biowaste compared to the previous sorting survey. The decrease in the proportion of biowaste compared to the 2011 sorting survey is particularly noticeable. The promotion of separate collection of biowaste in recent years in Tartu has contributed to the decrease in the proportion of biowaste.

5. CONCLUSIONS

- The regulatory framework for waste management in Latvia and Estonia is comprehensive, featuring multiple regulatory enactments that are supplemented by the National Waste Plan. Latvia and Estonia have similar responsibilities, permitting system and reporting. Supervision of waste management in Latvia and Estonia are similarly entrusted, with main supervisory institutions – state bodies.
- In Latvia, waste management reporting is a collaborative effort between the public and private sectors, encompassing various stakeholders such as specialised waste managers and local governments. Meanwhile, in Estonia, reporting is apparently only the duty of certain representatives of the private sector. In Latvia, the need to submit financial security in order to receive a waste management permit is determined for more permits for certain activities compared to Estonia. Persons wishing to obtain a waste management permit for certain activities must pay a state duty. Meanwhile, the Estonian regulation does not provide information about the obligation to pay the state duty.
- Getlini and Tartu city have similar waste processing opportunities – sorting station, biogas plant and landfill. In 2021, both have processed comparable amount of waste: Getlini – 513,761 tons; Tartu – 479,182 tons. The main difference between Getlini and Tartu is that Getlini is a company formed jointly by the municipalities of Riga and Ropazi, the main function of which is management of waste that is directed to landfill cell, and Tartu is municipality that organises collection and transport of household waste.
- The waste profile of Tartu is predominantly characterised by construction waste (47 %). 59 % of waste received by Getlini is formed by unsorted household waste. Tartu uses mixed household waste for incineration and has a very high recycling level of construction and agricultural waste, 75 % and 100 %, respectively. In 2023, Getlini landfilled 53 % of the received waste. The value of landfilled waste significantly increased in 2022 due to reaching maximum capacity of bioreactor in May 2022 where notable amount of household waste suitable for composting or anaerobic digestion was placed. Production waste received by Getlini has the highest landfilled proportion that reached 100 % of total received production waste in 2023.
- Volume of waste, its composition and management processes do not correlate between Getlini and Tartu. It triggers a requirement for development of aligned waste sampling and testing procedures.
- Based on requirements of legislative acts, Getlini is testing residuals of sorted household waste (household waste after sorting that is landfilled) and mechanically separated BDW, which is transferred to BDW recycling complex (sorted household waste). The test includes analysis of morphology of waste aimed at determining whether the waste meets the requirements for landfill or recyclable waste. In the city of Tartu, there is no regular testing in place, and there is no regulated procedure for such testing.
- The procedures for waste sampling and analysis of residuals of household waste

after sorting at Getlini are governed by stringent legislative acts, ensuring consistency in the sampling process, the quantity and fractions of samples collected.

- Within the scope of this study, Getlini made the following tests of waste:
  - chemical test of residuals of sorted household waste, which is currently being landfilled. According to mandatory morphological test, 68 % of residuals are formed by paper and plastic. Chemical parameters have similar measures at all testing dates, except for results of some chemical elements that have significant fluctuations;
  - morphological and chemical test of mixed construction waste, which is currently being landfilled. The main part of mixed construction waste is formed by fines in fractions below 10 mm. Chemical parameters of tested mixed construction waste have significant fluctuations at testing dates;
  - chemical test of waste resulting from sieving of the fermented mass of the BDW from BDW recycling complex, which is currently being landfilled. Chemical parameters at testing dates have low volatility around average value, except for chemical elements that fluctuate a lot;
  - chemical test of wood-containing waste (woodchips). Since woodchips are placed out of doors, these are affected by weather conditions. As a result, moisture content has significant fluctuation at testing dates that impacts calorific values. Moreover, chemical elements have high volatility around average values.
- By involving an accredited laboratory for precise waste sampling, Getlini adheres to internationally recognised standards and national regulations, ensuring robust and accurate manual separation of waste into 12 distinct fractions. Sample size is considered appropriate to get overview of the waste, it is also in line with the requirements of Cabinet Regulations No 1032, international practice and standards:
  - for residual of sorted household waste from 100 to 250 kg;
  - for mixed construction waste from 300 to 400 kg.

ACKNOWLEDGEMENT

The research has been funded by I3-2022-CAP2b, project “Circular Economy for Riga and Tartu Waste Management Facilities” (CERITA), Grant Agreement from 101133105.

REFERENCES

1. Eurostat. (2023). *Waste Statistics*. Available at https://ec.europa.eu/eurostat/statistics-explained/index.php?title=Waste_statistics
2. Ozbay, G., Jones, M., Gadde, M., Isah, S., & Attarwala, T. (2021). Design and Operation of Effective Landfills with Minimal Effects on the Environment and Human Health. *Journal of Environmental and Public Health*, 1–13. 10.1155/2021/6921607.
3. Hoang, M., Pham P., Song, T., Fujiwara, T.,

& Pham Van, D. (2020). Waste-to-Landfill Reduction: Assessment of Cost-Effective Solutions using an Optimization Model. *Chemical Engineering Transactions*, *78*. 10.3303/CET2078086.

4. Parveen, N., Azam, R., & Dingh, D. (2020). *Innovations in Recycling for Sustainable Management of Solid Wastes*. IGI Global. 10.4018/978-1-7998-0031-6.ch010.
5. Sauhats, A., Broka, Z., & Baltputnis, K. (2021). Energy Transition of the Baltic States: Problems and Solutions. *Latvian Journal of Physics and Technical Sciences*, *58* (3), 3–14. doi: 10.2478/lpts-2021-0013.
6. EC. (1999). *Council Directive 1999/31/EC of 26 April 1999 on the Landfill of Waste*. Available at http://data.europa.eu/eli/dir/1999/31/oj
7. MK. (2021). *Atkritumu apsaimniekošanas valsts plāns 2021.–2028. gadam*. Available at https://www.varam.gov.lv/lv/media/6191/download?attachment
8. LSM.lv (2023). *Landfills Still Bury too much Waste in Latvia*. Available at https://eng.lsm.lv/article/society/environment/03.04.2023-landfills-still-bury-too-much-waste-in-latvia.a503495/
9. Estonian Ministry of the Environment. (2023). *National Waste Plan 2022–2028*. Available at https://www.envir.ee/j%C3%A4%C3%A4tmekavaksh
10. Tartu Municipality. (n.d.) *Tartu City Provided Description of Waste Management Processes*. Available at https://tartu.ee/en/waste-management
11. Zigurs, A., Balodis, M., Ivanova, P., Locmelis, K., & Sarma, U. (2019). National Energy and Climate Plans: Importance of Synergy. *Latvian Journal of Physics and Technical Sciences*, *56* (6), 3–16. doi: 10.2478/lpts-2019-0031.
12. Getlini.lv (2024). *Getliņi EKO Statistical Data on Received, Used and Landfilled Waste for 2021–2023.* Available at https://www.getlini.lv/publicets-uznemuma-auditetais-gada-parskats-par-2023-gadu/
13. Latvijas Vides, ģeoloģijas un meteoroloģijas centrs. (2022). *Valsts statistiskā pārskata "Nr.3 – Atkritumi. Pārskats par atkritumiem" kopsavilkums par 2021.g.* Available at https://www.google.com/url?sa=i&url=https%3A%2F%2Fvidescentrs.lvgmc.lv%2Ffiles%2FVide%2FAtkritumi_un_radiacijas_objekti%2FNr_3_parskats_par_atkritumiem%2F3Atkritumi_kopsavilkums_2021.pdf&psig=AOvVaw27EAIXwLOsQodau33OxViH&ust=1723181726218000&source=images&cd=vfe&opi=89978449&ved=0CAYQrpoMahcKEwjorZGn1uSHAxUAAAAAHQAAAAQBA
14. Getlini.lv. (n.d.). *Description of Activities of Geliņi EKO*. Available at https://www.getlini.lv/
15. Kamil, F. H., & Waleed, M.A. (*2021). Circular Economy and Solid waste Management for Sustainable Environment.* Available at https://www.researchgate.net/publication/357555187_Circular_Economy_and_Solid_waste_Management_for_Sustainable_Environment
16. Zemite, L., Kleperis, J., Mezulis, A., Bode, I., Vempere, L., Jasevics, A., & Jansons, L. (2022). Biogas Production Support Systems for the Production and Use of Biomethane. In *2022 IEEE International Conference on Environment and Electrical Engineering and 2022 IEEE Industrial and Commercial Power Systems Europe*, (pp. 1–6). Prague, Czech Republic. doi: 10.1109/EEEIC/ICPSEurope54979.2022.9854739.
17. EPA. (n.d.). *Basic Information about Landfill Gas*. Available at https://www.epa.gov/lmop/basic-information-about-landfill-gas
18. Savickis, J., Zemite, L., Zeltins, N., Bode, I., Jansons, L., Dzelzitis, E., … & Ansone, A. (2020). The Biomethane Injection into the Natural Gas Networks: The EU's Gas Synergy Path. *Latvian Journal of Physics and Technical Sciences*, *57* (4), 34–50. doi: 10.2478/lpts-2020-0020.
19. Zemite, L., Jansons, L., Zeltins, N., Lapuke, S., & Bode, I. (2023). Blending Hydrogen with Natural Gas/Biomethane and Transportation in Existing Gas Networks. *Latvian Journal of Physics and Technical Sciences*, *60* (5), 43–55, doi: 10.2478/lpts-2023-0030.

20. Jansons, L., Bode, I., Koposovs, A., Zeltins, N., & Lapuke, S. (2023). Gas Distribution System of Latvia and its Transitional Challenges. *Latvian Journal of Physics and Technical Sciences*, *60* (6), 85–99. doi: 10.2478/lpts-2023-0038.
21. Selickis, A., Jansons, L., Bode, L., Zemite, L., & Zeltins, N. (2023). Basis of operational planning methodology in diversified gas distribution systems. In *2023 IEEE 64th Annual International Scientific Conference on Power and Electrical Engineering of Riga Technical University, RTUCON 2023 – Proceedings*, (pp. 1–15). 9–11 October 2023, Riga, Latvia. Piscataway: IEEE. doi: 10.1109/RTUCON60080.2023.10412954.
22. Jansons, L., Silina, J., Bode, I., Zemite, L., Zeltins, N., & Palkova, K. (2024). Injection of Renewables Gases into the Existing Gas Distribution Grids and Employment of Reverse Gas Flow Technique. *Latvian Journal of Physics and Technical Sciences*, *61* (2), 66–79. doi: 10.2478/lpts-2024-0013.
23. MC Regulations. (2011). *Regulations Regarding Landfill Sites*. Available at https://likumi.lv/ta/id/242189-atkritumu-poligonu-noteikumi
24. Dianda, P., Taleb, M.A., & Munawar, E. (2018). Production and Characterization Refuse Derived Fuel (RDF) from High Organic and Moisture Contents of Municipal Solid Waste (MSW). *IOP Conference Series Materials Science and Engineering, 334* (1), 012035. doi: 10.1088/1757-899X/334/1/012035
25. Tartu Municipality. (n.d.) *Statistical Data on Waste*. Available at https://tartu.ee/en/sustainable-tartu
26. Virsma SIA. (n.d.). *Testing Reports*. Available at https://www.virsma.lv/

sciendo

LATVIAN JOURNAL OF PHYSICS
AND TECHNICAL SCIENCES
2024, N 5

DOI: 10.2478/lpts-2024-0036

MAIN STAGES AND RESULTS OF THE DEVELOPMENT OF MOBILE SPACE ENVIRONMENT SIMULATION FACILITY "METAMORPHOSIS"

J. Gutans*, N. Mozga, A. Klokovs, N. Glizde, M. Kleinhofs

Institute of Aeronautics,
Faculty of Civil and Mechanical Engineering,
Riga Technical University,
6B Kipsala Street, Riga, LV-1048, LATVIA
*e-mail: jurisg777@gmail.com

This article presents the main stages and results of the project "Mobile Space Environment Testing Equipment Development of "Metamorphosis" Prototype for Transportation Intermodal Traffic". For successful implementation of the project, the project has been divided into four stages: 1) Design calculations and design documentation for the design elements of the prototype; 2) Prototype software development; 3) Manufacturing of construction details and prototype assembly; 4) Industrial research and prototype testing. The goal of the project is, based on industrial research, to develop a prototype of the Mobile Space Environment Test Facility (MSTF) "Metamorphosis" transported in an intermodal environment, and to achieve the level of scientific and technical readiness of MSTF from TRL2 to TRL4 (by the scale of the European Space Agency (ESA)) for further development of the project. This project is unique and has no comparable analogues, as all existing test facilities are stationary. The project is implemented by Riga Technical University in cooperation with Cryogenic and Vacuum Systems Ltd.

Keywords: *Calculation, CubeSats, satellite technology, test requirements, test systems, vacuum pumping system, vacuum system.*

1. INTRODUCTION

A while ago, outer space was an exceptional territory where only governments of major powers and large corporations could implement their projects. The situation has changed radically over the past 20 years. New companies – start-ups – have begun to offer inexpensive access to space and, as a result, space has become more cost-effective. Technological trends, such as

- reducing the size of microprocessors,
- reducing launch costs,
- shorter development cycles,
- rapid technological improvement,
- new operational models,

are associated with miniaturisation of satellite technologies and have led to an exponential increase in the use of small satellites, creating new advantages for space projects.

All of these benefits will continue to drive the adoption of small satellites over the next decade and create new opportunities in education, commerce, government and science. The Union of Concerned Scientists estimated that there were 4,550 active satellites on the Earth's orbit in early 2023 [1]. The most common of these satellites were CubeSats, which made up to 70 % of all active satellites and were not state meteorological satellites or large communications satellites.

An increase in the number of small satellites can be explained not only by many unique advantages that they offer to science, business and society, but also by an increase in their lifespan, which is a huge benefit for the customer. The development of design technologies and the improvement of testing systems contribute to this benefit. While satellite is in operation, it is impossible to timely repair any of its elements; therefore, the testers are required to foresee all possible variants of the situations in which the spacecraft will be involved. That is why sets of tests are carried out and during these tests different extreme conditions, thermal behaviour of the satellite and its functionality are studied and analysed. As a result of the tests, the system's stability is evaluated. Thermal vacuum chambers are used to simulate space environment conditions as accurately as possible.

Such testing is carried out by special testing centres, which are stationary. The services of these centres are expensive and not always available to small companies, societies, educational institutions, etc. This problem can be solved by creating a mobile ground simulator of space conditions, with the help of which it would be possible to provide testing services at the request of the customers in a place and time acceptable to them [2]. Such type of project called Metamorphosis was developed at the Institute of Aeronautics of Riga Technical University ["Prototype Development of Transportable in Intermodal Traffic Mobile Space Testing Facility (MSTF) "Metamorphosis"" (Metamorphosis, project No. 1.1.1.1/18/A/133)] [3] in cooperation with Cryogenic and Vacuum Systems Ltd. This company specialises in the development and production of vacuum and cryogenic equipment. It has extensive experience in creating technologies used in space research and the development and operation of space environment simulators [4]. This cooperation project is unique and does not have any comparable analogues – all existing testing facilities are stationary. The main difference of the Prototype MSTF "Metamorphosis" from existing test facilities is the ability to maintain operational characteristics in conditions of intermodal transport, i.e., in conditions of

vibration, shock, linear accelerations and angular displacements.

During the implementation of the project, the following 15 tasks have been consistently solved.

1. The analysis of existing technical solutions suitable for the development of prototype MSTF "Metamorphosis" has been carried out. In total, about 500 test facilities have been examined. The geometric and mechanical characteristics, composition and characteristics of the vacuum and cryogenic systems, alongside with operational characteristics of those facilities have been analysed. An analysis has also involved checking whether the requirements of ISO, ECSS and NASA standards have been met.
2. Based on the analysis, a generalised composition of the main systems, technical requirements for the Prototype, and the concept of its structure have been developed. The geometry characteristics of the test object (CubeSat sample) have been determined, and the geometric characteristics of the vacuum chamber of the Prototype have been calculated.
3. Based on the test object characteristics, the mean free path has been calculated for various test modes in molecular, viscous and transient modes, taking into account the Sutherland model and amendments for the Lennard-Jones potential. Based on the results obtained, the Knudsen number for different operation modes has been determined. The geometric characteristics of the vacuum chamber have been refined, taking into account the presence of cryogenic shrouds and minimising the parasitic heat inflow to the shrouds and the test object. Thus, by varying parameters and finding their mutually acceptable ranges, the geometric characteristics of the prototype vacuum chamber have been determined.
4. Various types of tests and modes of the Prototype operation have been analysed and their characteristics of the atmosphere (gas load, composition, etc.) have been determined. Based on the results obtained and in accordance with the requirements of the ISO, ECSS and NASA standards, the general requirements for allowable pressure have been determined for various types of the Prototype operating modes.
5. A pneumatic diagram and a preliminary layout of the vacuum system have been developed.
6. A mathematical model has been created, which includes a module for simulating of vacuum system gas load in various modes, a module for calculating the conductivity of elements of a vacuum system and a vacuum chamber, and a module for calculating the characteristics of vacuum pumps.
7. Based on the simulation results, technical requirements for vacuum pumps, valves, pipelines and gauges have been determined.
8. During the design and calculations, a systematic analysis of technical risks has been carried out, and the most vulnerable elements have been identified. It has been found that the greatest risks are exposed to: high-vacuum pumping system – vacuum valves, turbomolecular pumps, Stirling and Gifford-McMahon cryocoolers in cryogenic pumps; vacuum seals; thin-walled pipelines of cryogenic and vacuum systems with linear expansion joints, membrane bushings, cryogenic shrouds panels, vacuum chamber body; standard bellows, unloading and compensating spring elements of the cryogenic screen, fastening systems for the test object; a simulator of solar radiation, optical

feedthroughs; Van Allen belts simulator.

All analysed components exposed to risks have been divided into two groups:

- components for which it is possible to purchase options in vibration-shock-proof performance;
- elements requiring special design and technological measures to prevent damage and/or destruction.

9. Since the vacuum system has been identified as the system subject to the greatest technical risks, it has been decided to apply continuous postoperative verification control. The most objective control method that allows for a comprehensive assessment of the presence or absence of the main risks to the system's operation is tightness control.
10. An analysis of existing methods of leakage control has been carried out and, as a control method for the Prototype tests during test drives, a leak control method using a helium leak detector has been determined by comparing the leakage of the test object with the readings of a control leak.
11. A thermodynamic model of the Prototype has been developed. As a result of the simulation, the geometry of the cryogenic shrouds, cryogenic pipelines and other parameters of the Prototype cryogenic system have been obtained, common vacuum-cryogenic diagram and layout have been designed.
12. Based on the analysis of the requirements of the ISO, ESA ECSS and NASA standards and the results of the analysis of the prototype operation during various types of tests and modes, the prototype operation algorithms have been developed.
13. Based on the developed technical requirements, technical specifications have been drawn up, an analysis of the materials and components market and their procurement for the manufacture of a vacuum system, a vacuum chamber, cryogenic shrouds, and elements of a control system have been carried out. As components are received, incoming control is carried out. Manufacturing, assembly, installation of structural elements of the Prototype systems and their testing have been carried out. In particular, the assembly and testing of the elements of the fore-vacuum and high-vacuum systems have been carried out.
14. On the basis of the simulation results, sketches of the system's design have been developed.
15. Based on the analysis of the measurement processes during the Prototype's test, vacuum and cryogenic diagram analyses, a list of the Prototype control system sensors with technical requirements and the sensor interfaces list have been determined.

This article describes the main stages of the development of the mobile thermal vacuum chamber to be used for testing CubeSats.

2. DESIGN CALCULATIONS AND DESIGN DOCUMENTATION FOR THE DESIGN ELEMENTS OF THE PROTOTYPE

The main task of the project is to create such a Prototype, the qualities of which are to be verified both from the point of view of compliance with the main characteristics of space environmental simulators [5]–[7] and from the point of view of maintaining performance after repeated transportation in intermodal transportation. The design

of the vacuum pumping system and the Prototype leakage system must meet the above technical requirements. The purpose of vacuum calculation is to determine the design and technical requirement for the vacuum chamber, vacuum pumping system and associated facilities of the Prototype, as well as to create a specification and vacuum diagram of the Prototype.

We can single out the minimum requirements for the composition of the equipment of the test complex, which have allowed for the development and testing of space technology under conditions of imitation of outer space:

- the presence of a high-vacuum pumping system;
- availability of a system for simulating heat flows to simulate heat flows of the Sun and planetary surfaces;
- availability of a system of nitrogen cryogenic shrouds, simulating “black” space;
- availability of a control system for temperature and other parameters of the spacecraft;
- availability of a pressure control system in the vacuum chamber.

2.1. Determination of the Structural Appearance of the Prototype Vacuum Chamber

The vacuum chamber of a facility intended for testing space technology, while simulating the conditions of an operating environment, is a unique product of individual development and manufacture. The correct definition of the design of the vacuum chamber not only determines the ease of use of the test bench, but also has a significant impact on its operational capabilities and characteristics. On the basis of the analysis, it has been decided to adopt a cylindrical vacuum chamber for a horizontal structural type (Fig. 1) for equipping the Prototype [8].

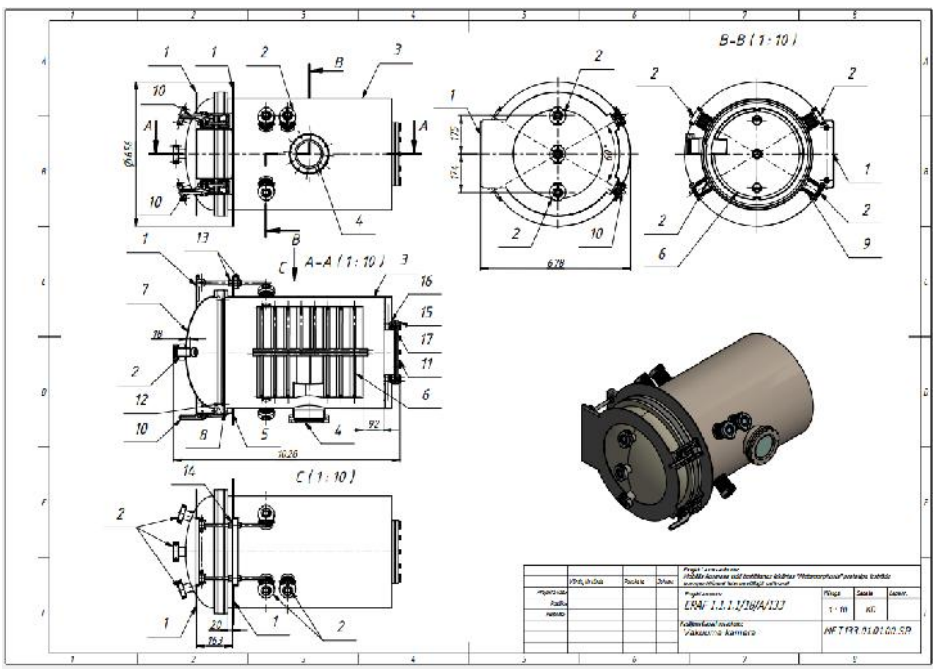

Fig. 1. Drawing of vacuum chamber.

2.2. Determination and Calculation of Geometric Characteristics of the Prototype Vacuum Chamber

The most probable test objects for the Metamorphosis mobile space testing facility are micro- (10–100 kg) and nano- (1–10kg) spacecraft, as well as parts and assemblies of such and larger spacecraft. The most common, and, therefore, probable type of such spacecraft is CubeSat. Based on the analysis of potential spacecraft to be tested, it has been decided to tentatively accept for the Prototype conditionally:

- minimum dimensions of the test object (LxWxH) 227x100x100 mm and mass 2.5 kg;
- nominal dimensions of the test object (LxWxH) 345x105x105 mm and mass 5 kg;
- maximum dimensions of the test object (LxWxH) 400x250x250 mm and mass 15 kg.

Determination of the Diameter and Length of the Cylindrical Part of the Vacuum Chamber

The diameter of the vacuum chamber [7] can be determined as the sum of the characteristic diameters (Fig. 2):

$$D = D_s + 2L_{cs} + 2h_{cs} + 2h_m, \quad (1)$$

where

D – the diameter of the vacuum chamber, mm;

D_s – the characteristic diameter of the test object, mm. $D_{s\ min}$=141.4 mm; $D_{s\ nom}$=148 mm; $D_{s\ max}$=354 mm;

L_{cs} – the distance from the test object to the cryogenic shrouds, mm;

h_{cs} – the thickness of cryogenic shrouds, mm;

h_m – the distance from the cryogenic shrouds to the body of the vacuum chamber, mm.

The length of the cylindrical part of the vacuum chamber can be determined as the sum of the characteristic length:

$$L = L_s + 2L_{cs} + 2h_{cs} + 2h_m, \quad (2)$$

where

L – the length of the vacuum chamber, mm;

L_s – the characteristic length of the test object, mm. $L_{s\ min}$=248 mm; $L_{s\ nom}$=360 mm; $L_{s\ max}$=472 mm.

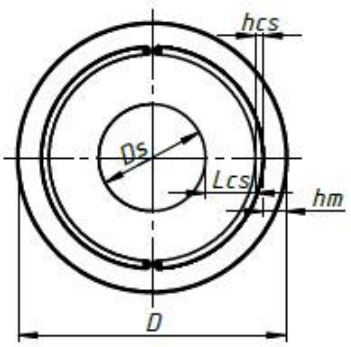

Fig. 2. Determination of vacuum chamber diameter size.

The main requirement of the standards [9], [10] for space environmental simulators is sufficient reliability of simulating real operating conditions, i.e., factors of outer space: 1) high vacuum; 2) zero reflection coefficient of electromagnetic radiation; 3) absence of convection and heat transfer through the thermal conductivity of the environment. High vacuum is understood as a state of gas in which collisions of gas molecules with the walls of the vessel prevail over the collision of gas molecules with each other. High vacuum is understood as a state of gas in which collisions of gas molecules with the walls of the vessel

prevail over the collision of gas molecules with each other.

As prescribed in standards [9], [10], the pressure in the vacuum chamber should not exceed 10^{-5} Torr and in any case ensure the achievement of the molecular regime of a gas flow in the vacuum chamber, characteristic of the space environment.

The criterion for determining the nature of the movement and interaction of gas molecules is the Knudsen criterion:

$$K_n = L_m / D_s, \quad (3)$$

where
L_m – the mean free path of gas molecules;
D_s – the characteristic size of the vacuum vessel.

$$L_m = \frac{1}{\pi d^2 n \sqrt{2}}, \quad (4)$$

where
d – the effective diameter of gas molecule, m;
n – the number of molecules (concentration) per unit volume.

We can use the Botzmann equation:

$$p \cdot V = n \cdot k \cdot T, \quad (5)$$

where
P – the gas pressure, Pa. According to the standards, the minimum pressure in the vacuum chamber is 10^{-5}Torr and for air pressure it will be 1.33 10^{-3} Pa;
k – the Boltzmann constant, 1.38 10^{-23}J/K;
T – the gas temperature, K. The temperature of the atmosphere in the test bench chamber is 20 ^{0}C or 293 ^{0}K.

The expression for determination the mean free path of an ideal gas molecule (4) can be rewritten:

$$L_m = \frac{kT}{\pi d^2 P \sqrt{2}}. \quad (6)$$

Since the initial atmosphere in the vacuum chamber of the test complex is air – the largest effective molecular diameter of a diatomic structure (N_2 and O_2) is about 3.5 10^{-10}m.

At a result, the length of the average free path of an air molecule as an ideal gas (6) will be:

$$L_m = (1.38 \cdot 10^{-23} \cdot 293)/(3.14 \cdot (3.5 \cdot 10^{-10})^2 \cdot 1.33 \cdot 10^{-3} \cdot 1.414) = 5.6\, m. \quad (7)$$

The estimate of the free path for an ideal gas can be taken as the maximum. Turning to a real gas, it is necessary to introduce correction for the non-ideal nature of the gas. First, with increasing temperature, the vibrational motions of molecules increase, which is practically demonstrated as an increase in the free path and is expressed as Sutherland correction for mean free path:

$$L_m = \frac{kT}{\left(1+\frac{C}{T}\right)\pi d^2 P \sqrt{2}}, \quad (8)$$

where
C is the Sutherland constant. The Sutherland constant value for air is 120.

Then, taking into account the correction, the free path for air at a temperature of 293 K and a pressure of 10^{-5} Torr will be 4.74 m.

In a real gas, gas molecules do not behave like rigid spheres, but rather attract each other at large distances and repel each other at smaller distances, which can be described using the Lennard-Jones potential where the radius of the molecule is rm=21/6σ~1.122 σ . Then the value of the free path of an air molecule at a pressure of 10^{-5} Torr and a temperature of 293 K will be 0.93 m.

This estimate of the mean free path can be taken as the most probable in assessing

the molecular regime of gas flow.

There is also a way to estimate the bridged path length from the assumption that the real gas is pseido-viscous. In this case, the mean free path of a molecule for a real gas is determined as follows:

$$L_m = \frac{\mu}{P}\sqrt{\frac{\pi RT}{2M}}, \quad (9)$$

where

μ – the viscosity, Pa s (μ=18.5 μPa s);

P – the pressure, Pa (1.33 10^{-3} Pa);

R – the universal gas constant, 8.31446261815324m^3PaK^1 mol^{-1};

T – the temperature, K (T=293K);

M – the molecular mass g/mol.

Then, when substituted in (9) we obtain L_m=0.27 m. This estimate can be discarded provided that a known molecular gas flow regime is ensured. Thus, it has been decided to accept for the vacuum calculation as the main estimate of the free path of a gas molecule in the vacuum chamber of the space environmental simulator at 0.93 m. From Eq. (8), taking into account the correction for the Lennard-Jones potential, we obtain a value of 0.186 m. Based on the obtained value of the mean free path and Eq. (3), let us determine the limitations of the overall dimensions of the vacuum chamber according to the Knudsen criterion to ensure the molecular regime of gas flow in the chamber for the main mode at maximum pressure (1 10^{-5} Torr):

$$D_s=L_m/K_n=0.93/10=0.093. \quad (10)$$

Thus, the characteristic size, i.e., the length of the shortest distance from the wall of the vacuum vessel to the test object should not exceed 0.093 m.

According to experimental data, during thermal cycling with imitation of the shadow side of a spacecraft in a space environmental simulation facility with liquid nitrogen cryogenic shrouds with a temperature of 90–95 ^{0}K, the temperature in the region close to the surface of the space of the spacecraft is close to 150 ^{0}K.

A verification calculation should be made to account for the effect of viscosity at low temperatures. For example, when the temperature of the atmosphere in the local volume of the vacuum chamber decreases from 293 ^{0}K to 150 ^{0}K, taking into account the value of the Sutherland coefficient (for air 120) and initial viscosity μ_0=18.5 μPa s, the viscosity of air at a temperature of 150 ^{0}K will be 14.1 μPa s, and, the free path of a molecule in accordance with (9) will be 0.08715 m.

Since the effect of a decrease in temperature on the mean free path of a molecule in viscosity is very significant, we will take this limitation into account. Then the characteristic size of the vacuum chamber should not exceed 0.0872- m.

Substituting into (1) the obtained values of the characteristic diameter of the test object and the double distance from the test object to the cryogenic shroud (7–9), taking the thickness of the cryogenic shields as 10 mm and the distance from the cryogenic shroud to the body of the vacuum chamber as 40 mm, we obtain the calculated diameters of the vacuum chamber:

$$D_{min} = 141.4 + 2 \cdot 87.2 + 2 \cdot 10 + 2 \cdot 40 = 415.8;$$

$$D_{nom} = 148 + 2 \cdot 87.2 + 2 \cdot 10 + 2 \cdot 40 = 422.4;$$

$$D_{max} = 354 + 2 \cdot 87.2 + 2 \cdot 10 + 2 \cdot 40 = 628.4.$$

Taking into account the technological tolerances, we initially take the calculated inner diameter of the prototype vacuum chamber: $D_{min} = 400^{+10}$ mm; $D_{nom} = 500^{+10}$ mm; $D_{max} = 800^{+10}$ mm.

Substituting into (2) the obtained values of the characteristic length, we obtain the total length of the cylindrical part of the vacuum chamber:

- for a diameter of 400 mm, the length of the cylindrical part is taken as 650 mm;
- for a diameter of 500 mm, the length of the cylindrical part is taken as 780 mm;
- for a diameter of 800 mm, the length of the cylindrical part is taken as 1300 mm.

Tests that can be done with the Prototype and its Operation Mode:

1. Thermal vacuum tests are the final certification, qualification or acceptance tests both in relation to individual parts, assemblies, assemblies and systems, and in relation to spacecraft as a whole. There are the following types of heat and vacuum tests:
   - thermostating;
   - thermal cycling;
   - thermobalance tests;
   - no-load vacuum tests – checking the performance of the thermal control system;
   - vacuum tests with partial load – with the inclusion of the thermal control system and partial activation of the on-board equipment for testing individual systems, assemblies and assemblies of the spacecraft;
   - vacuum tests with full load – with the inclusion of all systems of the spacecraft in the normal mode and full imitation of the payload operation program.

When carrying out thermal vacuum tests, it is necessary to ensure that the pressure in the vacuum chamber does not exceed $1x10^{-5}$ Torr ($1.33\ x10^{-3}$ Pa).

2. Pneumatic tests are acceptance tests for pneumatic and hydraulic systems of spacecraft and are preliminary tests in the test program for assemblies, assembly systems and spacecraft, in general. The following types of pneumatic tests are distinguished:
   - control of the tightness of the product by the mass spectrometric method;
   - analysis of the residual gases of the atmosphere of the vacuum chamber.

To carry out pneumatic tests, the accepted maximum pressure of $5x10^{-5}$ Torr ($7x10^{-3}$ Pa) is sufficient.

3. Electrical tests are acceptance tests for electrical systems of spacecraft and are preliminary tests in the testing program for assemblies, assembly systems and spacecraft, in general. There are the following types of electrical tests:
   - electrical tests with partial activation of on-board equipment for testing individual systems, assemblies and assemblies of the spacecraft;
   - electrical tests with the inclusion of all systems of the spacecraft in the normal mode and full simulation of the payload operation program.

Since voltages up to 400 V are usually used in on-board spacecraft equipment, the product of the distance between the conductors and the pressure should be less than 0.2. Spacecraft are characterised by a high packing density, and the distance between conductors can be up to 0.5 mm. In this case, to prevent ignition of the charge, the pressure in the vacuum chamber, the pressure should be less than $1x10^{-2}$ Torr (1.33 Pa). This condition is also satisfied by the maximum pressure in the vacuum chamber $5x10^{-5}$ Torr ($7x10^{-3}$ Pa).

4. Broad spectrum solar radiation tests. To carry out such a test, it is required to equip the simulator with a solar radiation simulator.
5. Test for the effects of ultraviolet radiation and radiation, which are part of the solar radiation spectrum. Test requires equipping the simulator with UV and X-ray solar radiation simulators.

6. Radiation tests under conditions of imitation of the impact of Van Allen radiation belts. To carry out such tests, it is required retrofitting of the test complex with sources of electrons, protons and helium nuclei (alpha particles) of the corresponding energy.
7. Degassing mode. In the degassing mode, parasitic gases and volatiles are removed from the surface and from the unpressurized volumes of the spacecraft.
8. Process thermostating mode. The pressure requirements for this type of test are similar to the requirements for thermal vacuum testing.

Estimated Gas Load and Vacuum Chamber Atmosphere Composition in Various Operating Modes

To analyse the gas load in different operating modes, it is necessary to assess the influence of various components on the overall picture of the gas load. The computational layout diagram of the test facility vacuum chamber is shown in Fig. 3.

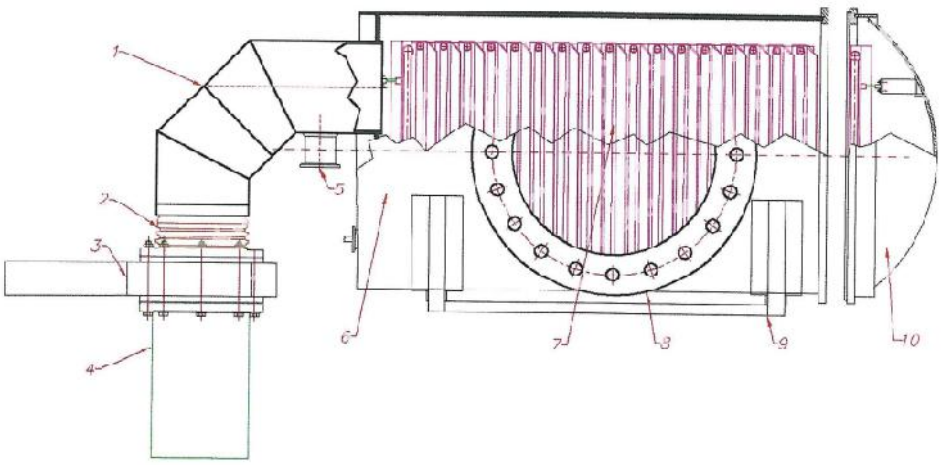

Fig. 3. Computational layout diagram of the Prototype vacuum chamber: (1) high-vacuum outlet; (2) vibration decoupling; (3) vacuum seal; (4) high-vacuum pump; (5) fitting for connecting the shutter of the fore line pump; (6) body of vacuum chamber; (7) cryogenic shroud; (8) optical feedthrough for inputting radiation from the Solar simulator; (9) lodgements and connections for camera mounting; (10) removable front cover.

During this step, operational pressure (10^{-5} mbar) and maximal gas load have been calculated. Then, the required pumping speed of fore vacuum pump (≥20 m^3/h) and turbomolecular pump (≥900 l/s) have been calculated. The required through diameter of the entire high-vacuum path of the vacuum pumping system has also been calculated (≥200 mm).

2.3. Thermophysical Calculation

One of the tasks to solve in the creation of facilities for simulating the conditions of outer space is a reliable imitation of the properties of outer space in terms of energy dissipation. A high vacuum also belongs to the properties of outer space; therefore, such heat transfer mechanisms as convection and heat transfer cannot be used. The

imitation of the process taking place in outer space will be reliable if only the radiation mechanisms of energy transfer are used. The problem of ensuring the reliability of simulating the dissipative capacity of outer space becomes especially important when testing modern leaky satellites with a passive thermal control system, which also include CubeSat.

This problem can be solved if the test object, placed inside the vacuum chamber of the space simulator, at a sufficient distance, is surrounded by surfaces absorbing thermal energy, having a temperature significantly closer to absolute zero than the temperature of the test object.

The basis of the project of the cryogenic system of the space simulator is its calculation. This calculation consists of a thermophysical part and a hydraulic part. The purpose of the thermophysical calculation is to prepare technical requirements for the elements of the Prototype cryogenic system.

Thermophysical calculation has been carried out using many results of vacuum calculation: information about the types of tests and operating modes of the Prototype, the nature of the gas load and pressure in the vacuum chamber, geometric characteristics of the vacuum chamber and the test object, dimensional characteristics of cryogenic screens, etc.

3. VIBRATION LOAD ANALYSES

According to posed requirements, the vacuum chamber system should be rigid enough to stand multiple transportation type loads. During transportation, mechanical systems are subjected to vibration loads caused and coming from different sources like engine, gearboxes, axels and other more unpredictable from road bumps and uneven parts of them. Most common transportation system to use for the vacuum chamber transportation has been taken to be road by truck or by railway.

In the beginning, the research on the mentioned subject has been conducted to obtain information about vibration levels, which appear during transportation on truck and train platforms. The designed system is intended to be transportable in intermodal environment. In intermodal environment, the transportation system can be subjected to vibration loads from transportation systems, which, in turn, come from rotating equipment, engines and uneven road bumps. According to research truck and railroad transportation, frequencies compose the range from 1 to about 120 Hz.

In this research, a system natural frequency range has been determined and analysed in comparison with frequencies caused by transportation, its impact on the system has been determined and solutions have been searched to reduce negative influence on the system for safe transportation.

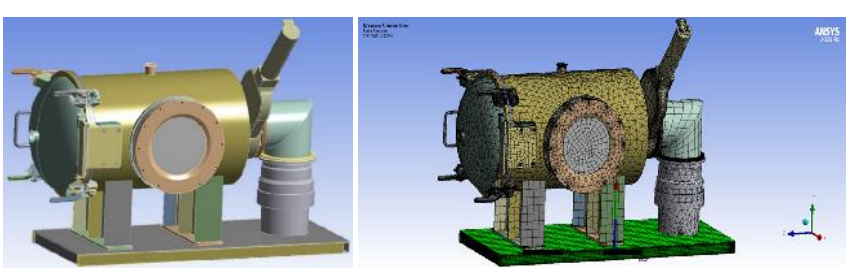

Fig. 4. Redesigned *Vacuum Chamber* construction.

From previous design steps and vibration load analyses, the construction has already been redesigned (integral base support part, chamber outtake part), providing positive results. Figure 4 illustrates the redesigned construction that will be subjected to vibration load analyses in the current design step. To determine construction load from the system inertial response forces and preload conditions for modal analyses, the Static Structural Analyses have been completed applying Standard Earth Gravity to the system. The system natural frequencies have been determined by modal analyses.

The vibration load influence from transportation is determined by Random Vibration Analyses. The system *CAD* model has been tested in *ANSYS* software environment. To check system on vibrational loads, it is necessary to complete simulation on loads in the following *ANSYS* modules [11]:

- *Static Structural Analyses* – during which it is prepared for a pre-stressed modal analysis [12]–[14];
- *Modal Analyses* – during which system natural frequencies are determined [15];
- *Random Vibration Analyses* – during which the structure response is determined under random loading [16]–[18].

The Vacuum Chamber weight is 349.35 kg, material is stainless steel, Young's Modulus of Elasticity – 1.93e+11 Pa, Poisson's Ratio – 0.31, density – 7750 kg/m^3, Tensile Yield Strength – 2.07e+08 Pa, Tensile Ultimate Strength – 5.86e+08 Pa.

The vibration loads are cyclic and repetitive, as well as vessels for use under pressure (in this case negative pressure), so for the current design the Vacuum Chamber structure is considered to be subjected to metal fatigue. Also, considering the aforementioned factor of safety for pressure vessels, the factor of safety value of 3.5 is taken for the current design.

3.1. The Static Structural Analyses

The system inertial response forces have been identified in Static Structural Analyses applying Standard Earth Gravity to the system. The results of Static Structural Analyses show the biggest directional deformation from structure inertial load at tank upper part, but values are not critical. Also strain energy concentrates in tube part with right angle; values are also not critical. Total deformation shows its concentration in part of structure where vacuum pump and shatter are mounted. Though the values are not critical, they can point to problems on those parts caused by vibration loads (Fig. 5).

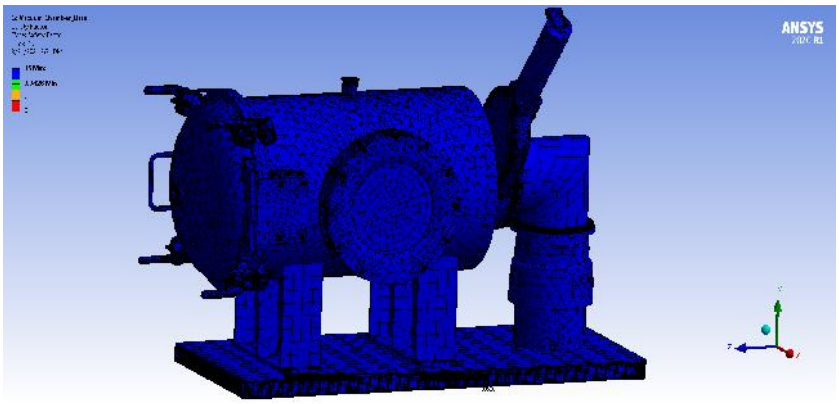

Fig. 5. The Vacuum Chamber analysed in *Static Structural* module.

Table 1. Summary of Static Structural Analysis Results

No.	Results	Minimum	Maximum	Units
1.	Normal Stress	-5.89E+06	2.05E+07	Pa
2.	Directional Deformation	-4.04E-05	1.05E-04	m
3.	Total Deformation	0	1.48E-03	m
4.	Equivalent Stress	0	2.67E+07	Pa
5.	Safety Factor	7.7428	7.7428	-

In the construction model for the *Static Structural Analyses*, the probe input has been made that shows the following reaction forces of -2.2042e-004 N, 3414.6 N, 3.0342e-004 N and 3414.6 N for X, Y and Z axis and total, respectively.

In Table 1, we can see the simulation results where the maximum stress is 20.5 MPa and maximum deformation is 0.105 mm in Z-axis direction and total deformation of 1.48 mm. In Table 2, we can see that the reaction force is 3414.6 N.

3.2. The Modal Analysis

Modal Analyses on twenty modes of natural frequencies have been determined, ranging from 6.6923 Hz to 286.41 Hz (Table 2). The most dangerous frequencies for the system that can lead to its disintegration are 126.22 Hz, 142.15 Hz, 200.52 Hz, and 247.48 Hz. Those dangerous frequency modes show strong shutter response that also affects the structure part with connection to chamber. Example of analysis results are depicted in Figs. 6 and 7.

Table 2. Summary of Modal Analysis Results

Mode	Frequency, Hz	Mode	Frequency, Hz
1.	6.6923	11.	142.15
2.	13.418	12.	169.59
3.	16.602	13.	185.24
4.	33.225	14.	186.6
5.	38.435	15.	200.52
6.	61.888	16.	210.37
7.	66.526	17.	217.88
8.	112.69	18.	233.17
9.	120.6	19.	247.48
10.	126.22	20.	286.41

If the applied force frequency is close to the construction system natural frequency, it dramatically affects the amplitude of oscillation which becomes very large and can lead to destruction of the construction system.

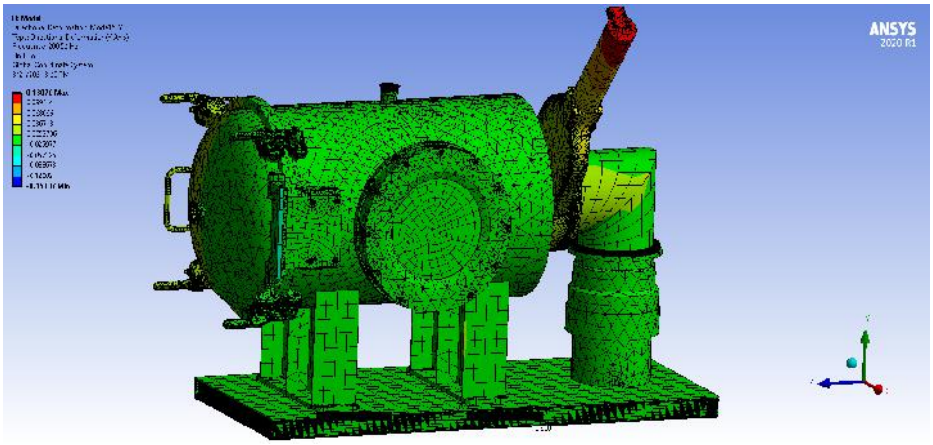

Fig. 6. Example of the Modal Analysis results.

The current study has determined twenty natural frequencies (Table 2) corresponding to the twenty normal frequencies. From the theoretical point of view, to determine system durability, it is necessary to take a wider range of frequencies that system will be subjected in real life with 1.5 probability that is to about 180 Hz. Thus, from Table 2, we can assume that the construction will show large amplitude oscillations when the exciting frequency is close to either of fourteen natural frequencies.

Results show that there is strong response in the X and Z axis directions. If it were on the support under chamber structure, it could be considered acceptable due to the material strength, but in this case the load direction could influence proper functioning of the vacuum pump and the gate valve. The system itself is strong enough to withstand those loads but as it refers to technically sophisticated assemblies that can influence their proper functioning, careful considerations should be taken, and it is very desirable to redesign that part of the system.

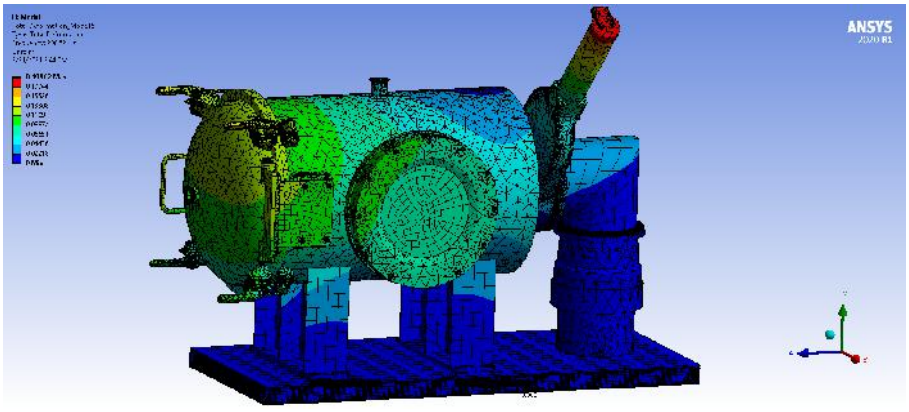

Fig. 7. Example of the Modal Analysis results.

From Table 3 we can see that modes that influence the Vacuum Chamber structure in the most severe way are 126.22 and 142.15 Hz, respectively.

Table 3. Summary of Modal Analysis Results

Results	Minimum	Maximum	Units	Reported Frequency (Hz)
Maximum Shear Elastic Strain	0	0.18285	m/m	6.6923
Normal Elastic Strain	-5.63E-02	7.56E-02	m/m	6.6923
Shear Elastic Strain	-5.80E-02	8.54E-02	m/m	6.6923
Maximum Shear Stress	0	1.35E+10	Pa	6.6923
Normal Stress	-1.85E+10	1.31E+10	Pa	6.6923
Shear Stress 2	-4.28E+09	6.29E+09	Pa	6.6923
Directional Deformation_Mode1	-5.30E-02	6.40E-03	m	6.6923
Directional Deformation_Mode3	-0.31106	4.59E-02	m	16.602
Directional Deformation_Mode10	-0.10989	7.74E-02	m	126.22
Directional Deformation_Mode11	-0.14774	9.94E-02	m	142.15
Directional Deformation_Mode14	-2.38E-02	2.60E-02	m	186.6
Directional Deformation_Mode17	-1.00E-02	1.07E-02	m	217.88

3.3. The Random Vibration Analysis

In Random Vibration Analyses, the system has been checked on possible damage types caused from vibration loads during transportation in the fourteen frequency modes that have been determined during Modal Analyses and correspond to a range of frequencies that can generate during transportation.

The construction has been tested on Sigma I stress level. The Sigma stress levels mean that these stress levels will occur 68.27 %, 95.45% and 99.73% of the time, respectively. 1-sigma, 2-sigma and 3-sigma levels are usually used, but these can be more, if necessary. For fatigue evaluation, 3-sigma stress level is essential. The stress levels from the Random Vibration are real, vary with time and have meaning. Similarly, the Von Mises stress is an indication of stress level severity at a point and its closeness to failure levels.

Analysis results also show strong structure response in Z axis and YZ component directions when vibration frequency is close to structure natural frequency. Result values do not exceed material (Stainless Steel) Yield Strength. The Factor of Safety should be considered (Figs. 8 and 9).

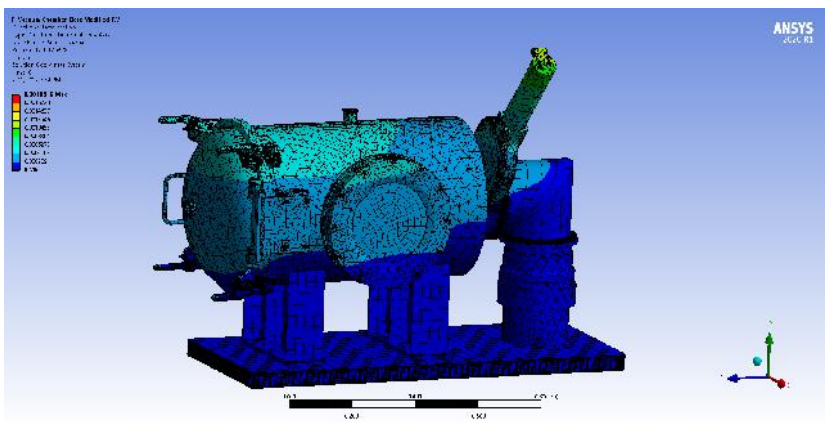

Fig. 8. Example of the Modal Analysis results.

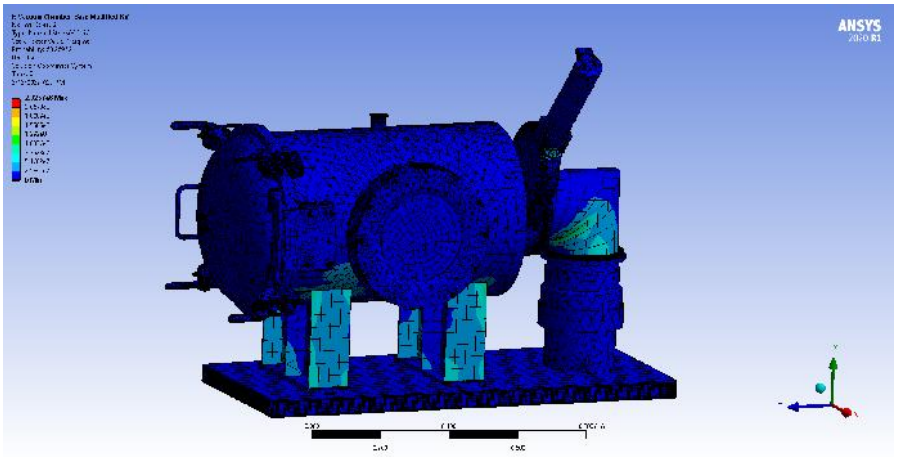

Fig. 9. Example of the Modal Analysis results.

Table 4. Summary of Random Vibration Analysis Results

Results	Minimum	Maximum	Units
Directional Deformation	0	6.85E-03	m
Normal Elastic Strain	0	1.30E-03	m/m
Shear Elastic Strain	0	8.89E-04	m/m
Normal Stress	0	3.44E+08	Pa
Shear Stress	0	6.55E+07	Pa
Equivalent Stress	0	2.026E+08	Pa
Directional Velocity	6.19E-02	0.94465	m/s
Directional Acceleration	39.392	711.16	m/s^2

In Table 4, we can see the simulation results where the maximum stress is 344 MPa and maximum deformation is 6.85 mm in Z-axis direction.

By completing the Vacuum Chamber analyses in ANSYS, it has been possible to identify deficiencies in the construction. The Static Structural Analyses have revealed that the safety factor is too high, it is equal to 7.74, which is more than twice of the necessary value defined in the beginning – 3.5. That can also be identified by Equivalent von-Mises Stress value (see Table 1) of 2.67e+07 Pa, which is only about 13 % of the allowable load. The system is too bulky. The changes can be made in support construction that will save same material and make construction lighter.

From the Modal Analyses and the Random Vibration Analyses, it can be seen that there is rather big vibration influence on the gate valve. As it is a sophisticated device and it can influence its proper functioning, consideration should be taken to change it for the other type of valve that is more appropriate to design situation (e.g., an electro-pneumatic angle valve).

Also, from the Random Vibration results, we can conclude that the Vacuum Chamber system is safe for transportation; however, originally the system has been designed as a transportable unit. If this is taken into account, then the safety factor of 3.5 should be also addressed to analy-

sis results from the Random Vibration that show Equivalent von-Mises Stress value of 2.026e+08 Pa (Table 4), which is about 98 % of the allowable load. If it is a safety factor, but as a design safety factor is determined to be 3.5, this points to the weakness of the construction. This indicates a too week design safety factor in case the system is subjected to transportation vibration. Thus, we need to assess the opportunity to redesign the Vacuum Chamber base construction, including some damping mechanisms. Since the Vacuum Chamber transportation state is not in its working state, but just only transfers to the point where actual work is to be completed, and that it will take very small part of its lifetime use, the damping system or mechanism should not be very complicated and raise overall price of the construction. It is suggested to use material at mounting place between the Vacuum Chamber and the transportation vehicle floor, with good damping properties.

Redesigned construction is depicted in Fig. 10.

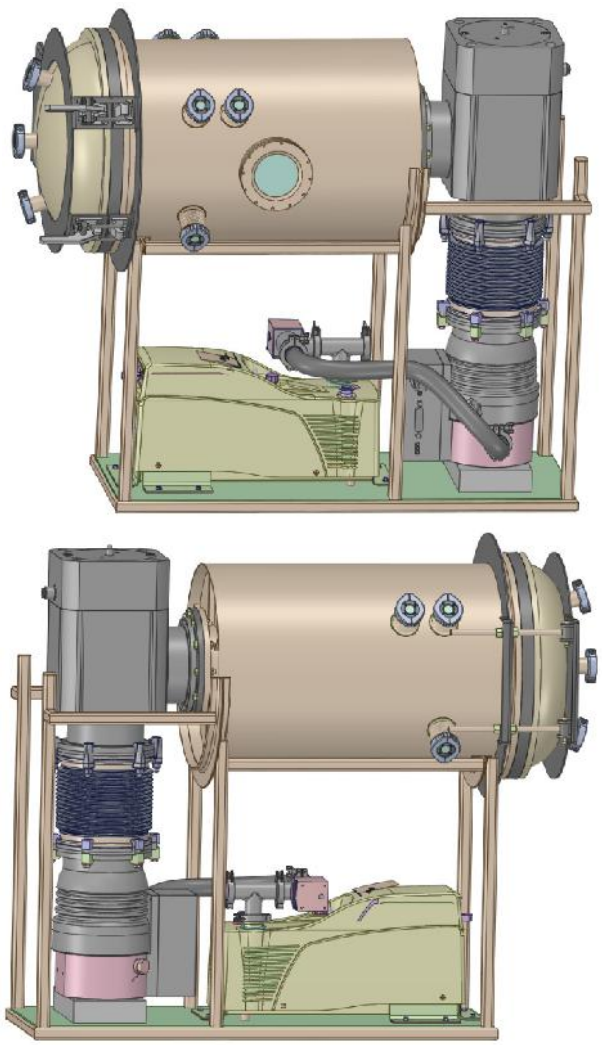

Fig. 10. Redesigned Vacuum Chamber (two-sided view).

According to the requirements, the Vacuum Chamber should be mounted on a vehicle and used as a mobile lab, it is also depicted in the mounted state that can be seen in Fig. 11. The Vacuum Chamber has been redesigned according to the obtained results. The initial design can be viewed in Fig. 4 (and also other from vibration simulation), the redesigned construction is depicted in Fig. 10.

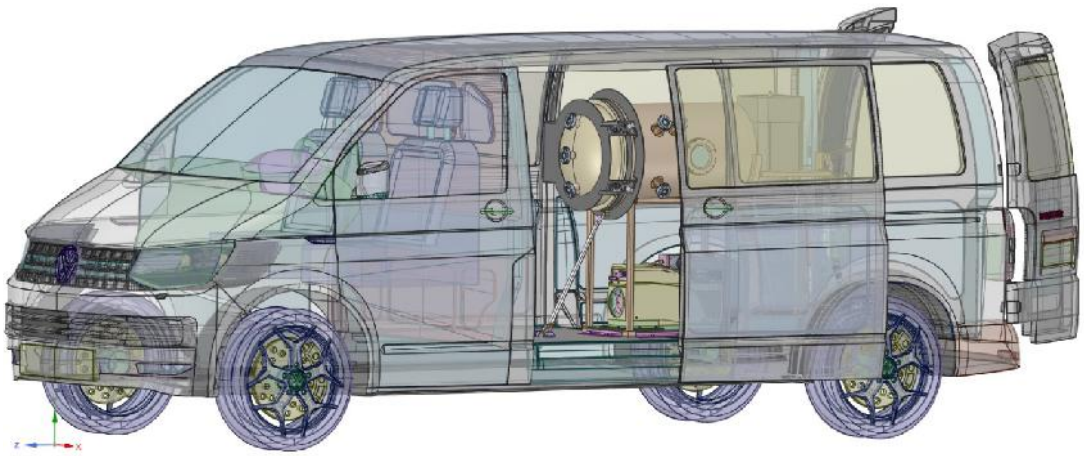

Fig. 11. Redesigned Vacuum Chamber mounted on a vehicle.

Completing the Modal Analyses and the Random Vibration Analyses, it has been observed that there is a rather big vibration influence on the gate valve (Figs. 6–8). As it is a sophisticated device and it can influence its proper functioning, consideration should be taken to change it for another type of valve more appropriate to the design situation. The gate valve has been changed to the electro-pneumatic angle valve.

4. CONCLUSIONS

The main stages of development of mobile thermal vacuum chamber to be used for testing CubeSats have been described in this article. The project for creating mobile testing facility for simulating the outer space environment has been implemented by Riga Technical University in cooperation with Cryogenic and Vacuum Systems Ltd.

Based on the developed technical requirements and the results of the Vacuum, Thermophysical calculation and Vibration Load Analyses and design documentation, technical specifications have been drawn up; the analysis of the market for materials and components has been performed; procurements of materials and components for vacuum and control systems manufacture have been provided, the supplied components incoming quality control has been performed; the prototype structural elements have been produced and/or purchased. During the further project implementation, all these elements have been sent to the assembly of the prototype, which has been then tested.

ACKNOWLEDGEMENTS

The research has been financed by the Aeronautics Institute of Riga Technical University project "Prototype Development of Transportable in Intermodal Traffic Mobile Space Testing Facility "Metamorphosis"" (Metamorphosis, project No. 1.1.1.1/18/A/133) budget.

REFERENCES

1. Union of Concerned Scientists. (n.d.). Available at https://www.ucsusa.org/
2. Irimex. (n.d.) Mobile Test Stand PV 1236. Available at https://www.irimex.ru/services/catalog/armatura/rubric_501/rubric_510/product_1651/
3. Prototype Development of Transportable in Intermodal Traffic Mobile Space Testing Facility "Metamorphosis" No. ERAF 1.1.1.1/18/A/133, Project implementers: Riga Technical University (Leading Partner), CRYOGENIC AND VACUUM SYSTEMS Ltd. 2019–2022. Available at https://www.rtu.lv/lv/universitate/ projekti/atvert?project_ number=4127
4. Cryogenic and Vacuum Systems. (n.d.) *Engineering Research Institute "Ventspils*
5. *International Radio Astronomy Centre" of Ventspils University of Applied Sciences*. Available at https://www.izm.gov.lv/sites/izm/files/latvian-entries1.pdf
6. ECSS Standard. (2012). *ECSS-E-ST-10-03C Space Engineering. Testing*. ECSS Secretariat ESA-ESTEC Requirements & Standards Division Noordwijk. The Netherlands.
7. NASA. (2013). *GSFC-STD-7000 General Environmental Verification Standard*. NASA Goddard Space Flight Center, Greenbelt, Maryland, USA.
8. ISO. (2016). *ISO 17851:2016 Space Systems – Space Environment Simulation for Material Tests – General Principles and Criteria.* International Standard Organization, Geneva, Switzerland.
9. Gutans, J., Mozga, N., Sestakovs, V., Kubulins, R., & Kleinhofs, M. (2023). Calculations of basic geometric parameters for Mobile Space Environment Simulation Facility "Metamorphosis". *Latvian Journal of Physics and Technical Sciences, 60* (3), 54–68.
10. ISO. (2007). *ISO 16528-1:2007 – Boilers and Pressure Vessels. – Part 1: Performance Requirements*. Available at https://www.iso.org/standard/41079.html
11. ISO. (2007). *ISO 16528-2:2007 – Boilers and Pressure Vessels – Part 2: Procedures for Fulfilling the Requirements of ISO 16528*-1. Available at https://www.iso.org/standard/41080.html
12. Glizde, N., Blumbergs, I., & Irbins, P. (2022). Structural Vibration Analysis of Intermodally Transportable Space Simulation Chamber. *Engineering for Rural Development*, 153–165. doi: 10.22616/ERDev.2022.21.TF048.
13. ANSYS. (2015). *Modeling Connections*. ANSYS, Inc.
14. ANSYS. (2016). *Best Practices for Contact Modeling using ANSYS.* ANSYS, Inc.
15. ANSYS. (2015). *Static Structural Analysis*. ANSYS, Inc. Available at https://www.clear.rice.edu/mech517/WB16/lectures_trainee/Mechanical_Intro_16.0_L07_Static.pdf
16. Matalevich, J. (2015). *Vibration and Modal Analysis Basics*. Jefferson Lab, Thomas Jefferson National Accelerator Facility. Available at https://indico.jlab.org/event/98/contributions/7450/attachments/6319/8367/6T_-_Vibration_and_Modal_Analysis_Basics.pdf

17. ANSYS. (2019). *Module 08: Random Vibration Analysis.* ANSYS, Inc. Available at https://innovationspace.ansys.com/product/random-vibration-analysis-using-ansys-mechanical/
18. Grishin, A. (2017). Estimating Structural Response to Random Vibration: Reaction Forces. *Phonex Analyses & Design Technologies.* Available at https://www.padtinc.com/2017/11/27/ansys-mechanical-random-vibration-reaction-forces/
19. ANSYS. (2015). *Results and Post-processing*. ANSYS, Inc. Available at http://static.sapucaia.ifsul.edu.br/professores/mauro/Curso%20Ansys/CFX_16_CD/lectures_trainee/CFX-Intro_16_L05_PostProcessing.pdf

sciendo

LATVIAN JOURNAL OF PHYSICS
AND TECHNICAL SCIENCES
2024, N 5

DOI: 10.2478/lpts-2024-0037

ADVANCED MAXIMUM POWER POINT TRACKING TECHNIQUE FOR PHOTOVOLTAIC REVERSE OSMOSIS SYSTEMS

A. G. E. M. I. Mowafy*, I. Steiks

Riga Technical University,
Faculty of Computer Science,
Information Technology and Energy,
Institute of Industrial Electronics,
Electrical Engineering and Energy
10 Zunda Embankment, Riga, LV-1048, LATVIA
*e-mail: Ahmed-Gamal-Ezzeldin-Mohamed-Ibrahim.Mowafy@edu.rtu.lv

The paper presents a novel control algorithm for a standalone Photovoltaic Reverse-Osmosis (PV-RO) system without a battery. It highlights the importance of tracking the maximum power tracking points in the photovoltaic panels. The development of new methods has become more urgent than before. The PV-RO system combines solar energy and reverse osmosis technology to provide reliable and sustainable access to clean drinking water in remote areas. Traditional PV-RO systems often require energy storage solutions such as batteries to maintain a constant water supply during periods of low solar irradiation. However, the integration of batteries adds complexity, cost, and environmental impact to the system. The paper presents the development of different MPPT techniques, which are better than traditional techniques (more accurate and faster). The paper also provides a comparison with the studied methods (P&O and Incremental Conductance) and the proposed one.

Keywords: *Batteryless system, control algorithm, desalination, MPPT, photovoltaics.*

1. INTRODUCTION

Access to clean drinking water is a fundamental necessity for human well-being and development. However, many regions around the world, particularly in remote and off-grid areas, still face significant challenges in securing a reliable and sustainable water supply. Traditional methods of water desalination and purification often rely on fossil fuels or grid-connected power sources, which may be unavailable, expensive, or environmentally detrimental in these regions [1]. To meet the energy needs of water treatment processes, the implementation of renewable energy sources, such as solar photovoltaic (PV) systems, appears as an appealing option.

In recent years, there has been a notable surge of interest in integrating PV systems with reverse osmosis (RO) technology. Photovoltaic-Reverse Osmosis (PV-RO) systems utilise solar energy to power the desalination or purification process, providing a clean and renewable energy source for water treatment. The intermittent nature of solar energy, however, makes it difficult to maintain a steady supply of water, particularly during times of low solar irradiation, like at night or in periods of cloudy conditions. To overcome this challenge, traditional PV-RO systems often integrate energy storage solutions, typically in the form of batteries, to store excess energy during sunny periods and use it during periods of low solar irradiation.

Although battery integration enables continuous water production, it introduces additional complexities, costs, and environmental concerns. Batteries require maintenance, have a limited lifespan, and contribute to the overall system's weight and footprint. Moreover, the production, use, and disposal of batteries involve environmental and sustainability challenges. Therefore, there is a need for alternative approaches that eliminate the reliance on batteries while maintaining reliable water production in standalone PV-RO systems.

This paper presents a modified control approach for a standalone PV-RO system without a battery. A feed water tank is used as an energy storage, aimed at addressing the challenges. The control algorithm intelligently manages the photovoltaic output power and optimises the operation of the RO unit based on real-time energy availability and water demand. By dynamically adjusting the water production rate and system operating parameters, the approach efficiently mitigates the characteristics of solar energy, and the water consumption demands, thereby obviating the necessity for energy storage solutions.

The goal of the paper is to assess how well the PV-RO system performs with the new control algorithm and compare it to traditional PV-RO systems with batteries. A comprehensive simulation model is developed to analyse the system's energy efficiency, water production reliability, and overall cost-effectiveness. The results of this study make a valuable contribution to the progress of standalone PV-RO systems, offering a practical and sustainable solution for water desalination and purification in remote and off-grid locations.

The paper is structured as follows: An overview of related research in PV-RO systems and control algorithms is provided in Section 2. The technique and simulation model utilised in this investigation are described in Section 3. The results and analysis of the suggested control algorithm are presented in Section 4. The work is concluded in Section 5 by summarising the major contributions and proposing potential directions for further study in this area.

2. LITERATURE REVIEW

The performance and energy efficiency of Photovoltaic-Reverse Osmosis systems are greatly improved by control algorithms. Researchers have focused on developing innovative control strategies to ensure reliable and sustainable water production without the need for energy storage solutions such as batteries [2]. The following provides an overview of key research areas and notable contributions in control algorithms for PV-RO systems.

By tracking the maximum power point (MPP) under fluctuating solar irradiation and temperature conditions, maximum power point tracking (MPPT) algorithms seek to maximise the power output from the photovoltaic array. PV-RO systems have used several MPPT approaches, including Perturb and Observe (P&O), Incremental Conductance, and Fuzzy Logic Control. The performance of the system is enhanced by these algorithms, enabling effective usage of solar energy [3].

Energy Management and Water Demand Control: Based on current energy availability and water demand, researchers have created control algorithms that dynamically regulate the energy distribution between the PV array and the RO unit. These algorithms optimise the water production rate, regulate system operating parameters, and prioritise water supply during periods of high demand or limited energy resources. Advanced control strategies, including model predictive control (MPC) and adaptive control, increase system reliability and efficiency [4].

Power Smoothing and Load Balancing: The solar energy nature can cause fluctuations in power supply to the RO unit [1]. Control algorithms have been developed to smooth out these fluctuations and maintain a stable water production rate. Techniques such as energy buffering, load shedding, and power scheduling algorithms have been employed to balance the energy supply and demand, ensuring continuous water supply while avoiding system instabilities [5].

Fault Detection and Diagnosis: Control algorithms are used to detect and diagnose faults or malfunctions in PV-RO systems. These algorithms analyse system parameters, sensor data, and performance indicators to identify deviations from normal operation. Fault detection algorithms, such as neural networks, fuzzy logic, and machine learning techniques, enable prompt identification of system failures, component degradation, or suboptimal operation, facilitating timely maintenance and improving system reliability [6].

Real-Time Optimisation and Decision-Making: Real-time optimisation algorithms are utilised to continuously adjust system parameters and optimise the operation of PV-RO systems [7]. These algorithms consider factors such as solar irradiance, water demand, energy efficiency, and system constraints to make informed decisions regarding power allocation, water production rates, and operating points. To improve system performance and reduce energy consumption, optimisation approaches such as genetic algorithms, particle swarm optimisation, and model-based optimisation have been used [8].

Control Hardware and Implementation: Research efforts have also focused on developing control hardware platforms, communication protocols, and control system architectures for PV-RO systems. Microcontroller, programmable logic controller, and supervisory control and data acquisition system integration are a few

examples of control hardware use. The implementation of control algorithms on hardware platforms enables real-time monitoring, control, and remote operation of PV-RO systems [9].

The research in control algorithms for PV-RO systems aims to optimise energy utilisation, improve water production reliability, and reduce system complexity. These efforts contribute to the development of sustainable water treatment solutions [10], especially in off-grid and remote areas. Future research may focus on advanced control techniques, integration with energy storage technologies, and system-level optimisation to further enhance the efficiency and scalability of PV-RO systems.

3. PV-RO PROPOSED SYSTEM

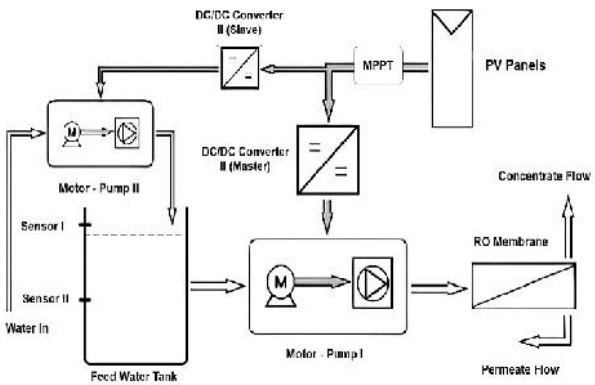

Fig. 1. Principle scheme of PV powered RO desalination.

In this study, we propose a new control algorithm that eliminates the need for a battery in the proposed PV-RO system while ensuring a continuous water supply. The algorithm intelligently manages the power output from the photovoltaic array and optimises the operation of the reverse osmosis unit based on real-time energy availability and water demand. By dynamically adjusting the water production rate and system operating parameters, the proposed control algorithm effectively balances the resulted fluctuations of the solar energy and the requirements of water consumption. This system as shown in Fig. 1 consists of photovoltaic panels, MPPT, DC-DC converters, motors, RO system, and water tank.

A thorough simulation model has been created to assess the performance of the PV-RO system using the new control algorithm. The simulation results show how well the suggested algorithm maintains a consistent water supply while maximising the use of the solar energy that is available. Compared to traditional PV-RO systems with batteries, the standalone system with the new control algorithm exhibits improved energy efficiency, reduced system complexity, and lower overall costs providing a practical and sustainable solution for water desalination and purification in off-grid and remote locations. The proposed control algorithm opens opportunities for widespread adoption of PV-RO systems, promoting and reducing reliance on fossil fuels and traditional energy sources, as well as access to clean drinking water.

4. THE PROPOSED CONTROL ALGORITHM

In contrast to other traditional search approaches, the proposed method operates on a distinct concept. The main goal of this method is to force the circuit current to operate at a value that is comparable to the MPP current value. This method can be used by figuring out predetermined current values that correspond to the highest possible power levels under various irradiation levels. To put it another way, a correlation of the maximum power and what are known as associated currents is found for different irradiation levels.

The average power will be estimated because of the continuous monitoring of the PV's current and voltage. The circuit's required current value will be decided by the computed power and the determined function. This value will be used as a benchmark against which the real value of the circuit's current will be continuously measured [5]. The Pl type control system will be used to regulate the endpoint of the operation's starting point by applying precise switching on the DC/DC converter, which serves as a mediator between the photovoltaic panel as the source of power and the load.

Using current adjustment, the system can track the necessary ideal current value, as shown in Fig. 3. The value of the power at the place where the line representing the load and current-voltage curve intersects can be used to calculate the circuit's normal operating point.

According to the power value, the system will compute a new value of current, Ireference2, and the PI controller's algorithm will push this value of current, which is determined as a function associated with the power, to identify the emphasis of the reference current, and equivalent power of the circuit [11].

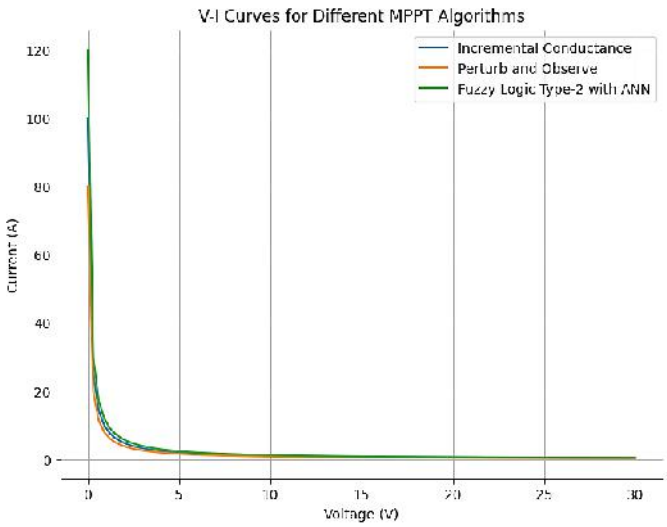

Fig. 3. V-I curve for different MPPT algorithms.

Since it does not rely on any search method, which always takes extra time to achieve the target operating point, the system may quickly follow the MPP in this way within a few milliseconds [4].

5. ALGORITHM SIMULATION

The duty cycle of the DC/DC converter, which serves as a middleman between the PVT module as a power supply and the load, will be adjusted by the Pl type controller before being used to control the location of the operation point.

The temperature will be measured, and the existing values will be updated, as shown within the modified simulation, to account for changes in temperature in three separate ranges (0–20, 21–35, and 36–55 °C). In a nutshell, each temperature variation range will have its own least-square computations for precise MPP determination.

6. CURVE FITTING

Building a curve, or ID mathematical function, that has the best fit to a set of data points while potentially considering constraints, is known as curve fitting. Two methods for fitting curves are interpolation, which requires a perfect fit to the data, or smoothing, which involves building a "smooth" function that roughly fits the data.

The simulation system shown in Fig. 4 has been initially created to track the MPP according to pushing the module values to match values from Table 1.

Table 1. Values of the Module at 25 °C

S(W/m2)	Pmax (W)	Imax (A)
1000	48.786	2.887
950	46.3626	2.8018
900	43.765	2.7441
850	41.4149	2.5827
800	38.9688	2.4341
750	36.6618	2.2357
700	34.2015	2.0905
650	31.6807	1.907
600	29.2523	1.7954
550	26.7682	1.6665
500	24.2757	1.4925
450	21.777	1.3386
400	19.2732	1.20132

The process of using a fitted curve outside the boundaries of the observed data is known as extrapolation. This process involves some uncertainty because the fitted curve may represent the construction process just as much as the observed data.

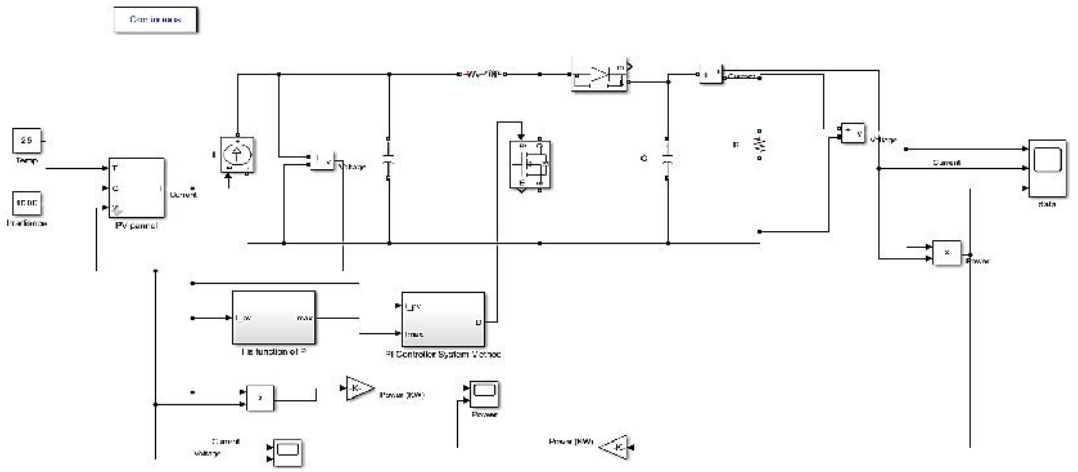

Fig. 4. The proposed method simulation.

The equation for 25 °C is as follows:

$$-7.846*10^{-5}\ P_{max}^{2} + 0.06616\ P_{max} + 0.06251. \quad (1)$$

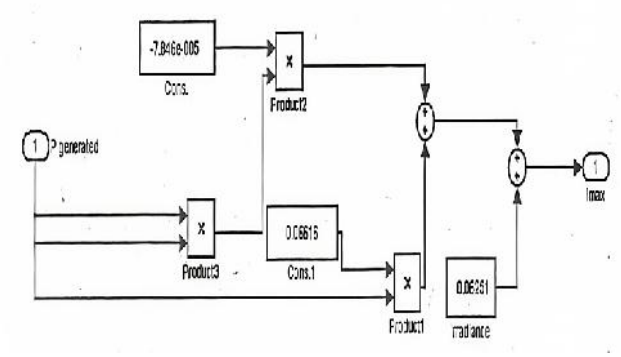

Fig. 5. Curve fitting equation subsystem.

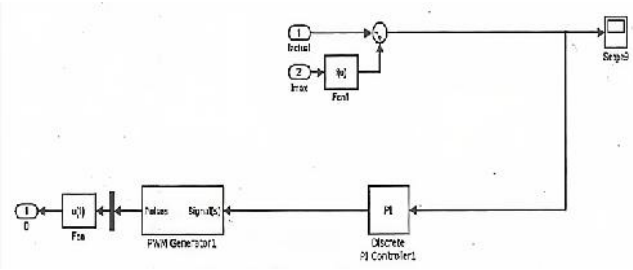

Fig. 6. PI controller subsystem.

The system is very fast in tracking the maximum power with every change of weather and load, and it may have a zero error since the locus of power changes with temperature. The maximum power point will change as well at the same irradiation level, because the PV panel currents are equal to the predetermined values of

optimum current values. If the temperature varies from the calculated values at STC (Standard Temperature Coefficient), some errors may occur. An installation of a temperature sensor can solve this issue.

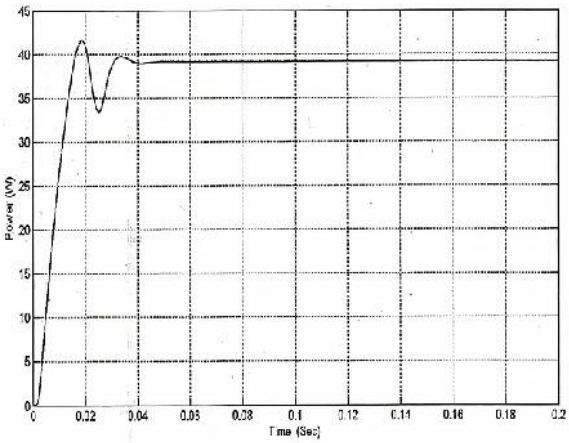

Fig. 7. The proposed method performance at 1000 W/m^2.

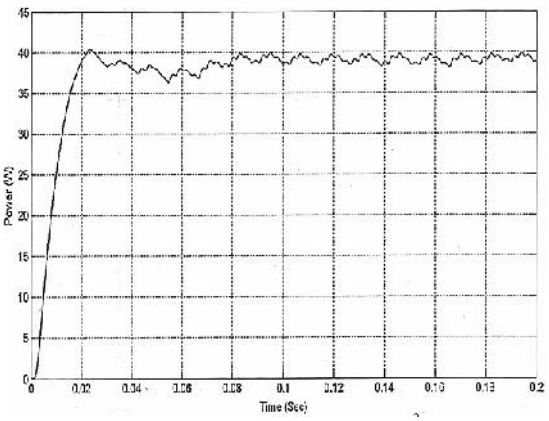

Fig. 8. IC method performance at 1000 W/m^2.

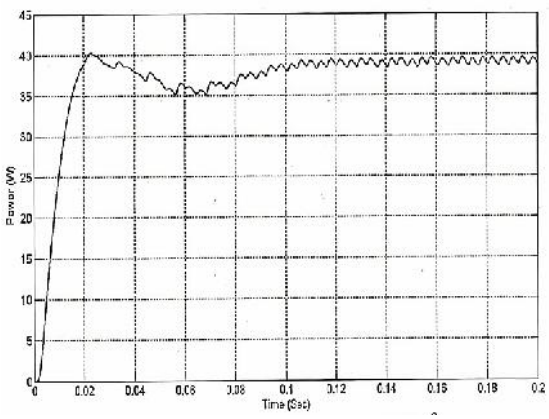

Fig. 9. PO method performance at 1000 W/m^2.

Table 2. Curve Fitting Equations

T(C)	Second degree curve	SS_E	RMSE
$0 \leq T < 20$	$4.65*10^{-5} P_{max}^2 + 0.0563 P_{max} + 0.0937$	0.005	0.023
$0 \leq T < 35$	$-7.846*10^{-5} P_{max}^2 + 0.06616 P_{max} + 0.06251$	0.012	0.035
$T \geq 35$	$-7.896*10^{-5} P_{max}^2 + 0.06616 P_{max} + 0.034$	0.004	0.022

The simulation results are given in detail and discussed with a suitable comparison with the Perturb and Observe and Incremental Conductance methods to validate the proposed method. Advantages and disadvantages of the proposed algorithm are also compared with the two traditional search methods (Table 4).

7. BEHAVIOUR OF MPPT ALGORITHM

It is difficult to evaluate MPPT behaviour, when there are two devices, and their interaction is involved in the measurement (PV module and MPPn). The actual readings of the current and voltage are measured by the PVG, but it is not easy to determine their maximum values, which vary with irradiance, temperature and other conditions.

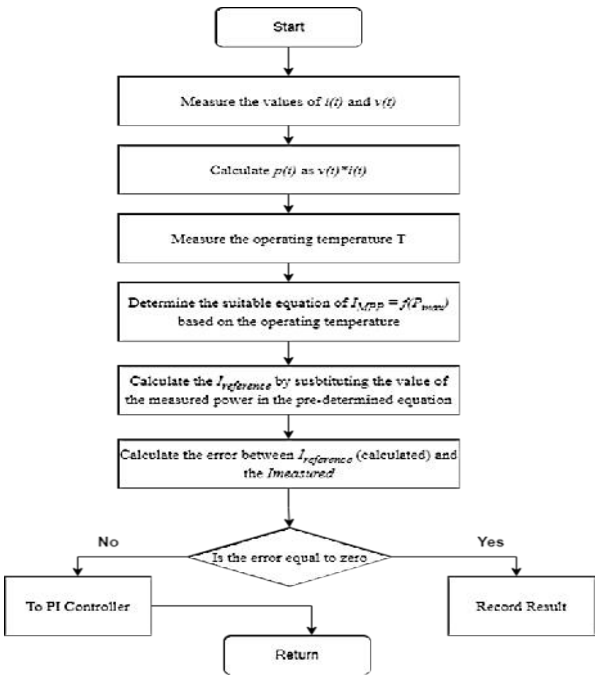

Fig. 10. Flow chart for the proposed algorithm.

The indices defining the behaviour of the MPPT algorithms shown in this section under static and dynamic modifications are provided as follows [12], [11]:

One of the straightforward and typical metrics used to show how closely the MPPT resembles the MPP is the a_{MPPT} during I_{MPP} [3]:

$$a_{mppt.p} = \frac{P}{p_{max}} * 100; \quad (1)$$

$$\text{or } \frac{v}{v_{max}} * 10 ; \quad (2)$$

$$\text{or } \frac{i}{i_{max}} * 100. \quad (3)$$

(η) The static efficiency index serves as a measure of how effectively actual PV power or energy compares to the available amount, and it is defined as follows (an example of accuracy in a specific scenario):

$$\eta_{mppt.p} = \frac{P}{p_{max}} * 100. \quad (4)$$

Let us consider that voltage or power can be used to define Eq. (1). Additionally, Eq. (6) provides the following definition for the relative tracking error (ε):

$$\varepsilon_{mppt} = P - P_{max} \text{ (Absolute)}; \quad (5)$$

$$\varepsilon_{mpp} = (\frac{P}{p_{max}} - 1) * 100 \text{ (Relative)}. \quad (6)$$

Additionally, to explain the MPPT's proximity to the maximum power point during a time period from 0 to tm, the energetic error of the MPPT ($\varepsilon_{mppt.E}$) and the energetic efficiency ($\eta_{mpp.E}$) are given as follows:

$$\eta_{mppt.E} = \frac{\int_0^{tm} P(t)d(t)}{\int_0^{tm} P_{max}(t)d(t)} * 100; \quad (7)$$

$$\varepsilon_{mppt.E} = (\frac{\int_0^{tm} P(t)d(t)}{\int_0^{tm} P_{max}(t)d(t)} - 1) * 100. \quad (8)$$

8. RESULTS

Table 3 shows the percentages of these indices for all the MPPT algorithms under study. It is notable that the proposed algorithm guarantees better values compared to the corresponding values of the conventional P&O and IC based MPPT algorithms.

Table 3. The Assessment of Algorithm Characteristics

Characteristics	Perturb and observe	Incremental conductance	Proposed
$a_{mppt.p}$	97.95	97.24	98.2
$\eta_{mppt.p}$	97.95	97.24	98.2
$\varepsilon_{mppt.p}$	2.45	2.96	1.95
$\eta_{mppt.E}$	86.0	88.0	91.0
$\varepsilon_{mppt.E}$	16.0	14.0	11.0

Table 4. Comparison of Advantages and Disadvantages

MPPT	Advantages	Disadvantages
P&O	1) Simple 2) Cheap 3) A few numbers of sensors needed 4) More common in usage	1) Not suitable in fast changes in weather 2) Slow response speed
IC	1) Simple 2) Faster than P&O method 3) Common in usage	1) More complex 2) More expensive
PI	1) Very fast response 2) Suitable for fast changes in irradiation and loads 3) Zero error is reached if the current generated equal Imax 4) High efficiency in dynamic weather changes	1) More complex 2) If the calculations of curve fitting have some errors, the efficiency of the system will decrease 3) Temperature dependency

According to the comparison between the proposed MPPT technique and the two previous methods (Table 4), it is concluded that the proposed technique is the best in tracking the MPP and can be used as a supplementary method.

9. CONCLUSION

An algorithm for tracking maximum power points under various operating conditions has been provided in this paper, and it is based on an investigation of the mathematical correlation between the maximum power points and the related currents. The performance, efficacy, benefits, and drawbacks of the proposed method in comparison to the traditional Perturb and Observe and Incremental Conductance methods have been highlighted by simulation results. The choice of the proper fitting relation between the maximum power and its associated current value is one of the primary contributions of this study. However, compared to other conventional MPPT approaches, the proposed method, nonetheless, has the drawbacks of being expensive and dependent on the photovoltaic.

It should be noted that the equations are greatly affected by two factors, i.e., how the system is able to achieve the MPP and how fast the system is able to achieve it. All the equations have been calculated over time from t=0 to t=tm. Energetic efficiency enhances, if the module can work very closely to the required MPP and is too fast.

Notably, the proposed approach promises the improved results compared to the values of the traditional P&O and IC-based MPPT techniques and can be utilised as an additional approach.

REFERENCES

1. Richards, S., Capao, D.P.S., & Schafer, A.I. (2008). Renewable Energy Powered Membrane Technology. 2. The Effect of Energy Fluctuations on Performance of a Photovoltaic Hybrid Membrane System. *Environ. Sci. Technol., 42*, 4563–4569.
2. Al-Suleimani, Z., & Nair, V.R. (2000). Desalination by Solar-Powered Reverse Osmosis in a Remote Area of the Sultanate of Oman. *Desalination, 65,* 367–80.
3. Tzen, E. (2005). *Successful Desalination: RES Plants Worldwide.* Hammamet, Tunisia: Centre for Renewable Energy Sources.
4. Herold, D., & Neskakis, A. (2001). A Small PV-Driven Reverse Osmosis Desalination Plant on the Island of Gran Canaria. *Desalination, 137*, 285–292.
5. Gocht, W., Sommerfeld, A., Rautenbach, R., Melin, T., Eilers, L., Neskakis, A., … & Muhaidat, A. (1998). *Decentralized Desalination of Brackish Water by a Directly Coupled Reverse-Osmosis-Photovoltaic-System – A Pilot Plant Study in Jordan. Renew Energy, 14* (1–4), 287–292.
6. Joyce, A., Lourerio, D., Rodrigues, C., & Castro, S. (2001). Small Reverse Osmosis Units Using PV Systems for Water Purification in Rural Areas. *Desalination, 137,* 39–44.
7. Miranda, M.S., & Infield, D.A. (2002). Wind-Powered Seawater Reverse-Osmosis System without Batteries. *Desalination, 153*, 9–16.
8. AlMadani, H.M.N. (2003). Water Desalination by Solar Powered Electrodialysis Process. *Renew Energy, 28* (12), 1915–1924.

9. Scrivani, A. (2005). Energy Management and DSM Techniques for a PV-Diesel Powered Sea Water Reverse Osmosis Desalination Plant in Ginostra, Sicily. *Desalination, 183*, 63–72.
10. Thomson, M. (2003). *Reverse-Osmosis Desalination of Seawater Powered by Photovoltaics without Batteries*. PhD dissertation. UK: Loughborough University.
11. Wunderlich, H. (2016). *Model-Based Development of a Maximum Power Point Tracker for Solar Generators of Solar-Driven Electro-Vehicles Using MATLAB/ Simulink* [Modellbasierte Entwicklung eines Maximum Power Point Trackers für Solargeneratoren solarenergiebetriebener Elektrofahrzeuge mittels MATLAB/ Simulink]. Master Thesis. University Koblenz-Landau, Germany.
12. Richards, S.B., & Schafer, A.I. (2003). Photovoltaic-Powered Desalination System for Remote Australian Communities. *Renew Energy, 28,* 2013–2022.

sciendo

LATVIAN JOURNAL OF PHYSICS
AND TECHNICAL SCIENCES
2024, N 5

DOI: 10.2478/lpts-2024-0038

OPTIMISATION OF ELECTROSPINNING PARAMETERS FOR HIGH-STRENGTH ORIENTED PAN NANOFIBRE MATS

J. V. Sanchaniya*, V. Rana, S. R. Vejanand

Riga Technical University,
Faculty of Civil and Mechanical Engineering,
Institute of Mechanics and Mechanical Engineering,
6B Kipsala Str., Riga, LV-1048, LATVIA
*e-mail: jaymin.sanchaniya@rtu.lv

This study explores the optimisation of electrospinning parameters to enhance the strength and orientation of polyacrylonitrile (PAN) nanofibre mats, which are pivotal in filtration applications and other areas requiring high-strength, uniformly distributed nanofibres. The focus is on the electrospinning process, particularly on a rotating drum collector, which is instrumental in determining the morphology of nanofibres. Key process variables, including the distance between the collector and the syringe, feed rate, applied voltage, and polymer concentration, have been meticulously examined to understand their influence on the physical properties of PAN nanofibres. Our findings indicate that parameters such as voltage, collector-to-syringe distance, and drum rotation speed (RPM) significantly impact the mechanical performance of the nanofibre mats. The optimised electrospinning conditions produced PAN nanofibre mats with tensile strengths ranging from 1.61 MPa to 21.78 MPa, demonstrating a notable improvement in strength due to controlled fluid dynamics and expulsion of polymer solution during the process.

Keywords*: Aligned nanofibres, optimisation, PAN nanofibre mat, response surface methodology.*

1. INTRODUCTION

Electrospinning emerges as a cost-effective methodology for the production of nanofibres [1]. This technique involves the collection of nanofibres in various ways; for instance, when using a flat plate collector, the structure of the nanofibres tends to be randomly orientated. In contrast, in drum-rotating collectors, nanofibres are typically characterised by higher strength and are orientated in a singular direction [2].

Polyacrylonitrile (PAN) nanofibres have garnered considerable attention due to their wide range of applications in filtration [3], biomedical engineering, drug delivery [4], scaffolding, nanocomposites [5], [6], antibacterial textiles [7]–[9], and protective clothing [10]. In such applications, the strength of the nanofibres is of paramount importance [11].

The collection of nanofibres on a flat plate collector presents fewer variables to control, as the fibres are deposited randomly, necessitating primarily the prevention of bead formation during electrospinning. However, the scenario changes significantly when nanofibres are electrospun onto a rotating drum. A critical variable in this context is the speed of the rotating drum, along with other parameters that become consequential in relation to the drum speed. The electrospun nanofibres may be collected in a semisolid or solid state, necessitating the avoidance of bead formation.

Thus, it becomes imperative to optimise the electrospinning process parameters to achieve high-strength nanofibre mats when collected on a rotating drum.

Table 1 encapsulates a summary of the literature concerning various methods of collecting nanofibres and the parameters used there. A notable variation in the choice of parameters is evident from this summary.

Table 1. Summary of Electrospun Process Parameters in the Fabrication of Nanofibre Mats

Collector type	Voltage (kV)	Distance (cm)	Speed of RD RPM	Applications	Reference
drum	15	10	400	Wastewater filtration	[12]
drum	18	15	600	Textile composites reinforced	[13]
drum	16	18	800	Gas toluene removal	[14]
drum	16	15	500	Air gap membrane distillation	[15]
roller	12	20	500	Super-capacitors	[16]
roller	15	18	800	Hybrid nanofibre filtration	[17]
drum	20	10	1000	Future high-power target	[18]
drum	17	15	1200	Wound healing	[19]
roller	16	10	1000	Super-capacitor	[20]
drum	15	20	400	Dust removal	[21]
roller	20	20	400	Non-crimping laminated	[22]
drum	18	18	1200	Textile composites reinforced	[23]
drum	20	20	1200	Annealed PAN nanofibres	[11]
drum	16	15	600	Battery	[24]
drum	20	10,15,20	500	Carbonized nanofibres	[25]
roller	14	20	800	Creating novel metal	[26]
drum	17.5	10	400	Orientated ferromagnetic Ni1-xFex nanofibres	[27]
roller	10	15	800	Enantioselective material	[28]
drum	11	10	600	Junction-free electrospun nanofibre network	[29]
drum	20	10	1000	Anti-adhesion barrier	[30]
drum	18	10, 20	1200	Food packaging	[31]

The literature reveals a broad spectrum of process parameters that are used for the production of nanofibres. In this context, six process parameters have been identified as critical in the electrospinning process. Among these, three are considered primary due to their significant impact on the quality of the nanofibres: voltage, collector drum distance, and drum speed. Secondary parameters – flow rate, needle gauge, and

polymer viscosity (wt / wt % of PAN polymer) – are considered interrelated. Alterations in the needle gauge or polymer viscosity are likely to proportionally impact the flow rate, thus warranting a holistic approach to optimising these parameters. Therefore, in this research, these secondary parameters are kept constant to maintain consistency and focus on the primary variables.

2. MATERIALS AND METHODOLOGY

The present study focusses on elucidating the effects of the electrospinning process parameters on the ultimate tensile strength of orientated PAN nanofibres. The PAN nanofibres were synthesised using PAN powder and N,N-dimethylformamide (DMF). Polyacrylonitrile (average molecular weight: 150,000; CAS number: 25014-41-9) and N,N-dimethylformamide (DMF; ACS reagent (solvent), purity ≥ 99.8%; CAS number: 68-12-2) were obtained from Sigma-Aldrich Chemicals (Merck KGaA, Darmstadt, Germany).

The electrospinning procedure was conducted according to the methodology previously established by the authors [11], [23], [32]. Figure 1 delineates the schematic of the electrospinning setup used in the Mechanics and Biotextile Research Laboratory at Riga Technical University.

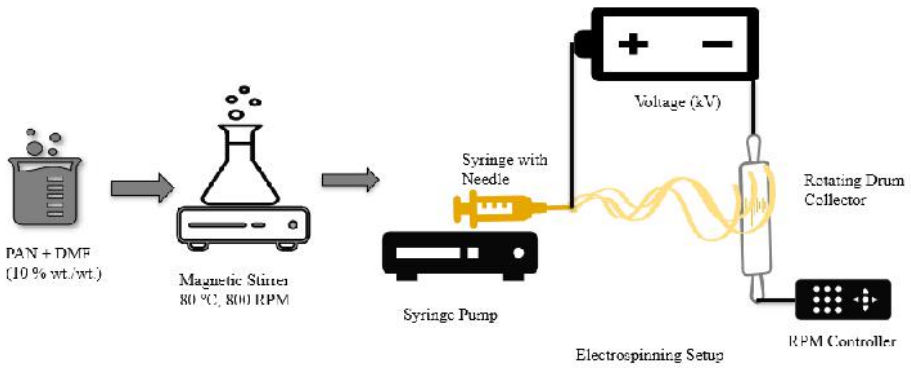

Fig. 1. Schematic diagram of the electrospinning setup.

For the optimisation of the process parameters, the range was chosen based on a comprehensive review of the literature as detailed in Table 1.

Table 1. Range of Process Parameters for Optimisation

Process Parameters	Parameters Used
Solution	PAN + N, N- Dimethylformamide
Polymer, wt/wt % (constant)	10
Needle size ml/hr (constant)	18
Flow rate, ml/hr (constant)	1
Tip to collector distance, cm	5, 10 and 15
Applied voltage, kV	15, 17.5, 20
Speed of rotating drum, RPM	400, 800, 1200

Response surface method (RSM) was employed as a statistical technique to optimise the electrospinning process, which involves analysing the relationship between the electrospinning settings and the ultimate tensile strength. Response surface methodology was implemented using the Design Expert software, and experiments were designed using the Box-Behnken. Seventeen experiments were designed as summarised in Table 2.

Table 2. Design of Experiments

No.	PAN + DMF (10 % wt./wt.)	Needle Size (Ga)	Flow rate of the solution (ml/hr)	Voltage (kV)	Needle to drum distance (cm)	Speed of rotating drum (RPM)
1.	10	18	1	15	15	400
2.	10	18	1	20	15	1200
3.	10	18	1	17.5	10	1200
4.	10	18	1	17.5	15	800
5.	10	18	1	15	10	800
6.	10	18	1	17.5	15	800
7.	10	18	1	17.5	15	800
8.	10	18	1	17.5	5	1200
9.	10	18	1	20	5	800
10.	10	18	1	17.5	15	800
11.	10	18	1	20	10	800
12.	10	18	1	20	15	400
13.	10	18	1	15	15	1200
14.	10	18	1	17.5	15	800
15.	10	18	1	17.5	10	400
16.	10	18	1	17.5	5	400
17.	10	18	1	15	5	800

All PAN nanofibre mats were produced as detailed in Table 2. Tensile properties were measured using a Mecmesin Multi-Test 2.5-i tensile testing machine equipped with a 25-N sensor (PPT Group UK Ltd., t/a Mecmesin, Newton House, Spring Copse Business Park, Slinfold, UK). The samples were conditioned and stored at room temperature according to ISO 139:1973 “Standard Environments for Conditioning and Testing”, specifying a temperature of 21 ± 1 °C, a relative humidity of 60 %, and an atmospheric pressure of 760 mm Hg. The sample dimensions were in accordance with ASTM D882-18, with a size of 50 mm × 10 mm (length × width). Five measurements were made to determine the tensile properties. The thickness of the nanofibre mats was gauged using a digital micrometre (range: 0–25 mm; Digimatic micrometre, MDC-25PX, code No. 293-240-30, serial No. 71912410, Mitutoyo, Japan). A 50 mm × 40 mm paper template with an inside cut of 30 mm × 20 mm was used. Both ends of the sample were adhered to the paper template using double-sided thin scotch tape (3M Scotch Magic Tape (Matte Finish) 3/4” × 36-yard Desk Dispenser refills). After attaching the paper and sample to the tensile testing apparatus, the sides of the paper template were excised with scissors, as defined in the methodology [5], [11].

3. RESULTS AND DISCUSSION

The experimental results of 17 distinct runs were meticulously analysed. The findings pertaining to the ultimate tensile strength (UTS) of the electrospun PAN nanofibres are summarised in Table 3.

Table 3. Summary of the Ultimate Tensile Test Results Obtained from the 17 Experiments

	Factor 1	Factor 2	Factor 3	Response 1
	A: Voltage	B: Distance	C: Rotation	UTS
Run	kV	cm	RPM	MPa
1	15	15	400	1.74
2	20	15	1200	2.5
3	17.5	10	1200	5.11
4	17.5	15	800	2.55
5	15	10	800	4.64
6	17.5	15	800	2.45
7	17.5	15	800	2.64
8	17.5	5	1200	17.45
9	20	5	800	10.36
10	17.5	10	800	2.56
11	20	10	800	8.63
12	20	15	400	3.04
13	15	15	1200	1.61
14	17.5	15	800	2.53
15	17.5	10	400	16.08
16	17.5	5	400	21.78
17	15	5	800	15.92

The evaluation of the primary responses reveals significant insights. For example, when the voltage was set at 15 kV with a 15 cm distance between the collector and spinneret and a drum rotation speed of 400 RPM, the UTS of the PAN nanofibre mat was 1.74 MPa. On the contrary, increasing the voltage to 20 kV and the drum rotation speed to 1200 RPM, while maintaining a constant distance of 15 cm, resulted in an increase in UTS to 2.50 MPa. This suggests that adjustments in voltage and drum rotation, with a fixed distance, can significantly enhance the tensile strength of PAN nanofibre mats.

Further analysis shows that when the voltage was maintained at 17.50 kV but the distance and rotation were adjusted, there was a noticeable impact on the tensile strength. For example, a 50 % reduction in tensile strength was observed when the distance was increased to 16 cm with a reduction in the drum rotation speed to 400 RPM. This indicates that the rotational speed of the drum has a more pronounced impact on the tensile strength of the PAN nanofibre mats compared to the distance parameter.

In the eighth experimental run, the tensile strength was maximised to 17.45 MPa with a decrease in distance and an increase in voltage, alongside an optimised drum rotation speed. Furthermore, in the 15th,

16th and 17th runs, as the applied voltage was increased and the distance and drum rotation speed were decreased, the tensile strength improved markedly, reaching 21.78 MPa. These findings underscore the significant influence of voltage and rotation speed on the tensile strength of PAN nanofibre mats.

The statistical analysis of the model is presented in Table 4, which provides information on the sequential p-value, the lack of fit p-value, adjusted R^2, and predicted R^2.

Table 4. Statistical Summary of the Model

Source	Sequential p-value	Lack of fit p-value	Adjusted R^2	Predicted R^2	
Linear	**<0.0001**	**<0.0001**	**0.7868**	**0.9602**	**Suggested**
2FI	0.5831	<0.0001	0.7709	0.2798	
Quadratic	0.1067	<0.0001	0.8559	-2.0389	
Cubic	<0.0001		0.9999		**Aliased**

Figure 2 represents a model that integrates the coded factors of the electrospinning process and the corresponding results obtained from the experimental runs. This figure is crucial in visualising the relationships and interactions between the various parameters studied and their impact on the ultimate tensile strength of the PAN nanofibres. It likely includes graphical representations, such as response surface plots or contour plots that depict how changes in the electrospinning parameters influence the tensile strength. This visual aid is instrumental in providing a clear and concise understanding of the experimental data and facilitating the interpretation of complex relationships between the coded factors and the resultant properties of the nanofibre mats.

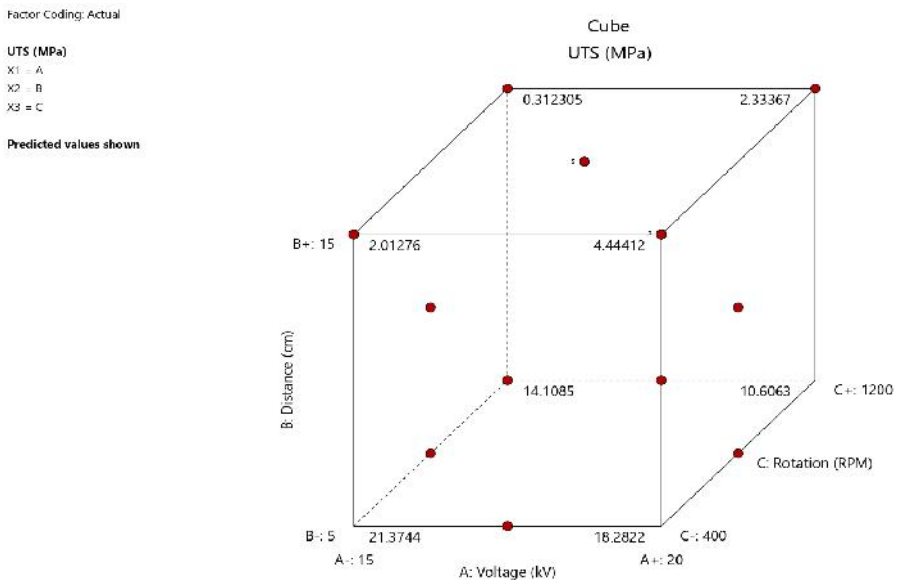

Fig. 2. Model representation with coded factors and obtained results.

Visual analysis (Fig. 3) suggests that optimising the distance between the collector and spinneret, coupled with a reduction in applied voltage, leads to an increase in the surface area of the PAN nanofibre mats. The optimal values were identified at a voltage of 15 kV and 5 cm distance, signifying that the optimisation of distance and voltage enhances the tensile strength of the PAN nanofibre mats.

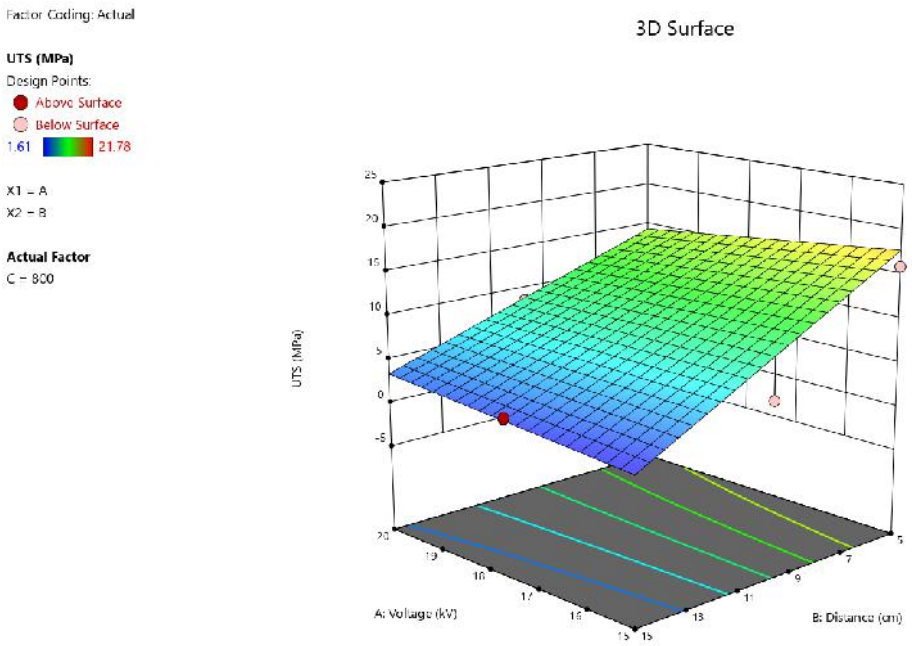

Fig. 3. 3-D visual of the influence of changes in electrospinning parameters on the surface area and ultimate tensile strength of PAN nanofibre mats.

Figure 4 illustrates the intricate relationship between the applied voltage, the distance of the rotating drum collector, and their collective impact on both the desirability function and the ultimate tensile strength (UTS) of the PAN nanofibres. This figure is pivotal for understanding how variations in these key electrospinning parameters influence the final quality and mechanical properties of nanofibre mats.

The graph presents a combination of response surfaces or line graphs, detailing how adjustments in voltage and drum distance affect desirability – a metric often used to gauge the overall effectiveness and efficiency of process parameters – and the UTS, a critical measure of the strength of the nanofibre mat. Such a visual representation is invaluable for identifying optimal parameter settings and understanding the trade-offs involved in the electrospinning process. It helps clarify the point at which the parameters converge to maximise both the desirability and the mechanical strength of the nanofibres, thus providing a comprehensive overview of the parameter optimisation process.

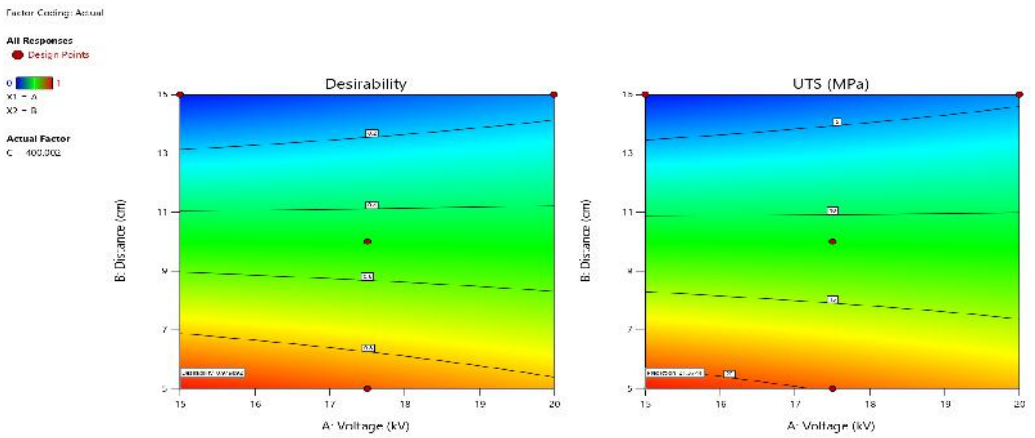

Fig. 4. Graphical representation of desirability and UTS in relation to voltage and rotating drum collector distance.

Equation (1) integrates the coded factors such as voltage (coded A), distance between the spinneret and the collector (coded as B), and the speed of the rotating drum (coded as C). It could be a polynomial or another form of regression equation that best fits the experimental data. The coefficients in the equation represent the influence of each factor and their interactions on the UTS of the nanofibre mats.

$$UTS = +9.18 -0.2677\ A -6.91\ B -2.34\ C +1.38\ AB – 0.1025\ AC +1.39\ BC. \quad (1)$$

Equation (1) represents the final predictive model in terms of coded factors. This equation represents the quantified relationship between the coded electrospinning parameters and their collective impact on the ultimate tensile strength of the PAN nanofibres, serving as a crucial predictive tool for determining optimal process conditions.

CONCLUSIONS

The comprehensive study undertaken to optimise the electrospinning parameters for the production of high-strength-orientated polyacrylonitrile nanofibre mats has yielded pivotal insights, underpinned by the extensive analysis of experimental data. The meticulous exploration of key parameters – applied voltage, distance between collector and spinneret, and the speed of the rotating drum – has culminated in a nuanced understanding of their collective impact on the ultimate tensile strength (UTS) of the nanofibres.

Figures 3 and 4 serve as crucial visual aids, illustrating the intricate relationship between these electrospinning parameters and the mechanical properties of the PAN nanofibre mats. Figure 3 effectively maps the interaction of the coded factors with the UTS, providing a clear graphical representation of the complex interplay at work. Figure 4 further delves into the correlation between the parameters and both desirability and UTS, offering a comprehensive view

of how varying the electrospinning parameters can optimise the quality and strength.

Equation (1), the final predictive model derived from the study, encapsulates the essence of these findings. It quantitatively represents the relationship between the coded electrospinning parameters and the UTS of the PAN nanofibres. This equation stands as a testament to the robust statistical methodology employed, offering a predictive tool that can significantly streamline the process of determining optimal electrospinning conditions.

In conclusion, this research not only enhances our understanding of the electrospinning process, but also significantly contributes to the field of nanotechnology, particularly in the production of high-strength nanofibre mats. The optimisation of electrospinning parameters, as delineated in this study, has crucial implications for various industrial applications where the strength and quality of nanofibre mats are paramount. The insights gained from this research hold a substantial value for future academic and industrial pursuits, paving the way for advancements in nanofibre fabrication technology and its myriad applications.

ACKNOWLEDGEMENTS

The research has been supported by the Doctoral Grant programme of Riga Technical University.

REFERENCES

1. Nauman, S., Lubineau, G., & Alharbi, H. F. (2021). Post Processing Strategies for the Enhancement of Mechanical Properties of Enms (Electrospun Nanofibrous Membranes): A Review. *Membranes (Basel)*, *11* (1), 1–38. doi: 10.3390/membranes11010039
2. Sanchaniya, J. V., Kanukuntla, S.-P., Simon, S., & Gerina-Ancane, A. (2022). Analysis of Mechanical Properties of Composite Nanofibres Constructed on Rotating Drum and Collector Plate. *21st Int. Sci. Conf. Eng. Rural Dev. Proc.*, *21*, 737–744. doi: 10.22616/erdev.2022.21.tf227
3. Roche, R., & Yalcinkaya, F. (2019). Electrospun Polyacrylonitrile Nanofibrous Membranes for Point-of-Use Water and Air Cleaning. *ChemistryOpen*, *8* (1), 97–103. doi: 10.1002/open.201800267
4. Homaeigohar, S., & Boccaccini, A. R. (2020). Antibacterial Biohybrid Nanofibres for Wound Dressings. *Acta Biomater.*, *107*, 25–49. doi: 10.1016/j.actbio.2020.02.022
5. Lasenko, I., Sanchraniya, J. V., Kanukuntla, S. P., Ladani, Y., Viluma-Gudmona, A., Kononova, O., … & Selga, T. (2023). The Mechanical Properties of Nanocomposites Reinforced with PA6 Electrospun Nanofibres. *Polymers (Basel)*, *15* (3), 673. doi: 10.3390/polym15030673
6. Sanchaniya, J. V., Lasenko, I., Vijayan, V., Smogor, H., Gobins, V., Kobeissi, A., & Goljandin, D. (2024). A Novel Method to Enhance the Mechanical Properties of Polyacrylonitrile Nanofibre Mats: An Experimental and Numerical Investigation. *Polymers (Basel).*, *16* (7), 992. doi: 10.3390/polym16070992
7. Sanchaniya, J. V., Kanukuntla, S. P., Modappathi, P., & Macanovskis, A. (2022). Mechanical Behaviour Numerical Investigation of Composite Structure, Consisting of Polymeric Nanocomposite Mat and Textile. *21st Int. Sci. Conf. Eng. Rural Dev. Proc.*, *21*, 720–726. doi: 10.22616/erdev.2022.21.tf225

8. Grauda, D., Butkauskas, D., Vyšniauskiene, R., Rančeliene, V., Krasņevska, N., Miķelsone, A., … & Ļašenko, I. (2023). Establishment of Biotesting System to Study Features of Innovative Multifunctional Biotextile. *Proc. Latv. Acad. Sci. Sect. B Nat. Exact, Appl. Sci.*, *77*, (3–4), 186–192. doi: 10.2478/prolas-2023-0026
9. Asfand, N., & Daukantiene, V. (2023). Study of the Tensile and Bending Stiffness Behavior of Antistatic and Antibacterial Knitted Fabrics. *Fibres Text. East. Eur.*, *31* (3), 1–9. doi: 10.2478/ftee-2023-0026
10. Gorji, M., Bagherzadeh, R. & Fashandi, H. (2017). Electrospun Nanofibres in Protective Clothing. *Electrospun Nanofibers. Woodhead Publishing Series in Textiles*, 571–598. doi: 10.1016/B978-0-08-100907-9.00021-0
11. Sanchaniya, J. V., Lasenko, I., Kanukuntala, S. P., Smogor, H., Viluma-Gudmona, A., Krasnikovs, A., … & Gobins, V. (2023). Mechanical and thermal characteristics of annealed-oriented PAN nanofibres. *Polymers (Basel)*, *15* (15), 3287. doi: doi.org/10.3390/polym15153287
12. Zhao, Y., Hussain, A., Liu, Y., Yang, Z., Zhao, T., Bamanu, B., & Su, D. (2023). Electrospinning Micro-Nanofibres Immobilized Aerobic Denitrifying Bacteria for Efficient Nitrogen Removal in Wastewater. *J. Environ. Manage.*, *343*, 118230. doi: 10.1016/j.jenvman.2023.118230
13. Amini, S., Kandeh, S. H., Ebrahimzadeh, H., & Khodayari, P. (2023). Electrospun Composite Nanofibres Modified with Silver Nanoparticles for Extraction of Trace Heavy Metals from Water and Rice Samples: An Highly Efficient and Reproducible Sorbent. *Food Chem.*, *420*, 136122. doi: 10.1016/j.foodchem.2023.136122
14. Gezmis-Yavuz, E., Cansoy, C. E., & Koseoglu-Imer, D. Y. (2023). Fabrication of Mixed Matrix Nanofibres with Electrospraying and Electrospinning Techniques and their Application to Gas Toluene Removal. *J. Environ. Chem. Eng.*, *11* (3), 110067. doi: 10.1016/j.jece.2023.110067
15. Eryildiz, B., Ozbey-Unal, B., Menceloglu, Y. Z., Keskinler, B., & Koyuncu, I. (2023). Development of Robust Superhydrophobic PFA/TMI/PVDF Membrane by Electrospinning/Electrospraying Techniques for Air Gap Membrane Distillation. *J. Appl. Polym. Sci.*, *140* (12). doi: 10.1002/app.53635
16. Wang, Y., Qu, Q., Cui, J., Lu, T., Li, F., Zhang, M., … & Huang, C. (2021). Design and Fabrication of Cellulose Derived Free-Standing Carbon Nanofibre Membranes for High Performance Supercapacitors, *Carbohydr. Polym. Technol. Appl.*, *2*, 100117. doi: 10.1016/j.carpta.2021.100117
17. Guo, Q., Li, Y., Wei, X.-Y., Zheng, L.-W., Li, Z.-Q., Zhang, K.-G., & Yuan, C.-G. (2021). Electrospun Metal-Organic Frameworks Hybrid Nanofibre Membrane for Efficient Removal of As(III) and As(V) from Water. *Ecotoxicol. Environ. Saf.*, *228*, 112990, 2021, doi: 10.1016/j.ecoenv.2021.112990
18. Elnabawy, E., Farag, M., Soliman, A., Mahmoud, K., Shehata, N., Nair, R., … & Hassanin, A. H. (2021). Solution Blow Spinning of Piezoelectric Nanofibre Mat for Detecting Mechanical and Acoustic Signals. *J. Appl. Polym. Sci.*, *138* (45), 1–10. doi: 10.1002/app.51322
19. Bidhar, S., Goss, V., Chen, W.-Y., Stanishevsky, A., Li, M., Kuksenko, S., … & Zwaska, R. (2021). Production and Qualification of an Electrospun Ceramic Nanofibre Material as a Candidate Future High Power Target. *Phys. Rev. Accel. Beams*, *24* (12), 123001. doi: 10.1103/PhysRevAccelBeams.24.123001
20. Trabelsi, M., Mamun, A., Klocker, M., Brockhagen, B., Kinzel, F., Kapanadze, D., & Sabantina, L. (2021). Polyacrylonitrile (PAN) Nanofibre Mats for Mushroom Mycelium Growth Investigations and Formation of Mycelium-Reinforced Nanocomposites. *J. Eng. Fiber. Fabr.*, *16*, doi: 10.1177/15589250211037982
21. Mamuk, A. E., Koçak, Ç., Aslan, S., & Bal Altuntaş, D. (2022). Electrochemical Properties of Coumarin 500 Encapsulated in a Liquid Crystal Guided Electrospun Fiber Core and Their Supercapacitor Application. *ACS Appl. Energy Mater.*, *5* (10), 12078–12089. doi: 10.1021/acsaem.2c01287

22. Bauer, L., Brandstater, L., Letmate, M., Palachandran, M., Wadehn, F. O., Wolfschmidt, C., … & Ehrmann, A. (2022). Electrospinning for the Modification of 3D Objects for the Potential Use in Tissue Engineering. *Technologies*, *10* (3), 66. doi: 10.3390/technologies10030066
23. Sanchaniya, J. V., Lasenko, I., Kanukuntla, S. P., Mannodi, A., Viluma-Gudmona, A., & Gobins, V. (2023). Preparation and Characterization of Non-Crimping Laminated Textile Composites Reinforced with Electrospun Nanofibres. *Nanomaterials*, *13* (13), 1949. doi: 10.3390/nano13131949
24. Lee, J. P., Choi, S., Cho, S., Song, W. J., & Park, S. (2021). Fabrication of Carbon Nanofibres Decorated with Various Kinds of Metal Oxides for Battery Applications. *Energies*, *14* (5), 1–10. doi: 10.3390/en14051353
25. Jin, s., Yu, J., Zheng, Y., Wang, W. Y., Xin, B., & Kan, C. W. (2018). Preparation and characterization of electrospun PAN/PSA carbonized nanofibres: Experiment and simulation study. *Nanomaterials*, *8* (10). doi: 10.3390/nano8100821
26. Sabantina, L., Rodriguez-Cano, M. A., Klocker, M., Garcia-Mateos, F. J., Ternero-Hidalgo, J. J., Mamun, A., … & Ehrmann, A. (2018). Fixing PAN Nanofibre Mats during Stabilization for Carbonization and Creating Novel Metal/Carbon Composites. *Polymers (Basel)*, *10* (7), 735. doi: 10.3390/polym10070735
27. Bhugra, V. S., Williams, G. V. M., Chong, S. V., & Nann, T. (2020). Electrospun, Oriented, Ferromagnetic Ni1-xFex Nanofibres. *Front. Chem.*, *8*, 1–8. doi: 10.3389/fchem.2020.00047
28. Yang, J., Li, P., Zhao, B., Pan, K., & Deng, J. (2020). Electrospinning Chiral Fluorescent Nanofibres from Helical Polyacetylene: Preparation and Enantioselective Recognition Ability. *Nanoscale Adv.*, *2* (3), 1301–1308. doi: 10.1039/d0na00127a
29. Kim, G. H., Woo, H., Kim, S., An, T., & Lim, G. (2020). Highly-Robust, Solution-Processed Flexible Transparent Electrodes with a Junction-Free Electrospun Nanofibre Network. *RSC Adv.*, *10* (17), 9940–9948. doi: 10.1039/c9ra10278g
30. Baek, S., Park, H., Park, Y., Kang, H., & Lee, D. (2020). Development of a Lidocaine-Loaded Alginate/CMC/PEO Electrospun Nanofibre Film and Application as an Anti-Adhesion Barrier. *Polymers (Basel)*, 12 (3). doi: 10.3390/polym12030618
31. Zhu, W., Zhang, D., Liu, X., Ma, T., He, J., Dong, Q., … & Cai, J. (2022). Improving the Hydrophobicity and Mechanical Properties of Starch Nanofibrous Films by Electrospinning and Cross-Linking for Food Packaging Applications. *LWT*, *169*, 114005. doi: 10.1016/j.lwt.2022.114005
32. Sanchaniya, J. V., Lasenko, I., Gobins, V., & Kobeissi, A. (2024). A Finite Element Method for Determining the Mechanical Properties of Electrospun Nanofibrous Mats. *Polym.*, *16* (6), 852. doi: 10.3390/polym16060852

sciendo

LATVIAN JOURNAL OF PHYSICS
AND TECHNICAL SCIENCES
2024, N 5

DOI: 10.2478/lpts-2024-0039

MODELLING Π-SHAPED CONCENTRATING OPTICS FOR LCPV SOLAR CELLS USING FRESNEL LENS

A. Kapparova, S. Orynbassar, G. Dosymbetova*, D. Almen,
E. Yershov, A. Saymbetov, M. Nurgaliyev, N. Algazin,
A. Sharipbay, D. Zhastalapova

Faculty of Physics and Technology,
Al-Farabi Kazakh National University,
71 Al-Farabi, Almaty 050040, KAZAKHSTAN
*e-mail: dossymbetova.g@kaznu.kz

Most concentrating optics do not show good performance at higher incidence angles and have low acceptance angles and, therefore, they require a high-accuracy solar tracking system, which is costly. In this study, by detailed investigation of optics of the proposed Π-shaped concentrating optics, it was found that system remained high in terms of optical efficiency and its concentration ratio at certain higher incidence angles. During the work, ray path through the concentrating optics, width of the light spot at different incidence angles were calculated. Optical efficiency, geometrical concentration ratio, concentration ratio at different incidence angles were found by the results of COMSOL Multiphysics calculations. It was found that the system had a high optical efficiency of approximately 95% and its concentration ratio of 3x-5x was at the range of ±0-20 degrees of incidence angle, and it could reduce the work of a solar tracking system. As well, an increase in the optical efficiency could be seen from 0 to 5 degrees of the incidence angle and an increase in the concentration ratio could be seen from 0 to 12 degrees of the incidence angle in terms of the reflective mirrors which helped redirect the rays to the solar cells. Optical systems with such a high incidence angle could reduce the performance of the solar tracker system, and it reduced the overall cost and energy consumption of the LCPV.

Keywords: *Concentration ratio, Fresnel lens, incidence angles, light spot, optical efficiency, ray path, Π-shaped.*

1. INTRODUCTION

These days humanity consumes the energy generated by the sources, which pollute the environment. In one year, humanity consumes the energy, which the Sun delivers to Earth in 1 hour [1]. It means we are losing the clean, free energy; therefore, improving performance of solar power plants is a significant task. Researchers demonstrated that the substantial and readily available solar energy can effectively meet global energy demands [2], [3]. Nowadays, the amount of energy generated by solar panels is not sufficient, and electrical efficiency of the systems are lower. There are some opportunities to improve the performance of solar batteries. Using high-efficient solar cells, for example, multi-junction solar cells, is one of the ways to tackle the issue, but these kinds of solar cells are expensive, and their manufacturing process is complex [4]–[6].

Another way to improve the performance of generating electrical energy of photovoltaic systems is increasing the incident solar radiation power [7], [8]. The output power of solar batteries depends on the power of solar radiation; therefore, by increasing the incident solar radiation, it is possible to increase the generated power. Those systems are called concentrating photovoltaics (CPV). In CPV systems, by using more affordable mirrors and/or lenses, the overall cost can be reduced [9]. The paper [10] proved that average power output increased considerably using mirrors. Another work [11] improved the maximum power of the solar panel by 17 % by using flat mirrors. Currently, the CPV systems use different types of concentrating optics and depending on their performance they are classified as follows: LCPV (>10 suns) [12], MCPV (10–100 suns) [13], HCPV (100–2000 suns) [14] and UHCPV (42 000 suns) [15]. LCPV and MCPV systems have basic design principles even though their concentration ratio is lower [16]. HCPV systems usually consist of expensive high-efficiency small solar cells and several optical elements [17]. Even though HCPV systems have a high concentration ratio, the installation and maintenance are complex and cost-ineffective.

Among the CPV systems, LCPV modules are particularly appealing, since they can be affordable due to lowered active material usage, a Balance-Of-the-System cost potentially equivalent to that of standard fixed panels [18]. In the mid-2000s, Low Concentration Photovoltaics (LCPVs) made their market debut. LCPVs are still continuing their significance in the solar technology landscape compared to traditional flat PV panels [19]. Another benefit of LCPV systems is that they can be used with cheap commercial silicon solar cells, which help reduce the overall cost of the system. The paper [20] compared poly-crystalline and mono-crystalline silicon solar cells under low concentration ratio and concluded that poly-crystalline PV module was more efficient than mono-crystalline under LCPV conditions despite of the mono-Si PV module having higher performance compared to poly-Si PV module under STC.

The most common and widely adopted concentrating optics are the Fresnel lens and parabolic mirror [21]. Types of concentrating optics for LCPV systems are compound parabolic concentrators (CPCs) and planar flat concentrators or V-Trough, ACPC, parabolic concentrator, cylindrical troughs, linear Fresnel reflectors [22]. The

work [23] could increase the output power of CPV using CPC by 3 times compared to a non-concentrating system. Another work was performed using commercially available monocrystalline silicon photovoltaic solar cells and compound parabolic concentrator, and a concentration ratio of the LCPV reached 7x and the CPC optical efficiency was 55 % [24]. The work [25] examined a reflective asymmetrical compound parabolic concentrator (ACPC), which increased the power concentration ratio of the panel by 2.1 times compared to a similar non-concentrating panel. Another common type of LCPV and MCPV optics is linear Fresnel lenses, which can reach 5x concentration ratio but they are usually used with solar/thermal systems [26].

The Fresnel lens can be a linear Fresnel lens or a point focus Fresnel lens which is just called Fresnel lens [27]. Plastic Fresnel lenses are the most common primary optical concentrator since they are light-weight and capable of elevating the density of solar energy and possess advantages of compactness, simplicity in manufacture, and relative cheapness [28].

The work [29] designed a Fresnel lens which had a shorter focal length, the acceptance angle of the whole system was between 0.6 to 0.8°, and the optical efficiency obtained by simulations was between 80 to 90 %. To increase the acceptance angle and uniform distribution of sunlight, secondary optical concentrators were used [30].

Authors [31] compared two secondary optics: the CPC and the cone for Fresnel lens-based concentrator. Even though the concentration ratio increased in the case of the cone, the concentration was higher in the case of the CPC when the angle of incidence increased. Fresnel lens was used as a primary optical element with four types of secondary optics to get wider acceptance angle in [32]. As it can be seen, the abovementioned Fresnel lens-based concentrating photovoltaics have a low acceptance angle because they have a 1000x concentration ratio. Only high-efficiency small multi-junction solar cells can resist high concentrations. However, such solar cells are multiple times more expensive than single-junction silicon solar cells.

The work [33] showed that when using Fresnel lens as a concentrator for polycrystalline solar cells, it is possible to get an LCPV system, which can generate 27 % more energy than a non-concentrated silicon solar cell. The work [34] investigated different Fresnel lens designs and determined their optical efficiency. The design of the concentrating optics and the distance between solar cell and lens has a significant impact on the optical efficiency, which is defined as how efficiently the photons of the incoming radiation are transferred to the solar cell [35].

Point-focusing lenses need to operate in normal incidence, which means the incidence angle is zero, with accurate sun tracking in order to work properly [36]. A solar tracker is an essential component of CPV with such types of concentrators. The solar tracker can increase the PV panel energy by approximately 33 % [37]. However, a substantial amount of energy is consumed by solar tracking systems [38], [39]. Subsequently, when using point-focus Fresnel lenses, there has to be additional optics which helps obtain angled rays and increase the acceptance angle. The acceptance angle or optical tolerance for parabolic dishes and Fresnel lenses, without additional optics can be expected to be very low ±0.5 or less [40], [41]. If rays hit the solar cell with a greater angle than the acceptance angle, then non-uniform irradiance distribution may occur. To tackle the issue, a secondary optical element is added

to the CPV system [42]. The secondary optical element helps not only to improve the uniformity of irradiance distribution, but also increases the sunlight tracking tolerance [43]. The paper [39] shows that the tracking tolerance of the dome-shaped non-imaging Fresnel lens held efficiencies of 90 % up to an incident angle of 0.4°, then dropped to 80 % at 0.6° and then to 10 % at 1°. It means, when using Fresnel lenses as a concentrator, an accurate solar tracking system is necessary. However, the solar tracking systems consume more electrical energy to move the whole system [44]–[46]. Reducing the work of solar tracking is usually done by designing optical systems which redirect the sunlight to the solar cell. Therefore, it is important to design Fresnel based concentrators with additional optics.

The aim of the study is to design an optical system which can help reduce the work of solar tracking systems and increase the acceptance angle while not reducing the optical concentration ratio. In this work, we added reflective surfaces perpendicularly on the edges of Fresnel lens which helped redirect the inclined rays to the solar cell at higher incidence angles. The proposed optical system is called Π-shaped concentrating optical system. The novelty of the work is a mathematical model of Π-shaped concentrating optics and widening the incidence angle of a Fresnel lens-based LCPV with polycrystalline silicon solar cells. The proposed Π-shaped LCPV with nine polycrystalline solar cells showed good performance at higher incidence angles. Moreover, using cheap silicon solar cells and simple, affordable optics can reduce the system cost. As the system which has a wide incidence angle, it can simplify the work of a solar tracking system and reduce its power consumption.

2. MATHEMATICAL MODEL OF Π-SHAPED CONCENTRATING OPTICAL SYSTEM

A Fresnel lens is one of the types of optical lens, and it consists of a series of concentric grooves. The grooves allow the lens to achieve the same optical efficiency as a traditional lens but it is much thinner and lighter. It is known that the Fresnel lens concentrates the sunlight to one point, but if the polycrystalline solar cell is placed at the exact focus of the lens, the light does not cover the entire surface of the solar cell. Due to the concentrated light on the centre of the solar cell, it leads to a hot spot and the failure of the solar cell. Therefore, it is necessary to place the lens at such a distance that it evenly and completely covers the surface of the solar cell (Fig. 1a). However, placing the photocell at the focus of the Fresnel lens does not eliminate the need for a solar tracking system. Therefore, nine solar cells, which can increase the incidence angle of the light entering the Fresnel lens (Figure 1b), are used in our proposed Π-shaped optical system. However, the light deviates from the surface of the solar cell at a certain value (Fig. 1c). To solve this problem, mirrors can be placed around the distance between the Fresnel lens and the photocells, as shown in Fig. 1d.

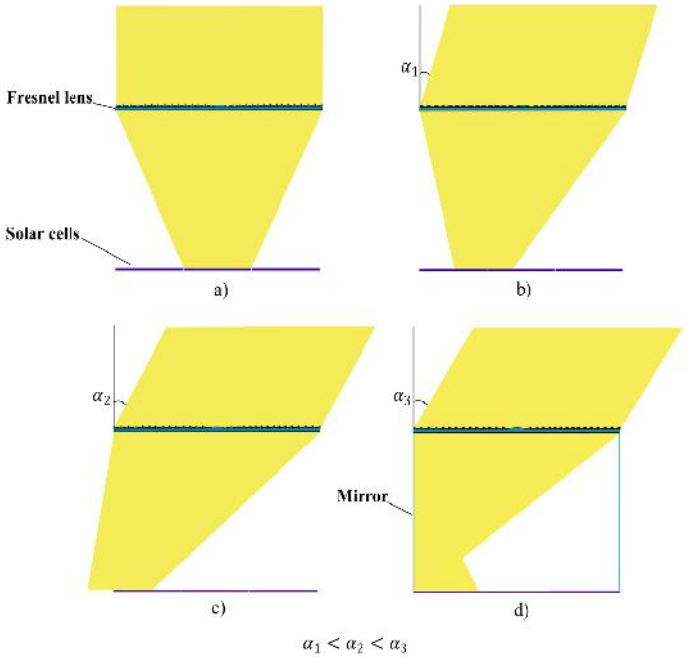

Fig. 1. Π-shaped concentrating optics at different incidence angles.

As shown in Fig. 2, the Π-shaped concentrating optics consists of a Fresnel lens, four reflective mirrors, which make the concentrating system as a letter Π, and nine polycrystalline silicon solar cells. The length of each solar cell is 50 mm, length of Fresnel lens is 150 mm, height of the mirror is 150 mm.

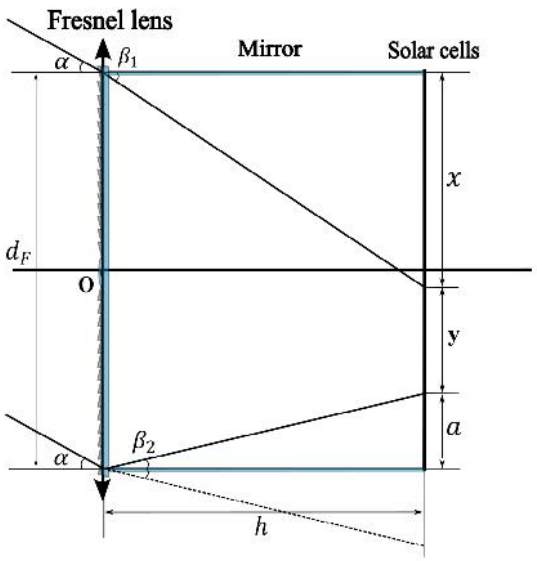

Fig. 2. The geometrical diagram of Π-shaped concentrating optics.

Figure 2 shows the path of the ray at a certain angle on Π-shaped optical system based on a Fresnel lens. Considering the cross-section of the Fresnel lens and assuming that it is a system consisting of prisms, and dividing it into two halves symmetrically, the ray paths corresponding to both right and left sides of the lens are calculated using Eqs. (1)–(4). The light passing through the Fresnel lens refracts at a certain angle and falls on the surface of the solar cell. Accordingly, the position of the incident beam is determined by the following equations:

$$tan\,\beta_1 = \frac{x}{h}; \quad (1)$$

$$x = h \cdot tan\,\beta_1, \quad (2)$$

where β_1 is refracting angle, x is the position of the right incident beam.

The ray path for the second part of the Fresnel lens is calculated by Eqs. (3) and (4). The light passing through the lens is refracted at a certain angle and reflects off the mirror and falls on the surface of the solar cell.

$$tan\beta_2 = \frac{a}{h}; \quad (3)$$

$$a = h \cdot tan\beta_2, \quad (4)$$

where β_2 is refracting angle, a is the position of the left incident beam.

We consider the rays calculated by these two equations to be the outermost rays. Assuming that all the remaining rays are located between these two rays, we can calculate the length of the light spot with the following equation:

$$y = d_F - (a + x), \quad (5)$$

where y is the length of the light spot.

The next problem is to determine at what angle the ray passing through the Fresnel lens is refracted. We consider the lens as a system consisting of prisms as shown in Fig. 3. It is necessary to determine the angle of refraction by calculating the ray path through the prism.

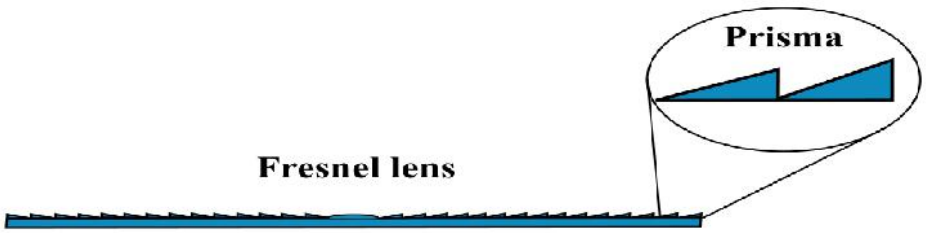

Fig. 3. Fresnel lens structure.

Prisms should be considered in two different cases depending on their location on the two right and left sides from the centre of the Fresnel lens. In the first case, let us consider the prism located on the right side of the Fresnel lens.

First of all, we express the incidence angle of the ray α for the horizontal plane:

$$\alpha = \alpha_1 - \psi\,, \quad (6)$$

where α_1 is the angle between incident ray and perpendicular on prism, ψ is the deflection angle of the prism.

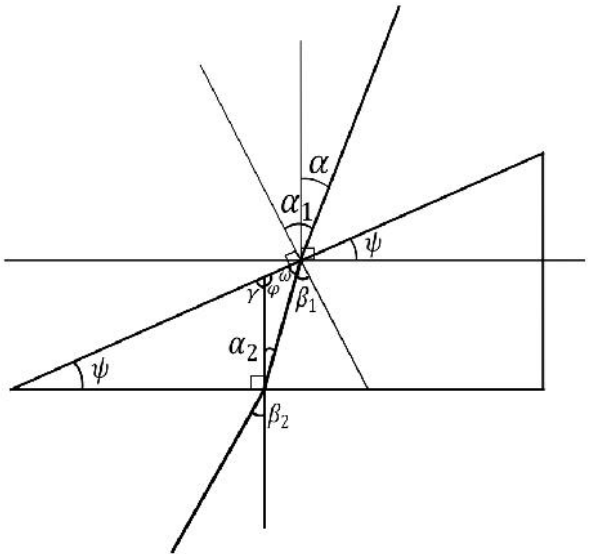

Fig. 4. Path of the rays through right prism of Fresnel lens grooves.

According to Snell's law, the angles α_1 and β_1 can be found as follows:

$$\frac{sin\alpha_1}{sin\beta_1} = \frac{n}{1}; \quad (7)$$

$$n \cdot sin\beta_1 = sin\alpha_1; \quad (8)$$

$$sin\beta_1 = \frac{sin\alpha_1}{n}, \quad (9)$$

where n is a refractive index.

Considering the Eqs. (7)–(9), the angle can be determined as follows:

$$\beta_1 = arcsin\left(\frac{sin\alpha_1}{n}\right). \quad (10)$$

Subsequently, α_2 can be expressed with angles β_1 and ψ:

$$\omega = 90° - \beta_1$$

$$\gamma = 180° - 90° - \psi$$

$$\varphi = 180° - \gamma$$

$$\alpha_2 = 180° - \varphi - \omega$$

$$\alpha_2 = 180° - (90° + \psi) - (90° - \beta_1)$$

$$\alpha_2 = \beta_1 - \psi; \quad (16)$$

$$\frac{sin\alpha_2}{sin\beta_2} = \frac{1}{n}; \quad (17)$$

$$sin\beta_2 = n \cdot sin\alpha_2. \quad (18)$$

The refraction angles of the ray coming out of the prism can be determined using the following equations:

$$sin\beta_2 = n \cdot sin\,(\beta_1 - \psi); \quad (19)$$

$$sin\beta_2 = n \cdot sin\,\left(arcsin\left(\frac{sin\alpha_1}{n}\right) - \psi\right); \quad (20)$$

$$\alpha_1 = \alpha + \psi; \quad (21)$$

$$sin\,\beta_2 = n \cdot sin\,\left(arcsin\frac{sinsin(\alpha+\psi)}{n} - \psi\right); \quad (22)$$

$$\beta_1 = arcsin\left(n \cdot sin\,\left(arcsin\frac{sinsin\,(\alpha+\psi)}{n} - \psi\right)\right). \quad (23)$$

Next, we need to determine the ray path for the prism on the left side of the Fresnel lens. The calculations for the left side of the lens will be as the right side.

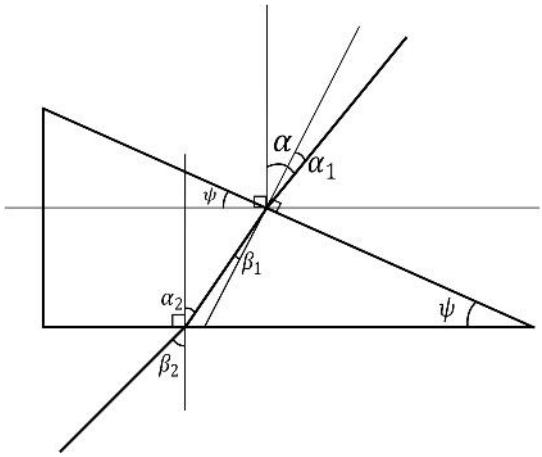

Fig. 5. Path of the rays through left prism of Fresnel lens grooves.

First of all, we express the incidence angle of the ray for the horizontal plane:

$$\alpha = \alpha_1 + \psi. \quad (24)$$

Further, we calculate the path of the incident ray at a certain angle and determine the angle of refraction using the following equations:

$$sin\,\beta_2' = n \cdot sin\left(arcsin\frac{\sin(\alpha-\psi)}{n} + \psi\right); \quad (25)$$

$$\beta_2' = arcsin\left(n \cdot sin\left(arcsin\frac{sin\,(\alpha-\psi)}{n} + \psi\right)\right). \quad (26)$$

According to the calculations of the Π-shaped optical system, the dependence of the width of the light spot on the surface of the solar cells on different incidence angles was established. In order to compare the obtained results, a 3D model of the Π-shaped optical system was created in the COMSOL Multiphysics program, and a Ray Tracing simulation was carried out using the Geometrical Optics section of the program.

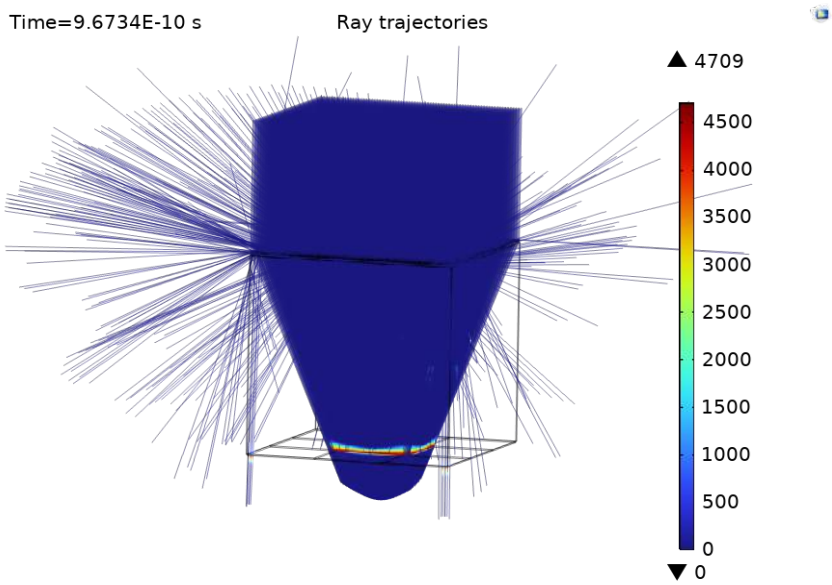

Fig. 6. Ray tracing simulation of the Π-shaped optical system.

As a result of the simulation, we determined the total number of rays that hit each solar cell by setting the ray detector state. If the initial number of rays is known, then we can determine the optical efficiency using the following equation:

$$\eta_{opt} = \frac{n_{entry}}{n_{exit}} \cdot 100\% , \quad (27)$$

where n_{entry} is the number of rays falling on the surface of the solar cell, n_{exit} is the number of primary rays, which equals 5700, in our case.

Optical efficiency is one of the most significant parameters in the design of solar concentrators. During the simulation, the sunlight falls on the П-shaped optical system at an incidence angle of 0–25 degrees. As a result, the dependence of the optical efficiency on different incidence angles was obtained.

3. RESULTS OF THE CALCULATIONS AND MODELLING THE П-SHAPED OPTICAL SYSTEM

We can determine the length of the light spot at different incidence angles using Eq. (5). We can see the dependence of the width of the light spot on the incidence angles from 0 to 20 degrees in Fig. 7. Taking into account that the width of the light spot should not be smaller than the length of the solar cell, i.e., 50 mm, we determined that the deviation of 18 degrees of incidence angle is the limit value. If the incidence angle exceeds 18 degrees, the length of the light spot decreases.

The fact that the width of the light spot is smaller than the length of the solar cell leads to a decrease in optical efficiency, which is one of the important parameters in concentrating optical systems. The high value of the optical efficiency in variations of the incidence angle allows reducing the operation of the solar tracking system.

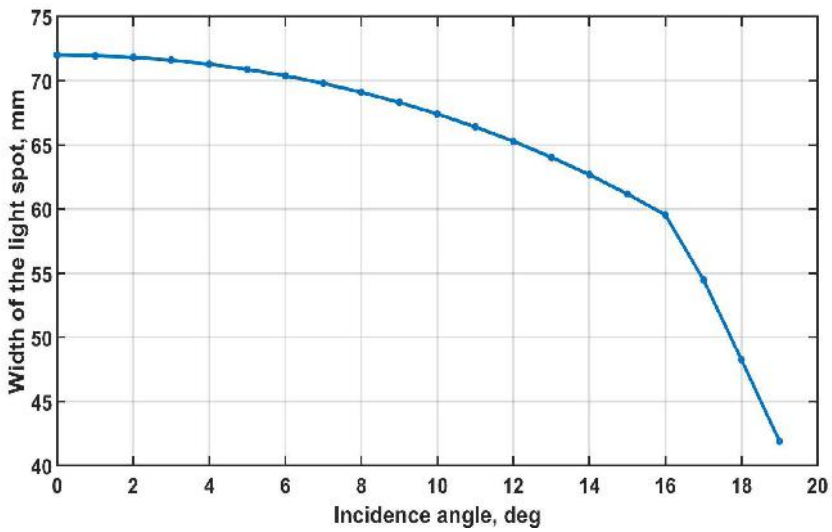

Fig. 7. Width of the light spot at different incidence angles.

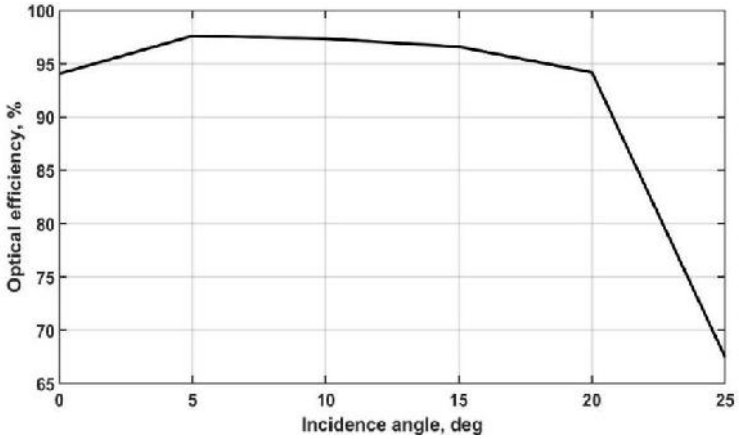

Fig. 8. Optical efficiency at different incidence angles.

Figure 8 shows the dependence of the optical efficiency of the system on different incidence angles using the results obtained on COMSOL Multiphysics. From this dependence shown in Fig. 8, we can see that the value of the optical efficiency decreases when incidence angle exceeds 20 degrees. If we do not make any changes to the geometry of the optical system, it can be stated that the efficiency of the optical system is directly proportional to the width of the light spot. The optical efficiency rises from 94 % to 97 %, when the incidence angle expands from 0 to 5 degrees, and this is the significant benefit of the system. We can see that the dependence constructed as a result of the calculations shown in Fig. 7 is similar to the dependence obtained from the simulation in Fig. 8.

One of the important optical parameters of optical systems is the geometric concentration ratio, which is determined as the ratio of the lens area to the cell area:

$$C_g = \frac{A_{lens}}{A_{cell}}, \tag{28}$$

where A_{lens} is the area of the Fresnel lens, A_{cell} is the area of the solar cell.

Depending on the equations used in the description of the Π-shaped optical system, the geometric concentration ratio can be determined as follows:

$$C_g = \left(\frac{d_F}{y}\right)^2. \tag{29}$$

Using Eq. (29), the geometric concentration ratio of the Π-shaped optical system is calculated, and the dependence of the geometrical concentration ratio on the incidence angle is plotted in Fig. 9.

If we consider that the d_F is the constant value, y is the width of the light spot, the geometrical concentration ratio only depends on the width of the light spot. Narrowing the width of the light spot leads to increasing the geometrical concentration ratio. It can be seen in Fig. 9 that the geometrical concentration ratio increases by increasing the incidence angle. By multiplying the geometrical concentration ratio by optical efficiency of the system, we get a concentration ratio of the optical system [47]:

$$C = C_g \cdot \eta_{op}, \tag{30}$$

where η_{op} – optical efficiency. As a result of the calculation, we get the dependence of concentration ratio on the incidence angle shown in Fig. 10.

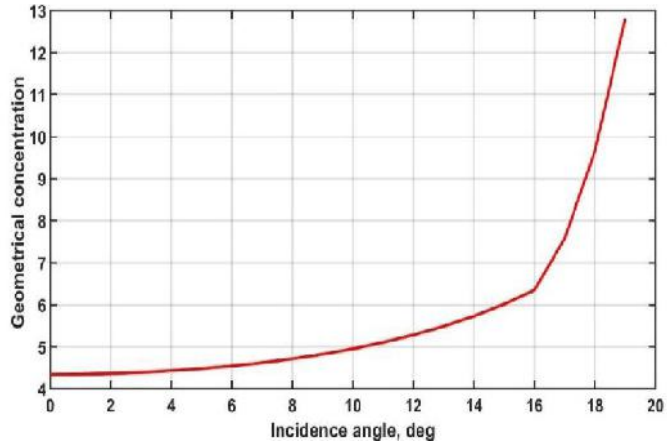

Fig. 9. Geometrical concentration ratio at different incidence angles.

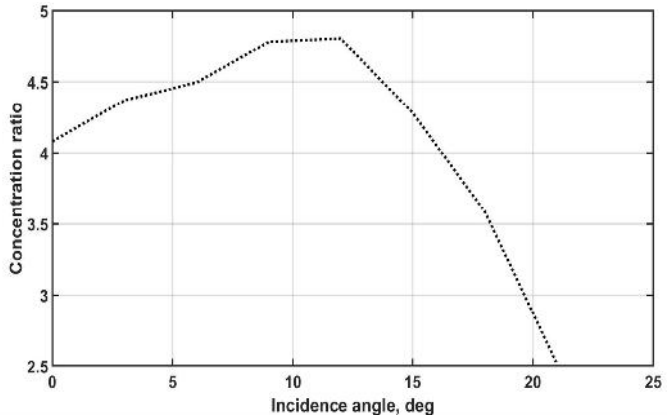

Fig. 10. Concentration ratio at different incidence angles.

As it can be seen in Fig. 10, the concentration ratio decreases by increasing the incidence angle. However, it remains in the range approximately 3x–5x from 0 to 20 degrees of the incidence angle; it shows that the system can exhibit good performance at 20 degrees of the incidence angle, and it benefits to reduce the work of a solar tracking system. In terms of the increase of optical efficiency using reflective mirrors which help redirect the sunlight to the surface of the solar cells, when the incidence angle increases from 0 to 12 degrees, the concentration ratio also increases. Taking into account that the incidence angle deviates from the central normal of the optical surface on both sides, if we double the value of the incidence angle, the optical system maintains high optical efficiency when the sun rotates by 40 degrees.

4. DISCUSSION OF THE RESULTS

During the work, a *П*-shaped optical system based on a Fresnel lens was proposed for low concentrating photovoltaic systems. In order to determine the optical efficiency of the proposed system, geometrical and mathematical calculations were carried out,

during the calculation, the width of the concentrated light spot in the *П*-shaped optical system was mathematically expressed, and the length of the light spot was determined. In addition, the change in the width of the light spot at different angles of incidence of light was observed. Based on the calculations, a 3D model of the *П*-shaped optical system was created in the COMSOL Multiphysics software, and its optical efficiency was determined using Ray tracing simulation. Based on the work done, the following results were achieved:

1. The light spot maintained its effective width up to 18 degrees at the incidence angle between 0–20 degrees;
2. When the incidence angle of the optical system was in the range of 0–25 degrees, the optical efficiency did not fall below 95 % up to 20 degrees;
3. The width of concentrated sunlight and optical efficiency were directly proportional quantities;
4. The geometric concentration ratio of the *П*-shaped optical system in the range of 0–20 degrees was calculated using the width of the light spot. As a result, it was determined that the geometrical concentration ratio was about 4–9 at the incidence angle up to 18 degrees;
5. Using the optical efficiency and geometric concentration ratio, the concentration ratio in the range of 0–25 degrees of incidence angle was calculated; as a result, it was determined that the concentration ratio was in the range of 2.5–5 up to 20 degrees, which corresponded to the low concentrating photovoltaic;
6. Using the proposed *П*-shaped optical system, the solar tracker of the LCPV could stand still up to 40 degrees.

Most of the Fresnel lens-based concentrating optical elements or systems have low acceptance angles, and they require high-precision solar tracking systems. Particularly, high concentrating solar cells with Fresnel lens usually have a low acceptance angle. The work [29] designed a Fresnel lens, and its acceptance angle was between 0.6 to 0.8°, and the optical efficiency was between 80 and 90 %. The studies [40], [41], [30] showed that Fresnel lenses with a secondary optics could increase the acceptance angle and uniform distribution of sunlight, but those systems still had comparably low acceptance because those systems provided high concentrated solar radiation, which required small high-efficiency multi-junction solar cells. Due to the small size of the solar cells, concentrating the sunlight into one point becomes more difficult if the rays are not perpendicular to the surface of the lens. In this work, we used inexpensive polycrystalline silicon solar cells as in our one of the previous works [33], it was proven that a polycrystalline silicon solar cell with Fresnel lens at optimal cell-lens distance could generate 27 % more energy than a non-concentrating solar cell. The proposed *П*-shaped optical system allows the LCPV to work without sun tracking up to 20 degrees. In addition, we can even see the increase in the optical efficiency and concentration ratio at lower incidence angles.

In the case of using the proposed optical system, it is possible to provide a low concentration level on the surface of the solar cell. Based on the obtained results, the capability of the proposed ***П***-shaped optical system, which can minimise the operation of the solar tracking system for low-concentration photovoltaic systems, was demonstrated using mathematical calculations and computer simulations.

5. CONCLUSION

Detailed investigation of geometrical optics of the proposed Π-shaped concentrating optics was performed. Expressions describing the incidence ray path through the concentrating optics were presented, and width of the light spot at different incidence angles was calculated. Optical efficiency at different incidence angles was found by the results of COMSOL Multiphysics and geometrical concentration ratio, the concentration ratio was calculated. It was found that the system had high optical efficiency of approximately 95 %, and its concentration ratio of 3x–5x at the range of ± 0-20 degrees of incidence angle and it could reduce the work of a solar tracking system. Additionally, an increase in the optical efficiency can be seen from 0 to 5 degrees of the incidence angle and an increase in the concentration ratio can be seen from 0 to 12 degrees of the incidence angle in terms of the reflective mirrors, which help redirect the rays to the solar cells. Optical systems with such a high incidence angle can reduce the performance of the solar tracker system, and it reduces the overall cost and energy consumption of the LCPV. It greatly simplifies the process of system implementation and maintenance.

ACKNOWLEDGEMENTS

This research has been funded by the Science Committee of the Ministry of Science and Higher Education of the Republic of Kazakhstan (Grant No. AP19574454).

REFERENCES

1. Lewis, N. S., & Nocera, D. G. (2006). Powering the Planet: Chemical Challenges in Solar Energy Utilization. *Proceedings of the National Academy of Sciences*, *103* (43), 15729–15735. https://doi.org/10.1073/pnas.0603395103
2. Kannan, N., & Vakeesan, D. (2016). Solar Energy for Future World: A Review. *Renewable and Sustainable Energy Reviews*, *62*, 1092–1105. https://doi.org/10.1016/j.rser.2016.05.022
3. Jatoi, A. R., Samo, S. R., & Jakhrani, A. Q. (2021). Performance Evaluation of Various Photovoltaic Module Technologies at Nawabshah Pakistan. *International Journal of Renewable Energy Development*, *10* (1), 97. https://doi.org/10.14710/ijred.2021.32352
4. Yamaguchi, M. (2003). III–V Compound Multi-Junction Solar Cells: Present and Future. *Solar energy materials and solar cells*, *75* (1–2), 261–269. https://doi.org/10.1016/S0927-0248(02)00168-X
5. Klugmann-Radziemska, E. (2023). Environmental Assessment of Solar Cell Materials. *Ecological Chemistry and Engineering S*, *30* (1), 23–35. https://doi.org/10.2478/eces-2023-0002
6. Kafui, A. D., Seres, I., & Farkas, I. (2019). Efficiency Comparison of Different Photovoltaic Modules. *Acta Technologica Agriculturae*, *22* (1), 5–11. https://doi.org/10.2478/ata-2019-0002
7. Michael, J. J., Iqbal, S. M., Iniyan, S., & Goic, R. (2018). Enhanced Electrical Performance in a Solar Photovoltaic Module Using V-Trough Concentrators. *Energy*, *148*, 605–613. https://doi.org/10.1016/j.energy.2018.01.101

8. Al-Ghezi, M. K., Ahmed, R. T., & Chaichan, M. T. (2022). The Influence of Temperature and Irradiance on Performance of the Photovoltaic Panel in the Middle of Iraq. *International Journal of Renewable Energy Development*, *11* (2), 501. https://doi.org/10.14710/ijred.2022.43713
9. Finot, M., & MacDonald, B. (2011). Significant Cost Reduction through New Optical, Thermal, and Structural Design for a Medium-CPV System. *High and Low Concentrator Systems for Solar Electric Applications VI,* 8108, 86–95. SPIE. https://doi.org/10.1117/12.894187
10. Bilal, M., Arbab, M. N., Afridi, M. Z. U. A., & Khattak, A. (2016). Increasing the Output Power and Efficiency of Solar Panel by Using Concentrator Photovoltaics (CPV). *International Journal of Engineering Works*, *3* (12), 98–102.
11. Zainulabdeen, F. S., Al-Hamdani, A. H., Karam, G. S., & Ali, J. H. (2019). Improving the Performance Efficiency of Solar Panel by Using Flat Mirror Concentrator. *AIP Conference Proceedings*, *2190* (1). AIP Publishing. https://doi.org/10.1063/1.5138540
12. Parupudi, R. V., Singh, H., & Kolokotroni, M. (2020). Low Concentrating Photovoltaics (LCPV) for Buildings and their Performance Analyses. *Applied Energy*, *279*, 115839. https://doi.org/10.1016/j.apenergy.2020.115839
13. Hasan, A., Sarwar, J., & Shah, A. H. (2018). Concentrated Photovoltaic: A Review of Thermal Aspects, Challenges and Opportunities. *Renewable and Sustainable Energy Reviews*, *94*, 835–852. https://doi.org/10.1016/j.rser.2018.06.014
14. Maka, A. O., & O'Donovan, T. S. (2020). A Review of Thermal Load and Performance Characterisation of a High Concentrating Photovoltaic (HCPV) Solar Receiver Assembly. *Solar Energy*, *206*, 35–51. https://doi.org/10.1016/j.solener.2020.05.022
15. Valera, Á., Rodrigo, P. M., Almonacid, F., & Fernández, E. F. (2021). Efficiency Improvement of Passively Cooled Micro-Scale Hybrid CPV-TEG Systems at Ultra-High Concentration Levels. *Energy Conversion and Management*, *244*, 114521. https://doi.org/10.1016/j.enconman.2021.114521
16. Baig, H., Heasman, K. C., Sarmah, N., & Mallick, T. (2012). Solar Cells Design for Low and Medium Concentrating Photovoltaic Systems. *AIP Conference Proceedings, 1477* (1), 98–101. American Institute of Physics. https://doi.org/10.1063/1.4753843
17. Payet, J., & Greffe, T. (2019). Life Cycle Assessment of New High Concentration Photovoltaic (HCPV) Modules and Multi-Junction Cells. *Energies*, *12* (15), 2916. https://doi.org/10.3390/en12152916
18. Grasso, G., Righetti, A., Ubaldi, M. C., Morichetti, F., & Pietralunga, S. M. (2012). Competitiveness of Stationary Planar Low Concentration Photovoltaic Modules Using Silicon Cells: A Focus on Concentrating Optics. *Solar Energy*, *86* (6), 1725–1732. https://doi.org/10.1016/j.solener.2012.03.015
19. Philipps, S. P., Bett, A. W., Horowitz, K., & Kurtz, S. (2015). *Current Status of Concentrator Photovoltaic (CPV) Technology* (No. NREL/TP-5J00-65130). National Renewable Energy Lab. (NREL), Golden, CO (United States).
20. Hamza, M., Kechiche, O. B. H. B., Barkaoui, B., & Sammouda, H. (2017, March). Performance comparison between commercial mono-crystalline and poly-crystalline PV modules under LCPV conditions. In *2017 International Conference on Green Energy Conversion Systems (GECS)* (pp. 1–6). IEEE. https://doi.org/10.1109/GECS.2017.8066261
21. Shanks, K., Senthilarasu, S., & Mallick, T. K. (2016). Optics for Concentrating Photovoltaics: Trends, Limits and Opportunities for Materials and Design. *Renewable and Sustainable Energy Reviews*, *60*, 394–407. https://doi.org/10.1016/j.rser.2016.01.089
22. Amanlou, Y., Hashjin, T. T., Ghobadian, B., Najafi, G., & Mamat, R. (2016). A Comprehensive Review of Uniform Solar Illumination at Low Concentration Photovoltaic (LCPV) Systems. *Renewable and Sustainable Energy Reviews*, *60*,

1430–1441. https://doi.org/10.1016/j.rser.2016.03.032

23. Baig, H., Montecucco, A., Siviter, J., Li, W., Paul, M., Sweet, T., ... & Mallick, T. (2016). Indoor Characterization of a Reflective Type 3D LCPV System. *AIP Conference Proceedings*, *1766* (1). AIP Publishing. https://doi.org/10.1063/1.4962070
24. Schuetz, M. A., Shell, K. A., Brown, S. A., Reinbolt, G. S., French, R. H., & Davis, R. J. (2012). Design and Construction of a∼ 7× Low-Concentration Photovoltaic System Based on Compound Parabolic Concentrators. *IEEE Journal of Photovoltaics*, *2* (3), 382–386. https://doi.org/10.1109/JPHOTOV.2012.2186283
25. Mallick, T. K., & Eames, P. C. (2008). Electrical Performance Evaluation of Low-Concentrating Non-imaging Photovoltaic Concentrator. *Progress in Photovoltaics: Research and Applications*, *16* (5), 389–398. https://doi.org/10.1002/pip.819
26. Sonneveld, P. J., Swinkels, G. L. A. M., Van Tuijl, B. A. J., Janssen, H. J. J., Campen, J., & Bot, G. P. A. (2011). Performance of a Concentrated Photovoltaic Energy System with Static Linear Fresnel Lenses. *Solar Energy*, *85* (3), 432–442. https://doi.org/10.1016/j.solener.2010.12.001
27. Cvetkovic, A., Mohedano, R., Gonzalez, O., Zamora, P., Benitez, P., Fernandez, P. M., ... & Miñano, J. C. (2011). Performance Modeling of Fresnel-based CPV Systems: Effects of Deformations under Real Operation Conditions. *AIP Conference Proceedings*, *1407* (1), 74–78. American Institute of Physics. https://doi.org/10.1063/1.3658298
28. Xie, W. T., Dai, Y. J., Wang, R. Z., & Sumathy, K. (2011). Concentrated Solar Energy Applications Using Fresnel Lenses: A Review. *Renewable and Sustainable Energy Reviews*, *15* (6), 2588–2606. https://doi.org/10.1016/j.rser.2011.03.031
29. El Himer, S., Al Ayane, S., & Ahaitouf, A. (2020, September). Optical Modeling and Performance Design of a Fresnel Lens for CPV Units. *IOP Conference Series: Materials Science and Engineering*, *937* (1), 012025. IOP Publishing. https://doi.org/10.1088/1757-899X/937/1/012025
30. Renzi, M., Cioccolanti, L., Barazza, G., Egidi, L., & Comodi, G. (2017). Design and Experimental Test of Refractive Secondary Optics on the Electrical Performance of a 3-Junction Cell Used in CPV Systems. *Applied Energy*, *185*, 233–243. https://doi.org/10.1016/j.apenergy.2016.10.064
31. El Himer, S., El-Yahyaoui, S., Mechaqrane, A., & Ahaitouf, A. (2017). Comparative Study of Two CPV Optical Concentrators, Using a Fresnel Lens as Primary Optical Element. *IOP Conference Series: Materials Science and Engineering*, *186* (1), 012033. IOP Publishing. https://doi.org/10.1088/1757-899X/186/1/012033
32. Ferrer-Rodríguez, J. P., Baig, H., Fernández, E. F., Almonacid, F., Mallick, T., & Pérez-Higueras, P. (2017). Optical Modeling of Four Fresnel-based High-CPV Units. *Solar Energy*, *155*, 805–815. https://doi.org/10.1016/j.solener.2017.07.027
33. Dosymbetova, G., Mekhilef, S., Saymbetov, A., Nurgaliyev, M., Kapparova, A., Manakov, S., ... & Koshkarbay, N. (2022). Modeling and Simulation of Silicon Solar Cells under Low Concentration Conditions. *Energies*, *15* (24), 9404. https://doi.org/10.3390/en15249404
34. Wiesenfarth, M., Steiner, M., Wolf, J., Schmidt, T., & Bett, A. W. (2014). Investigation of Different Fresnel Lens Designs and Methods to Determine the Optical Efficiency. *AIP Conference Proceedings*, *1616* (1), 97–101. American Institute of Physics. https://doi.org/10.1063/1.4897037
35. Jing, L., Liu, H., Wang, Y., Xu, W., Zhang, H., & Lu, Z. (2014). Design and Optimization of Fresnel Lens for High Concentration Photovoltaic System. *International Journal of Photoenergy*. https://doi.org/10.1155/2014/539891
36. Yeh, N. (2010). Analysis of Spectrum Distribution and Optical Losses under Fresnel Lenses. *Renewable and Sustainable Energy Reviews*, *14* (9), 2926–2935. https://doi.org/10.1016/j.rser.2010.07.016

37. Drury, E., Lopez, A., Denholm, P., & Margolis, R. (2014). Relative Performance of Tracking versus Fixed Tilt Photovoltaic Systems in the USA. *Progress in Photovoltaics: Research and Applications*, *22* (12), 1302–1315. https://doi.org/10.1002/pip.2373

38. Kumar, V., Shrivastava, R. L., & Untawale, S. P. (2015). Fresnel lens: A promising Alternative of Reflectors in Concentrated Solar Power. *Renewable and Sustainable Energy Reviews*, *44*, 376–390. https://doi.org/10.1016/j.rser.2014.12.006

39. Gol, A. E., & Ščasný, M. (2023). Techno-Economic Analysis of Fixed versus Sun-Tracking Solar Panels. *International Journal of Renewable Energy Development*, *12* (3), 615. https://doi.org/10.14710/ijred.2023.50165

40. Akisawa, A., Hiramatsu, M., & Ozaki, K. (2012). Design of Dome-Shaped Non-imaging Fresnel Lenses Taking Chromatic Aberration into Account. *Solar Energy*, *86* (3), 877–885. https://doi.org/10.1016/j.solener.2011.12.017

41. Goldstein, A., & Gordon, J. M. (2011). Tailored Solar Optics for Maximal Optical Tolerance and Concentration. *Solar Energy Materials and Solar Cells*, *95* (2), 624–629. https://doi.org/10.1016/j.solmat.2010.09.029

42. El Himer, S., Ahaitouf, A., El-Yahyaoui, S., Mechaqrane, A., & Ouagazzaden, A. (2012). A Comparative of Four Secondary Optical Elements for CPV Systems. *AIP Conference Proceedings*, *30003*. https://doi.org/10.1063/1.5053502

43. Pham, T. T., Vu, N. H., & Shin, S. (2019). Novel Design of Primary Optical Elements Based on a Linear Fresnel Lens for Concentrator Photovoltaic Technology. *Energies*, *12* (7), 1209. https://doi.org/10.3390/en12071209

44. Bione, J., Vilela, O. C., & Fraidenraich, N. (2004). Comparison of the Performance of PV Water Pumping Systems Driven by fixed, Tracking and V-Trough Generators. *Solar Energy*, *76* (6), 703–711. https://doi.org/10.1016/j.solener.2004.01.003

45. Sumathi, V., Jayapragash, R., Bakshi, A., & Akella, P. K. (2017). Solar Tracking Methods to Maximize PV System Output–A Review of the Methods Adopted in Recent Decade. *Renewable and Sustainable Energy Reviews*, *74*, 130–138. https://doi.org/10.1016/j.rser.2017.02.013

46. Larico, E. R. A., & Gutierrez, A. C. (2022). Solar Tracking System with Photovoltaic Cells: Experimental Analysis at High Altitudes. *International Journal of Renewable Energy Development*, *11* (3), 630. https://doi.org/10.14710/ijred.2022.43572

47. Renno, C., & Perone, A. (2021). Experimental Modeling of the Optical and Energy Performances of a Point-Focus CPV System Applied to a Residential User. *Energy, 15*, 119156. https://doi.org/10.1016/j.energy.2020.119156